# Experimental Evaluation of Loads from Inundation-Driven Debris Fields

Dakota Mascarenas

A thesis
submitted in partial fulfillment of the
requirements for the degree of

Master of Science

University of Washington

2022

Committee:
Michael R. Motley
Marc O. Eberhard
Pedro Arduino

Program Authorized to Offer Degree:
Civil & Environmental Engineering

University of Washington

## Abstract

Experimental Evaluation of Loads from Inundation-Driven Debris Fields

Dakota Mascarenas

Co-Chairs of the Supervisory Committee:
Michael R. Motley
Civil & Environmental Engineering

Marc O. Eberhard
Civil & Environmental Engineering

Inundation events, such as tsunamis and storm surges, pose a significant threat to coastal communities and infrastructure globally. Damage caused to communities is not only caused by flowing water, but also by debris from collapsed structures, vegetation, and whatever might be moved by an inundation flow. Previous studies have investigated wave- and flow-induced loading, but have not investigated the influence of debris fields (i.e., multiple pieces of debris) carried by inundation-type flows. The impacts from dense debris fields are chaotic in nature and it can be difficult to predict how the disparate debris will interact with a coastal structure. While single-debris impacts are fairly predictable and reproducible, debris fields require a statistically-driven approach.

This study presents the results of an experimental program in the Large Wave Flume at the NHERI Wave Research Lab conducted to generate a statistically-representative data set of various multi-debris scenarios and provide measurements to inform numerical modeling efforts. This thesis analyzes streamwise forcing via in-line load cells attached to a test structure to quantify reaction forces induced by high-density polyethylene (HDPE) debris fields, while varying: (i) number of debris, (ii) debris orientation, (iii) debris field density, and (iv) individual debris size. All tests within this scope were subjected to a single, repeatable

wave that remained unbroken throughout the test environment.

In general, peak forcing increases at a decreasing rate with the number of debris, such that the highest impact forces observed (with 24 debris) are approximately 3.25 times the magnitude of the maximum impact of a single debris oriented with its long axis in the direction of flow. Additionally, increasing debris field density tends to yield higher measured forces. A clear distinction between a first peak loading event and a second peak loading event is revealed in forcing time histories. Via analysis of video data, hypothesized explanations for the first and second peak are proposed: the first peak represents the initial contact of the debris field with the structure, while the second peak occurs up to 2 seconds later as randomized impacts after the initial debris field has broken apart. Correlation is also found between first peak impact and: 1) orientation of individual debris, such that debris oriented in the direction of flow has higher first peak values than transverse counterparts; and 2) cohesion of the mass within the debris field at the time of impact. Most tests, however, see absolute maxima during the second peak period, indicating that chaotic impacts after the initial impact represent significant loading. Further, low frequency forcing after impacts (i.e., "damming") is also present. This is hypothesized to be due to debris becoming caught on the test structure and has high variability between tests. Configurations with smaller individual debris pieces tend to have lower damming forces, despite the mass and density of the debris field being held constant. Damming reaction forces can be as high as 20% of peak loading values: the sustained forcing may have significant structural implications. Ultimately, this thesis will add to a large-scale study working to inform how a flow-driven debris field may interact with the coastal built environment during large-scale inundation events, and seeks to add research to assist coastal community resilience in the face of natural hazards.

# TABLE OF CONTENTS

# LIST OF FIGURES

# LIST OF TABLES

# ACKNOWLEDGMENTS

I acknowledge all past, present, and future Coast Salish peoples of this land (now known as Seattle, Washington), including the Duwamish, Puyallup, Suquamish, Tulalip, and Muckleshoot nations, on whose traditional lands I study and work. I acknowledge my work was also performed within the traditional lands (now called Corvallis, Oregon) of the Mary's River or Ampinefu Band of Kalapuya. After the Willamette Valley Treaty of 1855, Kalapuya people were forcibly removed from their homelands to reservations in Western Oregon. Kalapuya descendants are now a part of the Confederated Tribes of Grand Ronde Community of Oregon and the Confederated Tribes of the Siletz Indians. I acknowledge that Indigenous peoples are caretakers of the land and waters, crucial to our collective sustainable future - and have been since time immemorial. Note: these acknowledgements are warmly adapted from land acknowledgement resources at the UW (2022) and OSU (2021).

I acknowledge and appreciate generous fellowships and funding from GSEE at the University of Washington, University of Washington College of Engineering, and NSF Grant #203791.

Thank you to the team at Oregon State University's O.H. Hinsdale Wave Lab for going out of their way to make my work easy, meaningful, and exciting. Thank you too to Abbey, who's going to do awesome things in her career.

Thank you again and again to my advisors and mentors – especially Mike, Marc, Jim, Alex, Sarah, and Nirni – for all the time, effort, and belief in me.

Finally, a huge thank you to all of my family (especially Mom and Dad), my partner, and my extended family of friends. Wouldn't be here without you.

# DEDICATION

to Mackenzie, who rides all the waves

# Chapter 1

# INTRODUCTION & MOTIVATION

## *1.1 Motivation*

Large-scale water inundations caused by tsunamis and storm surges represent a significant threat to coastal infrastructure and environments, both locally and globally. In the Pacific Northwest of the United States and Canada, west coasts of Washington, Oregon, Northern California, and British Columbia are in close proximity to the Cascadia Megathrust Fault. The Cascadia Megathrust Fault is a zone of subduction that could cause a deep, powerful earthquake (i.e., Heaton and Hartzell (1987)). Subduction zone earthquakes are devastating in their own right, but may also cause upheaval and change in the bathymetry of the ocean floor. Other tsunamigenic events include landslides, volcanic eruptions, and meteorological forcing (see Winter (2019)).

For subduction-zone tsunamigenesis, a sudden change of bathymetry in the ocean floor near the subduction zone due to a megathrust earthquake has the potential to uplift the entire water column, producing a tsunami wave. The Cascadia Fault runs from northern Vancouver Island, British Columbia to northern California. The most recent tsunami event caused by the Cascadia Fault is understood to be in 1700 following a massive earthquake (e.g., Yamaguchi et al. (1997)). While estimates vary somewhat, a recurrence interval of approximately 530 years is found in Petersen et al. (2014). It should be noted that additional tsunami hazards from far-field subduction zone events pose risk, albeit to a lesser degree, as energy dissipation occurs throughout the ocean basin.

A magnitude 9.0 earthquake and subsequent tsunami event due to the Cascadia Megathrust Fault would be catastrophic, inundating highly populated coastline along the entire west coast of the US and Canada, as well as Hawaii and across the Pacific to Japan and Southeast

Asia. A recent, globally impactful example of the destructive power of tsunamis came in 2011 during the Tohoku earthquake and tsunami event. Following a massive megathrust earthquake (M9.0), a tsunami inundated large swaths of coasts and rivers in northern Japan. The inundation overtopped seawalls, destroyed buildings and infrastructure, and carried marine and urban kilometers inland. Figure 1.1 shows the tsunami overtopping a seawall in Miyako City, Iwate Prefecture, Japan.


Figure 1.1: March 11, 2011 tsunami overtops seawall in Miyako City, Japan (Reuters (2015)).

Tsunamis generated via a megathrust subduction zone earthquake propagate quickly and carry immense energy through the ocean: wavelengths can be 100 to 500 km, which greatly exceeds normal sea states and swell waves. Since wave speed is governed via the dispersion relation, the length of tsunami wavelengths gives a very high wave celerity, $c$. Tsunamis follow the shallow-water approximation given linear wave theory even across ocean basins due to their long wavelengths, which defines shallow water as $h/\lambda < 0.05$. Given the average depth of the Pacific Ocean is about 4 km and tsunami wavelengths are 100 to 500km, tsunami waves fall within the shallow-wave parameters. The dispersion relationship can be simplified to give a wave celerity (i.e., velocity) of $c = \sqrt{gh}$, where $g$ is gravitational acceleration

(approximately $9.81 m/s^2$) and $h$ is the water depth. Tsunami waves slow and increase in wave height given decreasing $h$ in a process called shoaling. While a tsunami wave height may only be 1m in deep water, the wave height increases substantially with decreasing wavelength and wave celerity. A combination of near-shore dynamics may cause wave heights in excess of 30m moving far inland as bore-like walls of water. A more complete discussion of tsunami fluid mechanics can be found in Dean and Dalrymple (1991).

While tsunamis pose a significant threat to the west coast of the United States, storm surges, especially on the American East Coast and Southeast due to hurricanes, also warrant concern and discussion. Storm surges can inundate low-lying areas and carry debris, causing damage via similar mechanisms as a tsunami. For both storm surges and tsunamis, increasing sea level rise due to climate change increases the risk of damage from these hazards. Additionally, the effect of cascading hazards (i.e., a large earthquake followed by a tsunami) is an increase in damage and loss of life.

The risk of damage is further increased in urban areas and/or port areas. Given a powerful flow, any objects which can be mobilized by the flow (i.e., debris) are additional hazards, as they may have substantial impact force given a flow-driven collision. As discussed in ASCE (2016) and Chock (2013), certain debris may also become caught in and around otherwise open areas of structures, increasing sustained loading on a structure via damming.

Natural hazards such as tsunamis and other inundations pose many threats that require increased resilience via more informed engineering. This study seeks to add to the body of work that discusses the complex phenomenon of debris within a flow in an experimental setting.

### *1.1.1 Current ASCE Provisions*

ASCE 7 presents a comprehensive set of structural design criteria for tsunami hazards that includes the effect of flow-driven debris (ASCE (2016)). Different types of debris are considered with potential for introduction into the flow (including shipping containers, vehicles, and wood poles). Debris impact forces on structural systems are a function of flow velocity

and debris mass and stiffness. Additionally, consideration is given to orientation and impulse duration for impacts. Specifically, ASCE 7 discusses the use of the elastic impact equation given material stiffness, mass, and velocity up to the crushing strength of a material.

Debris damming and buildup around a structure is discussed by way of defining a minimum closure area that accounts for additional surface area resisting flow loads due to the accumulation of debris around otherwise open pathways within a structure. In general, this amount is taken to be 50% of otherwise open area. Post-event debris accumulation is not presently accounted for within design consideration, but is certainly a matter to be considered in urban resilience during a recovery phase.

ASCE 7 incorporates the best available science for debris within inundations, but also allows for further research to better understand the complex phenomena of debris within flows. This study seeks to add to the available information for resilient coastal design.

### *1.2 Summary of Existing Literature*

In recent studies of inundation-type hazards (i.e., tsunamis, hurricane storm surges), debris was often found to be a significant player in the failure of impacted structures. McCullough et al. (2013) document several case studies during storm surge events in which debris may be considered to be a significant factor in structural damage, in addition to the storm surge itself. Chock (2013) documented the performance of structures after the 2011 Tohoku tsunami event to further develop the ASCE 7 Standard and considered debris damming and blockage to be significant. Leonard et al. (2011) also discusses the necessity of design for debris in New Zealand's tsunami-resilient structures and commented that collapsed reinforced concrete structures likely absorbed debris impacts during the 2004 Indonesian tsunami. Further discussion of debris damage during this event is discussed in Ghobarah et al. (2006). Similarly, investigations after the 2010 Chilean and 2011 Tokohu tsunamis found structural damage due to debris to be prevalent (e.g., Palermo et al. (2013), Akiyama et al. (2013), Suppasri et al. (2013), Yeh et al. (2014)). More recently, similar trends from cascading earthquake and tsunami hazards and flow-driven debris impact were seen during the 2018

Saluwesi event (Paulik et al. (2019)). Field surveys from these events largely conclude that debris fields and the damage they cause is a significant portion of structural ramifications incurred during high-energy inundation events.

Given the importance of debris in structural damage, several studies have considered single-debris impacts and have lain the basis for more complex debris field interactions. Aghl et al. (2017) investigates in-air debris impact forces of a one-dimensional single debris both numerically and experimentally. Haehnel and Daly (2004) investigated collision geometry for flood-driven wooden debris, reproducing laboratory data using a single degree-of-freedom, linear model. Kobayashi et al. (2012) investigated in-air impact forces due to flexible, one-dimensional debris. Shafiei et al. (2016) correlated impact acceleration forces with known velocity given by the "pick-up" distance from the structure. Stolle et al. (2019) implemented a two degree-of-freedom model for single debris impacts. Paczkowski et al. (2012) extended idealized models into three-dimensional finite element models of single debris. Extending to more complex geometry, several studies have been conducted using small-scale shipping containers propelled by tsunami-like waves, given their prevalence in coastal areas subject to inundation hazards (e.g., Ko et al. (2015), Naito et al. (2016)). Hasanpour et al. (2021) applied the aforementioned experimental conditions to the validation of smoothed particle hydrodynamics (SPH) and finite element models (FEM). Nonlinear conditions due to hydrodynamics at the structure during impact of small-scale shipping containers are investigated by Derschum et al. (2018). Madurapperuma and Wijeyewickrema (2012) also considered shipping container impacts, with a focus on reinforced concrete buildings' failure modes.

Many studies investigate idealized, single debris systems; in real-world hazard scenarios, many debris interact with complexity with the flow, the structure, and other debris. In general, research with debris fields tends toward accumulation and transport instead of impact (as opposed to works discussed for single-debris impacts, and as relevant to structural damage due to flow-driven debris). Schmocker and Hager (2011) discussed accumulations and blockages at bridges which had significant variability. Gschnitzer et al. (2017) conducted scale model tests of bridge clogging by wood and found apparent randomness in clogging

conditions. Naito et al. (2014) proposed procedures for evaluating the potential of sites for debris field impact and structural damage. On a larger scale, Lebreton and Borrero (2013) modeled the transport of debris fields carried by the 2011 Tohoku tsunami in the Northern Pacific Ocean. Tomita and Honda (2011) developed a numerical model of drifting debris such as vessels, containers, and cars to study object interaction in tsunami-like flows.

Prior research is robust and provides an excellent body of work off which to base further experimental and numerical studies on the complexities of debris interaction within inundations, particularly on debris impacts on a structure. This thesis seeks to improve understanding on this front.

### *1.3 Prior Debris Field Experimentation*

Similar experimental work has provided a basis for the experiment discussed herein. As part of a larger experimental study in 2017, a series of tests were performed at the Large Wave Flume at the NHERI (O.H. Hinsdale) Wave Research Lab at Oregon State University. The test program utilized a test structure, which was a 1:10 model of a two-story elevated coastal structure with piles and simulated bathymetry, which were subject to tsunami-like wave flow. Figure 1.2 shows the test structure in place.

In Alam et al. (2020), tsunami-like wave-induced horizontal and uplift forces on the test structure were evaluated. The experimental design allocated two wave profiles: one unbroken wave with no air gap underneath the structure at still water and one wave designed to replicate a tsunami bore, which had an initial air gap. Three-dimensional pressures were also studied. Large overturning moments were found, as well as a high degree of symmetry in both wave types. The unbroken wave also had highly repeatable wave height, pressure, and force measurements.

Winter et al. (2020) used the same experimental set-up and investigated the effect of macro-roughness elements on the flows (e.g., buildings blocking or channeling flow to a structure of interest). In the case of the experimental regime, concrete blocks were introduced to assess the influence of these adjacent structures on velocity, wave force, and pressures as


Figure 1.2: Test set-up at NHERI Wave Flume in 2017 (from Winter et al. (2020)).

compared to a baseline case without adjacent structures. The study found shielding and wave channeling to be significant effects on loads and pressures. Figure 1.3 shows an example trial.

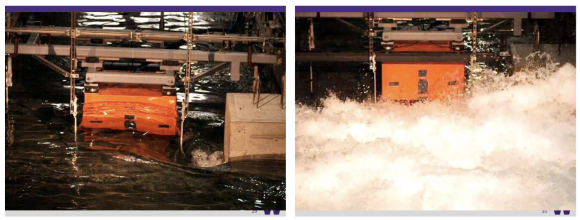

Figure 1.3: Test structure and adjacent structure in flow (from Winter et al. (2020)).

Shekhar et al. (2020) again used the same experimental set-up, but removed all structures except the test structure. As a proof-of-concept, high-density polyethylene (HDPE) debris were introduced using a static initial condition into the flow. The debris were intended to be neutrally buoyant and were varied to represent both structured and unstructured (random) initial conditions with a varying number of debris. Using the same unbroken wave from Alam et al. (2020), the debris were propelled into the test structure, where reaction forces

were measured by load cells in three dimensions. Figure 1.4 shows a structured test set-up with four debris.

Figure 1.4: Debris trial with four debris (from Shekhar et al. (2020)).

From a variety of test conditions, the study found evidence of 1) an initial impact due to the transfer of momentum from the block to the face of the test structure and 2) a low frequency forcing indicative of "damming" (i.e., when debris becomes caught on the structure and partially obstructs flow). Shekhar et al. (2020) discusses this as two distinct events. Additionally, the variation of peak impact and damming forces for trials with and without debris is discussed: debris adds substantial variability in peak forces. Since this experimental program was intended as a proof-of-concept, more trials are needed to understand the highly variable debris-structure interactions.

The experimental design and concepts elucidated from Shekhar et al. (2020) are the basis of the work presented herein. See Chapter 2 for details regarding the experimental set-up.

## *1.4 Objectives*

This document discusses a comprehensive experimental program conducted at the NHERI O.H. Hinsdale Wave Research Laboratory in Spring 2021 in which many trials were conducted with a large variety of initial debris field conditions, enabling quantification of debris field impacts with a test structure. This document represents the first set of results from this dataset, with specific objectives outlined as follows:

- Establish a consistent hydrodynamic reaction force baseline for the unbroken wave.

- Understand single-debris loading scenarios.
- Identify data patterns and trends in peak impact forces and damming
- Extend findings to inform design for highly variable flow-driven debris fields

Ultimately, this data set is intended to be used as a validation set for coupled fluid-structure numerical models, including finite element models (FEM), computational fluid dynamics (CFD), and material point method (MPM). The motivation of this work is to extend scientific understanding of inundation-driven debris fields and add to the growing body of scientific literature toward resilient coastal design. Future publications following this body of work should be referenced for further developments in data analysis and model development.

# Chapter 2

# EXPERIMENTAL DESIGN

## *2.1 Facility*

Testing was performed over a 10-week period at the NHERI O.H. Hinsdale Wave Research Laboratory at Oregon State University in Corvallis, OR. Set-up and experimentation were conducted from mid-February 2021 through mid-May 2021. Approximately three weeks were dedicated to installation and troubleshooting, after which time 410 successful trials with debris were conducted.

The test was conducted in the Large Wave Flume, which is 104-meters long, 3.7-meters wide, and 4.6-meters tall. The Large Wave Flume is made of approximately 0.3-m (12") thick reinforced concrete wall and is divided into 3.65-m long bays starting approximately 10.3-meters from the neutral position of the wavemaker.

The piston-driven wavemaker capable of simulating tsunami-like and swell waves is the full height of the flume and is situated at the south end of the flume. It is capable of driving a variety of wave profiles in water up to 2-meters deep for tsunami-like waves, and 2.7-meters deep for swell-type waves. The origin of the coordinate system is located at $[(x, y, z) = (0, 0, 0)]$ at the bottom of the flume in the center of the front face of the wave maker paddle at its rest position. Positive $x$ is oriented in the streamwise direction of wave propagation, positive $z$ is upward, and positive $y$ is based on a right-hand coordinate system toward the westmost flume wall.

For this experiment, concrete panels were placed on the bottom of the flume to create simulated beach bathymetry and induce run-up. The bathymetry was laid out similarly to previous experiments, such as Winter et al. (2020), Alam et al. (2020), and Shekhar et al. (2020). Figure 2.1 provides plan and elevation views of the flume with bathymetry sloped

at 1:12 then increased to 1:24 with the test structure shown. Also shown is the location of the debris frame, placed 2-meters upstream of the test structure. Unlabeled in the below figure is a slight depth decrease of 0.1524 m located at Bay 2, where the initial bathymetry panel to create is placed. The slabs to create bathymetry were not filled underneath to allow restraint from below as well as above, and thus the region underneath the slabs was not watertight. These slight discrepancies from an idealized test scenario do not significantly impact the dominant hydrodynamic forcing (see Winter (2019) for further discussion).

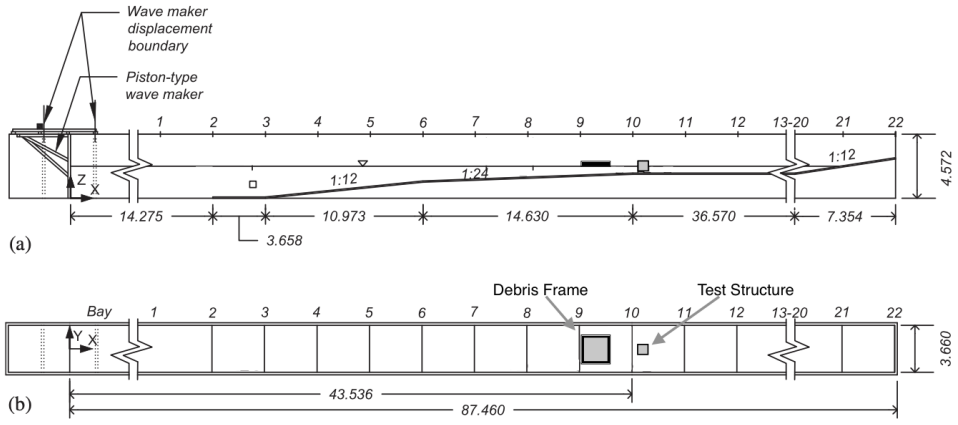


Figure 2.1: Large Wave Flume elevation and bathymetry (top) and plan (bottom) (adapted from Winter et al. (2020)).

The O.H. Hinsdale Wave Research Lab (HWRL) manages a data acquisition system (DAQ) that allows instruments to be synchronized and managed simultaneously. In this experiment, data were acquired mainly at 1200 Hz to allow characterizing high-frequency debris impacts. 1200 Hz was selected since it allows for high-frequency events, is divisible by the highest sampling rates of certain instruments (120 Hz for DOT accelerometers and ADVs), and is under the threshold at which signal "ghosting" occurred in this system. "Ghosting" is the occurrence of nonphysical signals that are a product of large voltage swings on adjacent channels, which increases voltage settling time on adjacent channels. Some early trials were run at 120 Hz; this was only the case for early hydrodynamic (i.e.,

no debris present) trials, which were limited by the maximum sampling frequency of the acoustic doppler velocimeters (ADVs).

### *2.2 Wave Generation*

Two waves were used during this experimental program to simulate an unbroken wave and a broken bore. The unbroken wave is highly repeatable as compared to the broken wave, and thus was used for the majority of testing during which different debris configurations were used. The mechanism by which they are generated and their profiles are discussed in this section.

The Large Wave Flume's wavemaker is a piston-driven, hydraulic actuator assembly that can create a multitude of wave profiles, including regular, irregular, tsunami, and user-defined wave profiles. It has a period range of 0.8 to 12+ seconds and has a max stroke of 4m at 4m/s.

Both wave profiles were studied intensively for various scenarios as documented in Winter et al. (2020), Alam et al. (2020), and Shekhar et al. (2020). Paddle motion was controlled via time histories for paddle displacement. The displacement history for the unbroken wave was specified via an error function, whereas the displacement history for the broken wave was specified using solitary wave theory.

The following represents the paddle history displacement time history as discussed in Winter (2019):

$$x_{wm}(t) = \frac{S_{max}}{2}[1 + erf(\frac{100(t - t_0)}{SF})]$$

where $x_{wm}$ is the position of the paddle, $S_{max}$ is the maximum piston stroke (4m), and $SF$ is a specified scaling factor to stretch the displacement over a specified time. In this case, $SF = 500$. $t_0$ is defined as the initial time offset, which is calculated using $t_0 = 100/\tau_0/SF + t_{wm}$, where $t_{wm} = 10s$ and is the required delay for the data acquisition system after wavemaker start. $\tau_0$ is the solution to $erf(\tau) + 1 = \text{tolerance} = 5e - 5$, which allows displacement to remain at 0 for the initial time period. The scaling factor $SF$ is used to define the amplitude

of the wave. In this case, a relatively small amplitude and long wavelength allowed for the unbroken wave to remain unbroken throughout the testing environment.

For the unbroken wave, the still water level (SWL) was 2.0 m, which represents a water depth of 0.25 m at the test structure. The bottom of the structure is 0.25 m above bathymetry (as discussed further in the next section), so the SWL represented no air gap underneath the structure for the unbroken wave.

The broken wave, as previously mentioned, used a piston displacement time history generated via shallow water and solitary wave theories Winter et al. (2020)). The SWL was 1.85 m, which results in an air gap of 0.15 m beneath the structure and 0.1 m of standing water. The wave height was 1.35 m, which was unstable due to wave steepness and thus broke well before the structure, resulting in an impacting bore. The wavemaker displacement histories are consistent throughout each trial. Sample trials for each wave type are shown in 2.2.

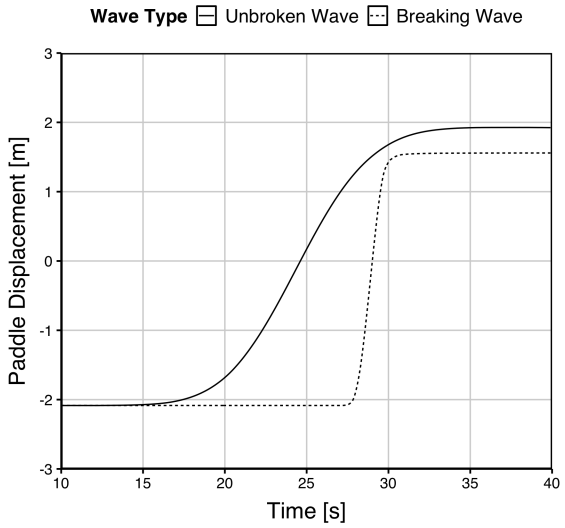


Figure 2.2: Paddle displacement for both wave types.

### *2.3 Test Structure*

A 1.016-meter square base x 0.615-meter tall box constructed with sheet metal and piped steel framing (similar to Alam et al. (2020)) was placed at approximately 43.8 m from the face of the neutral position of the wave maker and was subjected to run-up and follow-on flow. The structure was supported via low-friction bearings from a frame mounted to the flume wall sides, allowing reactions to be measured in the streamwise $x$ and transverse $y$ directions. The test structure was internally supported by a frame of 0.0381-meter hollow steel sections (HSS). These HSS were placed evenly at thirds through the interior in the $y$-direction, and at the halfway point in the $x$-direction. The sections were continued along the top and bottom in both directions to encircle the box. This is very similar to the set-up presented in Winter et al. (2020), Shekhar et al. (2020), and Alam et al. (2020), but with some exceptions. Modifications were made to resolve streamwise loading and provide rotational stiffness. Instead of having one streamwise in-line load cell, two load cells were placed symmetrically across the streamwise centerline of the flume. Additionally, the two load cells were lowered in elevation. Instead of the load cells extending through the support frame, two 1-inch (0.0254-m) thick steel plates sandwiched and bolted-connected around the frame and extending downward allowed for load cells to be connected and the structure to maintain stiffness of connection.

Additional modifications were introduced in the internal structure, in which extendable rods encased with aluminum HSS spanned the load path from the bottom front edge of the test structure to the two streamwise load cells at the back and provided additional stiffness.

Eight load cells were located at the points of attachment from the test structure to the support frame. Underneath the structure were 0.25-m steel "legs", which were not load-bearing but were installed to terminate just above the bathymetry beneath. Unlike previous set-ups (e.g., Alam et al. (2020)), there were no load cells installed on the legs, as the debris field initial conditions occurred much higher than the legs due to their buoyancy within the flow. Figure 2.3 shows the test structure and support structure. Figure 2.4 provides further

dimensions of test structure instrumentation. Figure 2.5 show images of the test structure in place.

In Figure 2.3, the numbered labels correspond as follows: (1) design structure body, (2) pressure gauge positions, (3) design structure legs, (4) pancake uni-directional load cell, (5) in-line load cell, (6) flume wall-mounted frame support beam, (7) streamwise support frame section, (8) transverse support frame section, (9) streamwise low-friction bearings, (10) transverse low-friction bearings, (11) bearing attachment block, (12) threaded-rod connections between the support frame and flume wall-mounted beams, and (13) HSS stiffener braces.

## *2.4 Instrumentation*

Instrumentation was present within the structure (attached to the support frame for the test structure) and attached to the flume walls. The following section will document the instrumentation location and functionality. Table 2.1 shows the locations and names of each instrument used during testing. Figure 2.4 shows the locations of the instruments attached to the test structure. Figure 2.6 shows the location of instruments located within the flume.

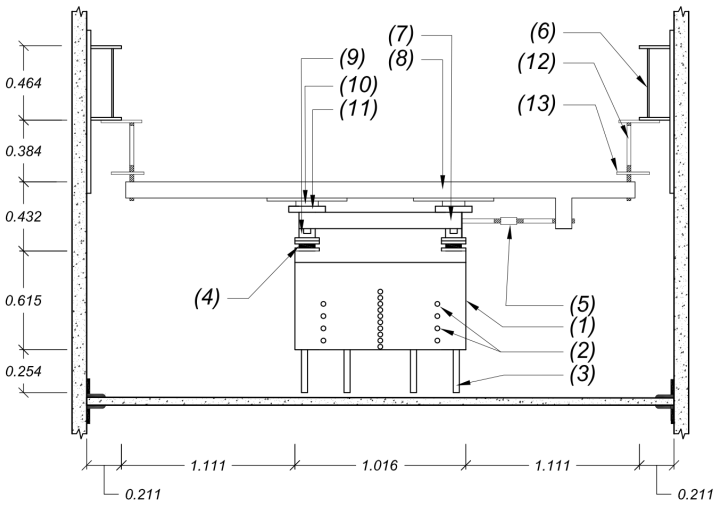


(a) Front view (wave propagation into page)

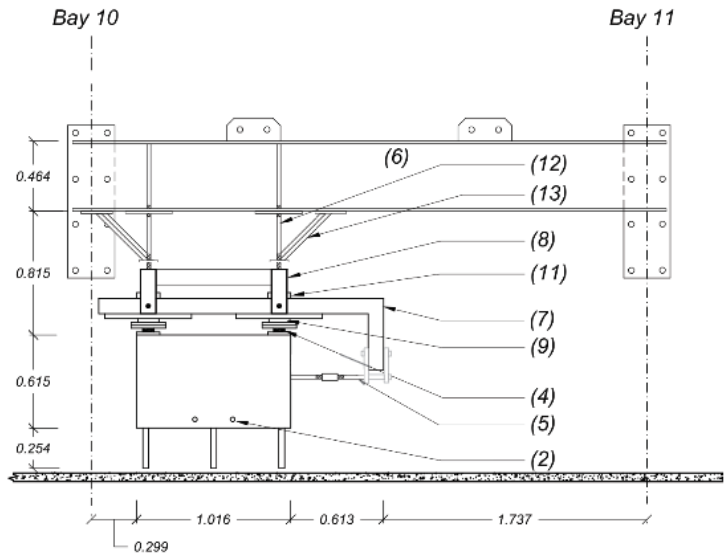


(b) Side view (wave propagation to right)

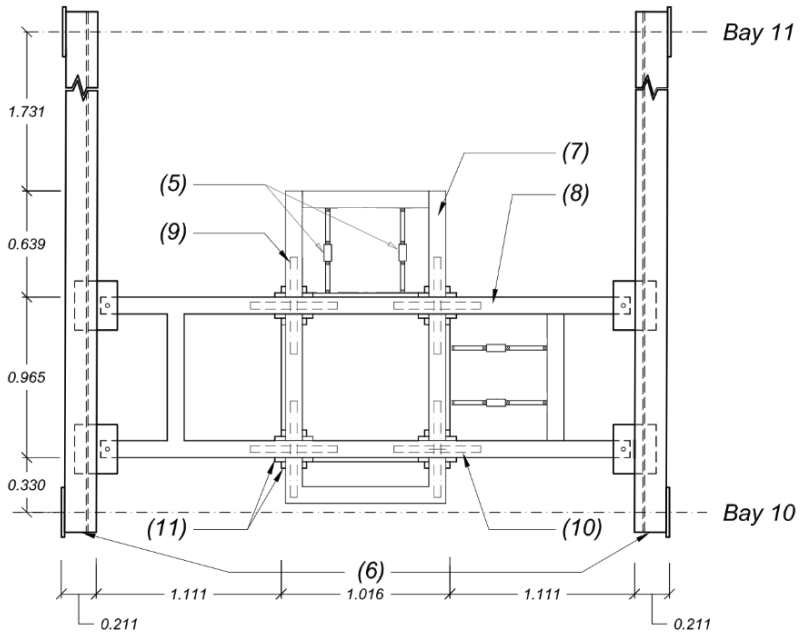


(c) Top view (wave propagation to top of page)

Figure 2.3: Elevated structure and instrumentation plan and elevation views (adapted from Alam et al. (2020))).

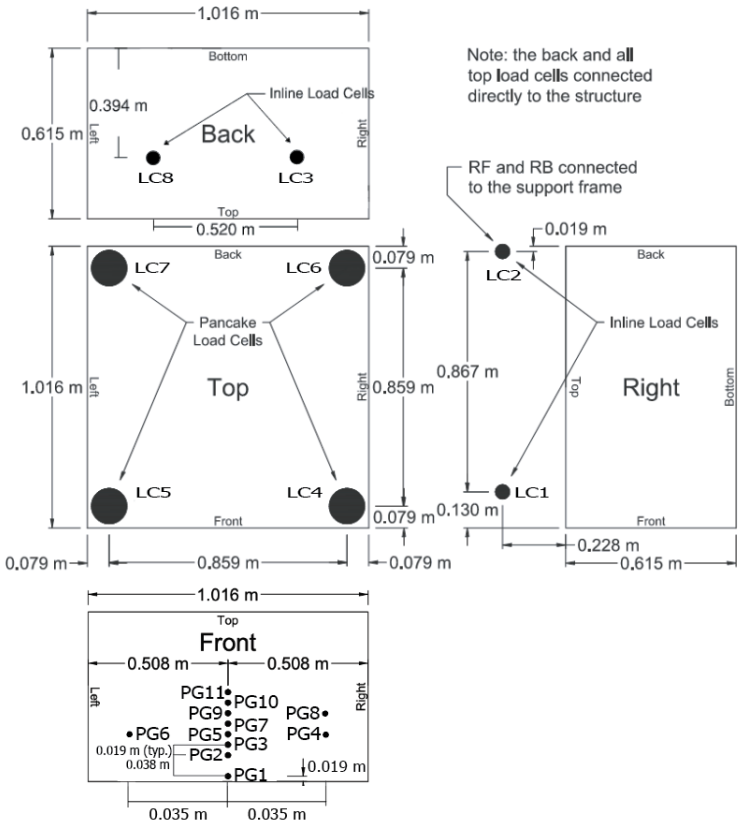


Figure 2.4: Test structure instrumentation (adapted from Winter et al. (2020)).

(a) Test structure in flume

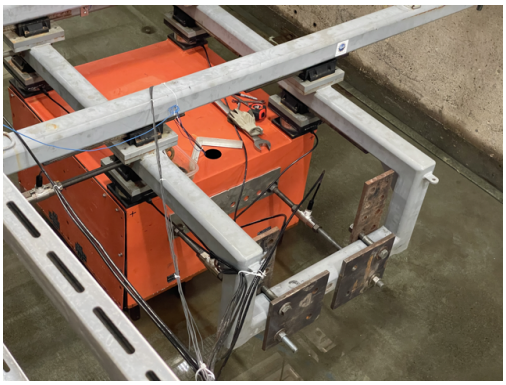

(b) Attachment plates for streamwise load cells

(c) Internal structure of test structure; threaded rods and HSS provide stiffness from front bottom edge of box to the streamwise load cells.

Figure 2.5: Photographs of test structure.

Table 2.1: DAQ Instrument Locations in LWF

| Name | Type | X [m] | Y [m] | Z [m] |
|---|---|---|---|---|
| wg1 | wire wave gauge | 13.992 | -1.391 | NA |
| wg2 | wire wage gauge | 32.269 | -1.361 | NA |
| wg3 | wire wage gauge | 36.114 | -1.372 | NA |
| uswg1 | ultrasonic wage gauge | 39.602 | -1.303 | 3.638 |
| uswg2 | ultrasonic wage gauge | 43.227 | -1.303 | 3.374 |
| uswg3 | ultrasonic wage gauge | 43.116 | -0.009 | 3.663 |
| uswg4 | ultrasonic wave gauge | 44.264 | -1.293 | 2.748 |
| uswg5 | ultrasonic wave gauge | 46.929 | -1.301 | 3.369 |
| uswg6 | ultrasonic wave gauge | 46.925 | 0.076 | 3.357 |
| adv1 | acoustic doppler velocimeter | 13.981 | -1.425 | 0.636 |
| adv2 | acoustic doppler velocimeter | 35.913 | -1.412 | 1.542 |
| adv3 | acoustic doppler velocimeter | 43.237 | -0.526 | 1.766 |
| adv4 | acoustic doppler velocimeter | 43.246 | 0.509 | 1.765 |
| adv5 | acoustic doppler velocimeter | 44.260 | -1.319 | 1.759 |
| adv6 | acoustic doppler velocimeter | 44.255 | -0.005 | 1.796 |
| adv7 | acoustic doppler velocimeter | 46.948 | 0.017 | 1.768 |
| press1 | pressure sensor | 43.790 | -0.005 | 2.028 |
| press2 | pressure sensor | 43.788 | -0.004 | 2.104 |
| press3 | pressure sensor | 43.787 | -0.005 | 2.180 |
| press4 | pressure sensor | 43.787 | -0.361 | 2.218 |
| press5 | pressure sensor | 43.786 | -0.004 | 2.219 |
| press6 | pressure sensor | 43.791 | 0.351 | 2.220 |
| press7 | pressure sensor | 43.786 | -0.006 | 2.256 |
| press8 | pressure sensor | 43.787 | -0.360 | 2.293 |
| press9 | pressure sensor | 43.787 | -0.005 | 2.294 |
| press10 | pressure sensor | 43.786 | -0.005 | 2.341 |
| press11 | pressure sensor | 43.788 | -0.005 | 2.372 |
| load1 | in-line load cell | 43.916 | -0.840 | 2.859 |
| load2 | in-line load cell | 44.783 | -0.845 | 2.855 |
| load3 | in-line load cell | 44.783 | -0.275 | 2.405 |
| load4 | pancake load cell | 43.850 | -0.446 | 2.690 |
| load5 | pancake load cell | 43.848 | 0.415 | 2.694 |
| load6 | pancake load cell | 44.715 | -0.438 | 2.688 |
| load7 | pancake load cell | 44.711 | 0.424 | 2.691 |
| load8 | in-line load cell | 44.790 | 0.245 | 2.404 |

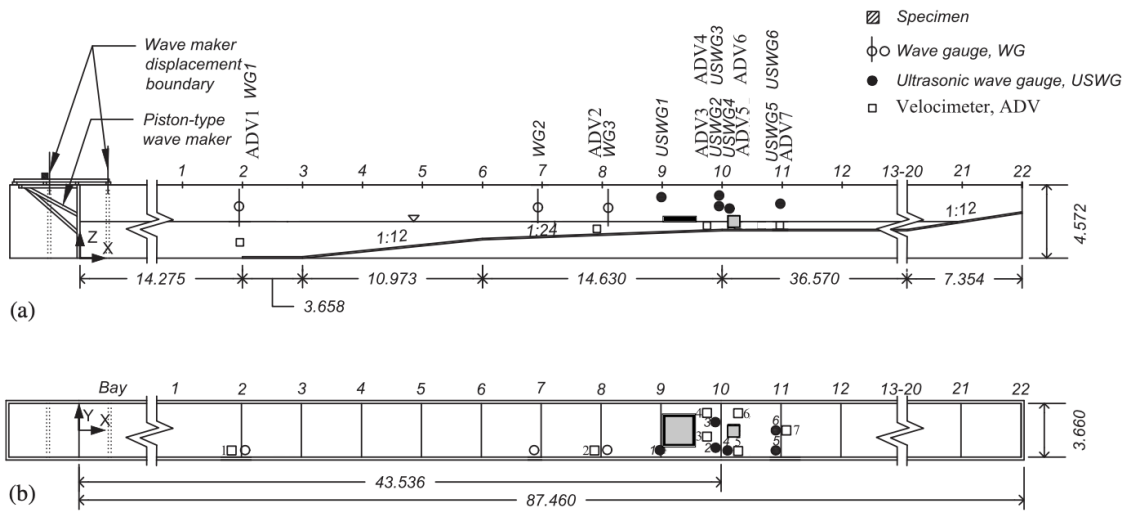


Figure 2.6: Flume instrumentation (adapted from Alam et al. (2020)).

### *2.4.1 Wire & Ultrasonic Wave Gauges*

Three wire wave gauges were attached to the wall of the flume. An additional wave gauge is intrinsic to the wavemaker system and is termed the "wavemaker wave gauge". The wire wave gauge nearest to the test structure was located upstream of the structure to reduce the likelihood of contact with debris. Wire wave gauges measure free surface elevation via changing electrical resistance along a wire which is partially submerged.

Six ultrasonic wave gauges were positioned near the structure. Unlike wire wave gauges, their signal is acquired via high-frequency acoustic reflection; there are no portions of the instrumentation that are submerged before, during, or after a wave event, so they are used around the structure during debris experiments. However, they are prone to signal oversaturation due to splashing.

Both wire and ultrasonic wave gauges were connected to the DAQ and sampled at 1200 Hz. Figure 2.6 shows all wave gauge positions for both wire and ultrasonic wave gauges. Elevations of ultrasonic wave gauges (shown in Table 2.1 are intended to avoid splashing and signal saturation during wave events while also avoiding instrumentation and/or structure underneath their signal path.

### *2.4.2 Acoustic Doppler Velocimeters*

Seven acoustic doppler velocimeters (ADVs) were used during testing without debris. They were removed for subsequent trials due to the risk of damage from debris impact. ADVs operate by emitting sound and using Doppler shift principles to detect fluid velocity in three dimensions. They recorded under the minimum free surface elevation to prevent data corruption due to entrained air and recorded flow around and underneath the test structure.

ADVs, unlike other instruments connected to the DAQ, were limited to sampling at 120 Hz. Since they were not present during debris trials, only certain wave-only trials were sampled at this lower frequency. In general, most wave-only data comes from trials conducted after ADVs were removed as a consequence of experimental sequencing. However, due to

the consistency of the generated flow profile, ADV data can still be used to understand the hydrodynamics throughout the experimental program. Further discussion of wave-only tests is provided in Chapter 3.

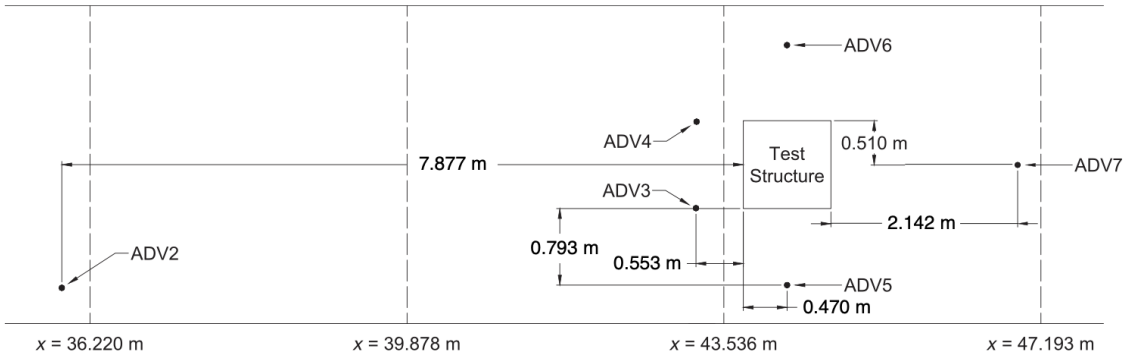


Figure 2.7: Acoustic doppler velocimeter locations near test structure (adapted from Winter et al. (2020)).

### *2.4.3 Pressure Sensors*

Eleven pressure sensors were installed on the front face of the test structure (facing the wave maker). As was the case with the ADVs mentioned in the previous section, they are sensitive to impact from debris, and thus were removed during trials with debris. Due to the consistency of hydrodynamics, they are assumed to be relevant to the entire testing program, as will be discussed further in Chapter 3. They were present during trials limited to 120 Hz due to the ADVs; thus, their maximum sampling frequency was 120 Hz. Previous validation and understanding of pressure sensors in a similar experimental setup were explored in Winter et al. (2020). Figure 2.6 shows the location of the pressure sensors for trials without debris. Note: piezoelectric pressure sensors were left in place and recorded throughout; however, they are not included in this scope of work due to unreliable data.

### *2.4.4 Accelerometers*

Two triaxial accelerometers were in place on the test structure during all trials; however, they are not included in this scope of work.

### *2.4.5 Load Cells*

Instrumentation included eight load cells. Two in-line streamwise load cells connected the back face of the test structure to the support frame, two in-line transverse load cells were attached to the right side of the test structure if facing in the direction of flow, and four pancake (vertical direction) load cells on the four top corners of the orange measured uplift forces. Each load cell was connected to the DAQ and sampled at 1200 Hz when ADVs were not connected (most trials). In-line and transverse load cells measure load via strain gauges calibrated with known stiffness. All load cell data is taken as a displacement that is not dependent on an initial reading (i.e., the strain is linear-elastic in the region of measured loads). Therefore, the initial readings of the load cells are taken to be 0, and the magnitude of the change in load is recorded. Figure 2.4 shows the locations of all load cells as attached to the test structure.

### *2.4.6 Cameras*

Throughout the experiment, one Edgertronic high-speed camera and one GoPro Hero 8 were used for at least two trials per test configuration. The GoPro was mounted on unistrut out of the way of the "lift" frame crane path and was able to be connected to computers outside the wall of the flume (i.e., operators could connect a cable without removing the camera from the flume), though it was started and stopped remotely. While one location was used for the majority of testing, known lengths are visible throughout all frames, which allows for dimensional and velocity data to be read from video. Additionally, LED lights that are synced with an unambiguously random signal generated by the DAQ allow synchronization between external video data and DAQ instrumentation data. In general, GoPro camera data

was recorded at 120 frames per second and was focused on recording the initial condition and debris path.

The high-speed camera was also mounted to unistrut above the debris path and was operated manually from outside the flume. The high-speed camera focused on recording images of debris collision with the front face of the test structure at 500 frames per second. To allow synchronization with DAQ data, an LED light was visible in all frames of recorded video.

### *2.4.7 Debris-Mounted Accelerometers*

Debris-mounted accelerometers (called DOTs) were used during at least two trials per test, and were used during the same two trials during which both cameras were fully operational. They are manufactured by Xsens and are intended to capture accelerations and orientations to reconstruct trajectories. They have been used in applications with human movement, but never in a fluid-structure-impact setting. They showed promise in reconstructing debris trajectories in fluids applications since they are small, light, fairly inexpensive, impact-resistant, waterproof, and can be operated remotely via Bluetooth. While they are capable of showing live data, they were used in "recording only" mode and thus could only be operated at 120 Hz.

DOT accelerometers were placed in a compartment within the debris (discussed in the next section). A maximum of four accelerometers were used at a time, with a fifth accelerometer located outside of the flume and attached to a solenoid, which was synced with the unambiguously random signal generated to synchronize external instruments to the DAQ. The DOTs' timing was synced before the trial so that the DOTs all could be paired with DAQ signal. DOTs were charged overnight and used throughout daily trials.

Data collected from Xsens DOT accelerometers are outside of the scope of this thesis, but will be discussed in future work.

### *2.5 Debris*

Debris fields were experimentally simulated using debris pieces made of high-density polyethylene (HDPE). The debris were 0.5-meters x 0.051-meters x 0.102-meters and weighed approximately 2.52 kilograms. A maximum of twenty-four full-sized pieces were used. The density of HDPE is 988 $kg/m^3$ (i.e., approximately neutrally buoyant in fresh water) and Young's modulus is 0.8 GPa. The draft of the debris was 5 cm. Figure 2.8 shows the dimensions of a typical debris piece.

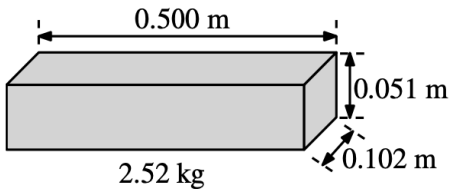


Figure 2.8: Typical debris dimensions (adapted from Alam et al. (2020)).

Debris were outfitted with a compartment for debris-mounted accelerometers (discussed in Section 1.4.7). The construction required a hole at the geometric center of the HDPE block to allow for the accelerometer to be oriented specifically. The compartment was machined to have a DOT compartment, and was attached via pre-drilled holes through the HDPE and into the steel when the electromagnetic system was used. The compartment could also be attached using screws into HDPE if no steel was present (see Figure 2.9).

In addition to the compartment for onboard DOT accelerometers, a steel plate was optionally available during trials using the electromagnetic frame (discussed in Section 1.7). The steel plate was approximately 1/2" (1.27-cm) thick and 2-5/8" (6.6675-cm) in diameter. The steel plate allowed a magnetic attachment surface for the electromagnets at approximately the center of the debris. To maintain neutral buoyancy and draft, portions of HDPE were selectively removed to maintain axial symmetry but reduce overall weight and filled with foam sealant to: a) prevent changes in the debris surface for comparison between trials

and b) keep the debris watertight and buoyant. Additionally, a small 3/8" (0.9525-cm) deep and 1-5/8" (1.6675-cm) diameter hole (where the electromagnet would attach to the embedded steel plate) was present on the top center. Modifications to the stiffness of the overall block are assumed negligible in this experimental context. Figure 2.9 shows a modified debris (prior to the removal of HDPE for buoyancy). When no plates were present in the debris, styrofoam was used to replace the steel plate and seal the compartment and accelerometer in place.

Figure 2.9: Debris with accelerometer compartment removed and Xsens DOT accelerometer.

## *2.6 Debris Lift Frame*

Debris frames held in place the initial conditions for debris configurations and/or released the debris into the wave path. For the purposes of this scope of work, two types of frames were utilized. The "lift" or "wood" frame was used for the majority of debris tests. The debris area was located 2-meters upstream of the front face of the test structure to the downstream

most edge of the structure and centered in the width of the flume. All tests were conducted with the front face of the initial debris field 2 meters from the front face of the structure and with the debris field extents axisymmetric about the streamwise centerline of the flume.

The lift frame was modeled closely after the system used by Shekhar et al. (2020). It was comprised of (4) 2-inch x 10-inch (5.08-cm x 25.4 cm) pieces of lumber as primary structural support and additional smaller 1-inch x 12-inch (2.54-cm x 30.48-cm) plywood pieces. Two 2-inch x 10-inch (5.08-cm x 25.4 cm) lumber pieces nearly the same width of the flume were positioned 2 meters from each other (perpendicular to the direction of flow). The flume width was approximately 3.65 meters, so the primary lumber pieces were approximately 3.6 meters. This dimensioning provided rotational stability for the frame and also allowed the frame to be lifted without contacting the sides of the flume (which, due to construction tolerances, are not uniformly plumb).

Spanning the two perpendicular 2-inch x 10-inch (5.08-cm x 25.4 cm) pieces were two secondary 2-inch x 10-inch (5.08-cm x 25.4 cm) pieces, connected with bolts. They were separated by 2 meters and bolted to the primary structural support to create a rigid 2-m x 2-m internal area. The entire assembly was attached via rigging eyebolts at four points, and the rigging was centered to allow the crane to lift at exactly the center of the 2-m x 2-m internal area.

Secondary 1-inch x 12-inch (2.54-cm x 30.48-cm) plywood pieces boards were cut to varying lengths and slotted to allow for their adjustment between trial configurations. In some cases, the boards held the debris in an exact, tightly packed position; in other cases, the boards defined a maximum debris field extent and the debris was allowed to float freely in that area. Figure 2.10 shows the wood frame.

The “lift”/“wood” frame was allowed to float on the surface, with enough tension in the rigging to hold it stationary at 2m from the front face of the test structure. The crane was operated by the research team and was lifted above the maximum wave height before the wave reached the initial debris field. The lift frame was used for the majority of the testing due to its ease of use and because it maintained a stationary initial debris field.

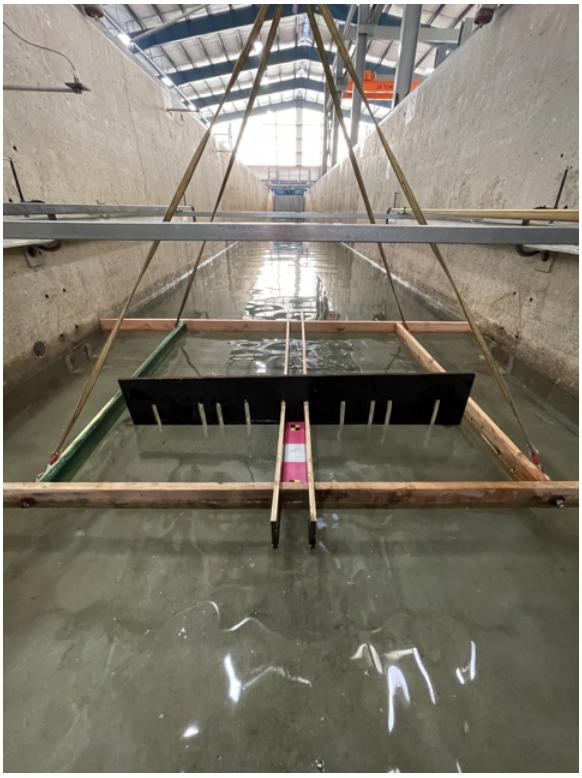

Figure 2.10: Wood frame in the flume with single debris.

## *2.7 Debris Drop Frame*

The “drop” or “electromagnetic” frame was used for a subset of tests; all configurations tested on the “drop” frame were tested also using the “lift” frame. The “drop” frame was used due to its strength in providing chaotic, randomized conditions. The debris area was located 2-meters upstream of the front face of the test structure to the downstream most edge of the structure and centered in the width of the flume. The “drop” frame was comprised of two pieces of latticed steel fencing, bolted together side by side, which created a grid of approximately 1” x 1” (2.54 cm x 2.54 cm) and exceeded the total maximum frame area (2m x 2m). The grid allowed for precise layout of electromagnets to which debris would be attached. The structural support for the latticed steel fencing was unistrut spanning across the flume underneath the front and back (streamwise) edges. Unistrut supported the

transverse edges and spanned the primary struts in the streamwise direction. Along the top face of the frame, unistrut spanned the flume and was attached to the lattice via pipe straps. All transverse struts were attached to channels mounted to the flume side by structural clamps. The front face of the lattice was 2 meters from the front face of the test structure. The bottom side of the assembly (from which the debris would hang) was approximately 1-m from the free surface in the case of a 2-m SWL so that debris would fall approximately 0.91 m (36”). This dimension was determined since it both cleared the maximum wave crest for the unbroken wave (approximately 0.25m; the only wave condition used with the “drop” frame) and allowed the minimum feasible working height underneath. The assembly was supported by (4) crane rigging attachment points, with the crane supporting the structure in place for the duration of its use. Figure 2.11 shows the electromagnetic frame.

Figure 2.11: Electromagnetic/drop frame from underneath.

Debris were attached to the “drop” frame via electromagnets that were screwed to small aluminum channels. The weight limit for the electromagnets was approximately 11 kg, which provided sufficient capacity for individual debris pieces. Electromagnet locations were manually moved between test configurations. Unlike using the “lift” frame which allowed debris to float freely within a specified area, the debris centers were placed in predetermined locations (albeit, within a specified area). However, rotating the debris around the specified

center point and the fact that the debris fell into the water allowed for highly random initial conditions.

Additionally, randomness in the initial condition was introduced via the fact that the steel plate was slightly higher than the geometric center of gravity of the debris; therefore, debris was likely to roll when it impacted the water surface so that the steel plate was in a stable equilibrium position. This introduced motion into the initial debris field, which was captured by GoPro video throughout most trials.

Due to test sequencing, tests that occurred before the installation of the electromagnetic frame were conducted with debris that had styrofoam in lieu of steel to enclose the accelerometer compartment. This was to maintain neutral buoyancy.

Tests occurring after the initial installation of the electromagnetic frame (including those using the lift frame after the electromagnetic frame was removed) generally had steel plates and had HDPE removed and filled with a lightweight foam and sealant. Occasionally, steel plates were removed and replaced with styrofoam in order to maintain neutral buoyancy. Only 16 of the initial 24 full-sized debris were subjected to this modification where HDPE mass was removed.

In trials using "multi-sized" debris, the remaining 8 of 24 full-sized debris were cut to remove the two end quarter-lengths. This provided 16 "quarter-sized" debris and 8 "half-sized" debris. Both of these smaller-sized debris were not available for use by the electromagnetic frame (as they could not contain a steel plate) and were only used with the lift frame.

### *2.8 Testing Sequence*

Testing was conducted over a period of several weeks. On average, each trial lasted approximately 200 seconds. To allow for the water to settle and reset the test configuration, tests occurred approximately every 20 minutes. In general, one person operated the DAQ, while another person oversaw and/or conducted manually setting the initial conditions and operating the crane (for "lift" frame trials), cameras, and DOT accelerometers (which required remote manual control).

Non-debris testing consisted of wave-only (hydrodynamic) testing for both unbroken and breaking waves. Additionally, system testing to understand load transfer and system stiffness was conducted and included: quasi-static/push testing, hammer testing, and in-air/swing testing. Debris tests varied along several variables, as follows: a) number of debris, b) debris configurations, c) size of individual debris pieces, d) type of frame, and e) type of wave. In roughly chronological order, the tests were sequenced as follows:

1. Hydrodynamic (wave-only testing) before load cell modification (i.e., relevant data from pressure sensors, ADVs, wave gauges)

   (a) unbroken wave only

   (b) breaking wave

2. Hydrodynamic testing after load cell modification (i.e., relevant data from load cells and wave gauges)

   (a) unbroken wave only

   (b) breaking wave only

3. Debris Testing

   (a) unbroken wave, "lift"/wooden frame, full-sized debris, regular (tightly-packed) configurations

   (b) unbroken wave, "lift"/wooden frame, full-sized debris, random (dispersed) configurations

   (c) unbroken wave, "lift"/wooden frame, multi-sized debris, regular and random configurations

   (d) unbroken wave, "drop"/electromagnetic frame, full-sized debris, random (dispersed) configurations (note: only random configurations were tested since the drop frame was suitable only for random testing)

(e) breaking wave, “lift”/wooden frame, full- AND multi-sized debris, regular AND random configurations

4. Structural System Testing

(a) Quasi-Static/Push Tests: A load cell was attached to a steel rod, then the rod was pushed manually into the box at various locations (i.e., a known load was applied at a known location).

(b) Hammer Tests: A load cell-outfitted hammer was used to strike the box at a known force and a known location.

(c) In-Air/Swing Tests: A debris of known mass was attached to a pendulum with neutral at the face of the box; swinging from various distances allowed the application of a known load.

Items 1.a. and 2.a. are explored in Chapter 3. Items 3.a., 3.b., and 3.c. are discussed in Chapters 4 through 6, respectively. All other items will be discussed in future work.

# Chapter 3

# RESULTS OF HYDRODYNAMIC (WAVE-ONLY) TESTS

Tests were conducted to understand the flow properties for the unbroken wave conditions discussed in Chapter 2. In this chapter, the data collected during these trials are presented to: a) build upon and corroborate prior research within a similar testing environment (i.e., Shekhar et al. (2020)) and b) set a baseline of flow conditions for trials without debris.

As discussed in Chapter 2, an unbroken wave with still-water level (SWL) = 2m was chosen to maintain consistent flow properties throughout the experimental program. Several trials were conducted with just the unbroken wave to understand the free-surface elevation, flow velocity, and structural loading in the absence of debris. Due to experimental logistics and modifications after preliminary data analysis to increase test structure stiffness, early trials do not have reliable structural loading data, and later trials do not have velocity data (as acoustic doppler velocimeters (ADVs) were removed to prevent damage due to debris impacts). For simplicity, the tests are further referred to as "Pre-Stiffening" and "Post-Stiffening" to denote before and after test structure stiffening.

## *3.1 General Data Processing*

### *3.1.1 Downsampling Outside of Primary Wave Event*

In early hydrodynamic (wave-only) trials, the presence of the ADVs limited the sampling frequency to 120 Hz. In later trials, the ADVs were removed and the sampling frequency was increased to 1200 Hz to capture high temporal resolution of high-frequency impacts. Given the large quantity of data, downsampling was applied to all 1200 Hz trials outside of the wave event time (from 25 to 50 seconds). During the wave event, all instrument data maintained the full sampling rate. Outside of the wave event (before 25 and after 50 seconds),

downsampling was applied to transform the data sets to 20 Hz. Figure 3.1 shows an example of downsampling applied to a load cell data set from an unbroken wave trial sampled at 1200 Hz as compared with the original data set. Given the high degree of similarity between the two data sets, the remaining analyses are conducted with the downsampled 1200 Hz sets. For sets at 120 Hz, no downsampling is applied.

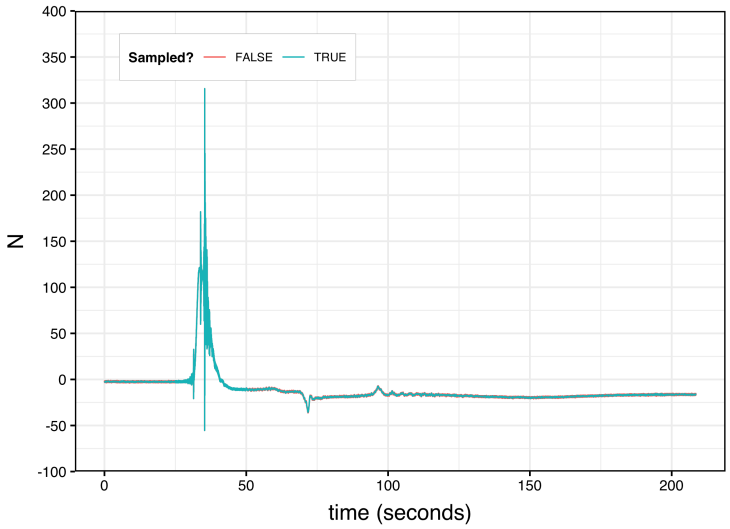


Figure 3.1: Example of sampling strategy for a selected trial (single longitudinal debris subject to unbroken wave, load cell 3).

### *3.1.2 Setting Zero Baseline For Instrumentation*

Instruments connected to the data acquisition system (DAQ) measure the magnitude of a given quantity from a predefined baseline. Free-surface elevation, loads applied to the structure, and velocities in the flume were assumed to have a value of 0 at the beginning of the test. Initial readings are generally set to 0 in post-processing. In particular, load cells use strain gauges, and an initial strain does not move the instrumentation out of a linear elastic range. Therefore, the measured loads can be read as a deviation from an initial value.

For ease of comparison between trials, instruments are set to 0 at the start of experiment time by averaging the first second of data points and subtracting that average value from all data points in the time history, effectively "taring" instruments at the beginning of each trial.

### *3.2 Free-Surface Elevation*

Free-surface elevation in all unbroken wave tests was measured via three wire wave gauges and six ultrasonic wave gauges. Refer to Figure 2.6 for the location and layout of the instrumentation. This discussion provides context for the high repeatability of the wave between trials and between the two test series conducted (before and after the removal of ADVs).

In both the early unbroken wave trials and later trials that occurred after structural stiffening, a total of six trials were conducted during each phase. Figure 3.2 shows all twelve trials for both test series. The consistency both between the tests and among each test's trials for the full time history indicates that there is consistency in the free-surface elevation. We observe the main wave event passing the wire wave gauge at the initial maximum peak, then returning to a baseline near 0 as the wavemaker retracts and reflected wave motion decreases toward 200 seconds. Additional peaks are due to wave reflections in the flume and are outside of the time interval of the significant wave event. Figure 3.3 shows the period of time during which the wave event occurs. For all following wave gauge discussion, the time interval is narrowed to 15 to 60 seconds experiment time to focus on the primary wave event.

Between the three plots, we see the wave shape is consistent in the temporal domain, with the peak free-surface occurring at approximately 27.50, 31.65, and 32.88 seconds, respectively, as the wave propagates toward the test structure and passes through the wave gauge points. The peak of the wave travels at a velocity of approximately 4.4 m/s between wave gauges 1 and 2 and 3.1 m/s between wave gauges 2 and 3. This observation is consistent with slowing due to the increase in bathymetry elevation according to shallow water shoaling. The height of the wave increases from approximately 0.20 meters at wave gauge 1 to 0.24

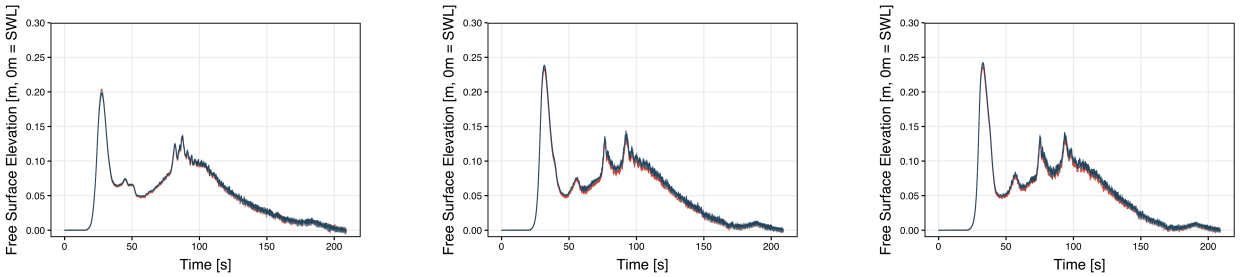


(a) WG1 full time history (b) WG2 full time history (c) WG3 full time history

Figure 3.2: Wire wave gauges full time histories: RED gradient indicates trials during the later "Pre-Stiffening" test; BLUE gradient indicates trials during "Post-Stiffening" test.

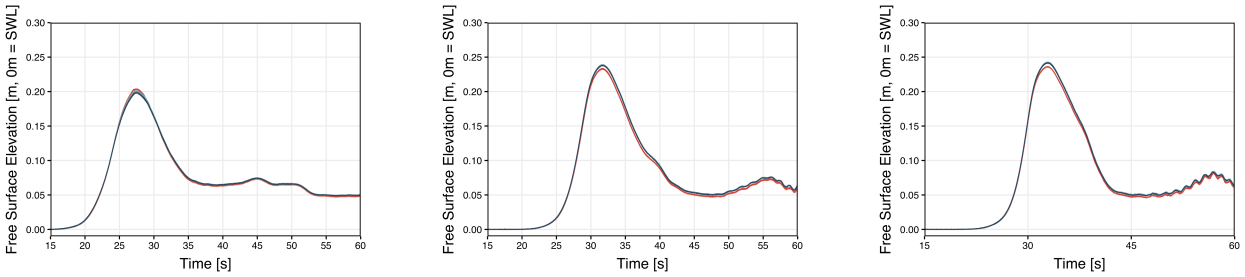


(a) WG1 (b) WG2 (c) WG3

Figure 3.3: Wire wave gauges time histories between 15 and 60 seconds (passing of wave): RED gradient indicates trials during the later "Pre-Stiffening" test; BLUE gradient indicates trials during "Post-Stiffening" test.

m at wave gauge 2 and wave gauge 3. This is also consistent with run-up on increasingly shallow bathymetry.

Ultrasonic wave gauges show similar consistency, although there is more noise present in the measurements. In this case, all trials are shown for both tests. While the low-frequency signal of the passing wave is clear, there is a substantial amount of noise. This is due largely to instrumental noise in the case of the unbroken wave, where there is minimal splashing that could saturate the USWG signal. Both "pre-" and "post-stiffening" tests show considerable noise, but at different instruments. Figure 3.4 shows all six ultrasonic wave gauges. Note that there is a portion with significant error affecting USWG4 in "pre-stiffening" tests. These trials are left for completeness but do not represent a true drop in water level.

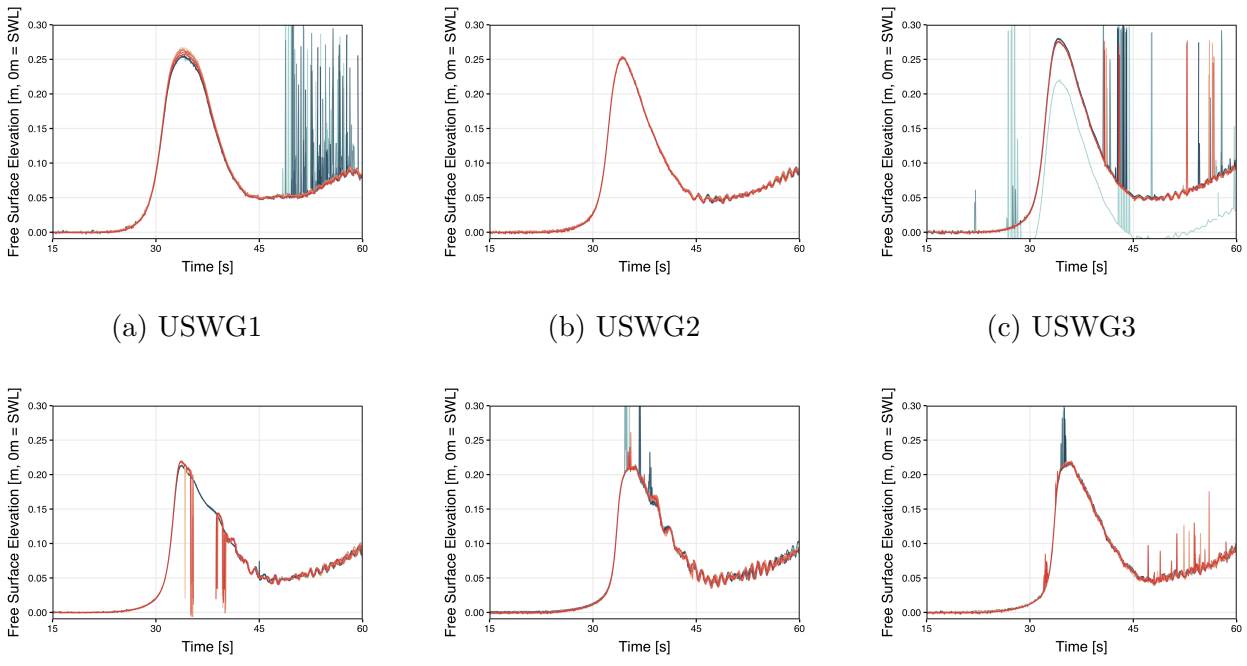


(a) USWG1 (b) USWG2 (c) USWG3

(d) USWG4 (e) USWG5 (f) USWG6

Figure 3.4: Ultrasonic wave gauges time histories between 15 and 60 seconds (passing of wave): BLUE gradient indicates trials during the later "Post-Stiffening" test; RED gradient indicates trials during "Pre-Stiffening" test.

Again, the consistency and repeatability of the unbroken wave are observed within these plots. While ultrasonic wave gauges give noisier data, they are useful in that they can be closer to the structure and debris field in future trials (as they would not be impacted since no portions are submerged).

Considering wire wave gauge WG3 (due to its proximity to the structure), we see that the unbroken wave reaches a maximum free-surface elevation of 0.239m +/− 0.004m from the SWL = 0 in all cases. USWG 3 gives an estimate of the wave height right before the test structure is contacted (removing the erroneous trial that starts below 0 in the "post-stiffening" trials) as 0.278 m.

### *3.3 Flow Velocity*

As shown in the above section, there is a high degree of consistency among the trials of the unbroken wave. Therefore, we can conclude that the wave produced by the wavemaker was highly repeatable. One can extend the conclusions from ADVs (only present during "pre-stiffening" tests) to future testing. ADV data is given in all three dimensions, where $u$ = streamwise velocity, $v$ = cross-stream velocity, and $z$ = vertical velocity at Eulerian points demarcated by the location of ADVs.

In this scope of work, the flow velocities can only be measured without debris present due to the sensitivity of ADVs to impact. However, ADV measurements were discussed in detail in Winter et al. (2020) with regards to changes in velocity due to flow shielding. Given this understanding, flow is assumed to be unaffected by mobile debris fields and thus ADV data collected during trials without debris can be applied to trials with debris.

The predominant flow direction is in $x$ (i.e., streamwise); therefore, the highest velocities are seen in $u$. Any transverse velocities, $v$, and vertical velocities, $w$, are small compared to the dominant flow properties. Each of the five recorded trials is shown in Figure 3.5 for each component of velocity for the first two ADVs, which are located upstream of the structure, with ADV1 being located closest to the wavemaker and ADV2 located approximately 7.8 meters upstream of the test structure. Note that while six trials were conducted during the

"pre-stiffening" unbroken wave only tests, only five trials recorded ADV data.

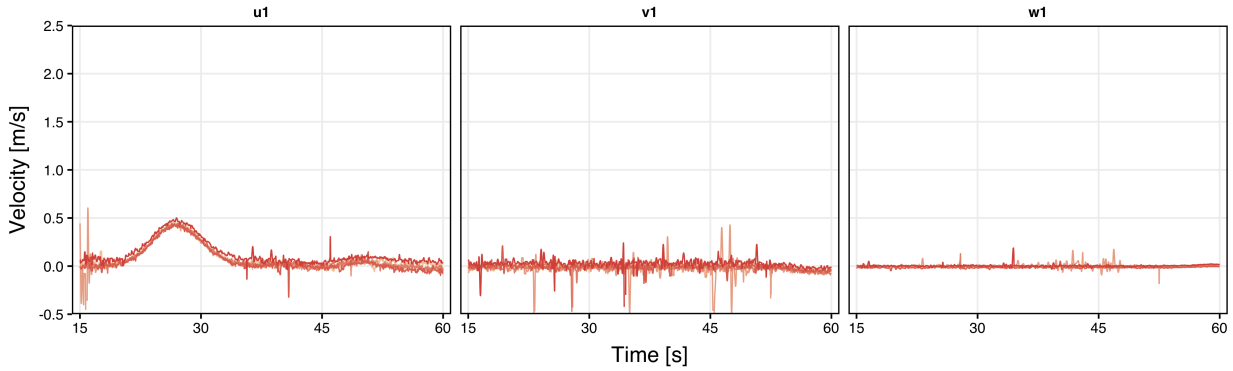


(a) ADV1; 1.364 m below SWL

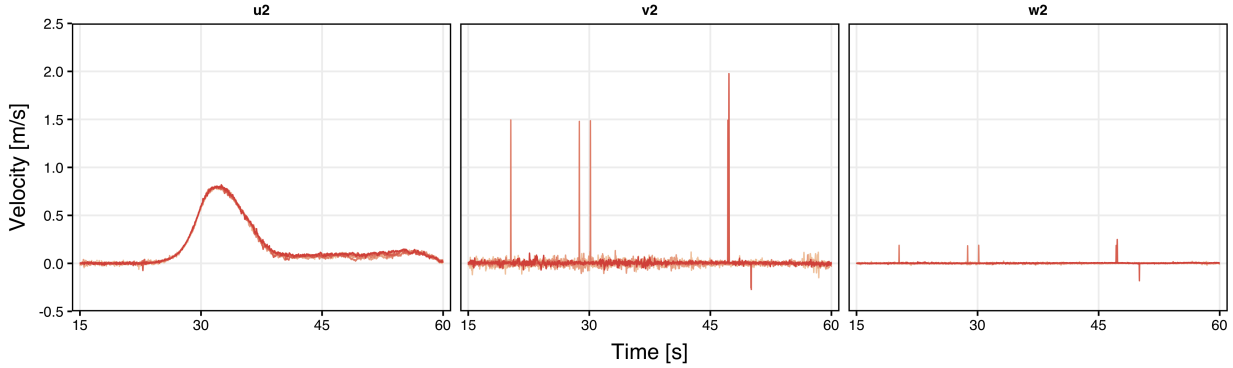


(b) ADV2; 0.458 m below SWL

Figure 3.5: ADVs 1 and 2 for "Pre-Stiffening" unbroken wave trials; sampled at 120 Hz without filtering. Color gradient shows different trials.

The peak streamwise velocity increases as the wave propagates toward and over the simulated bathymetry. The maximum offshore velocity in the streamwise direction measured before full run-up and contact with the structure is a median value of 0.809 m/s.

ADVs 3 and 4 are approximately 0.5 m upstream of the structure and are aligned with

the corner of the front face of the structure. They are submerged 0.234 m below SWL. Figure 3.6 shows the time histories for ADVs 3 and 4. The measured streamwise velocities were consistent between the two velocimeters, with median peak values at approximately 0.959 m/s and 0.990 m/s respectively. These values are taken to represent the peak velocity before the wave contacts the front face of the structure.

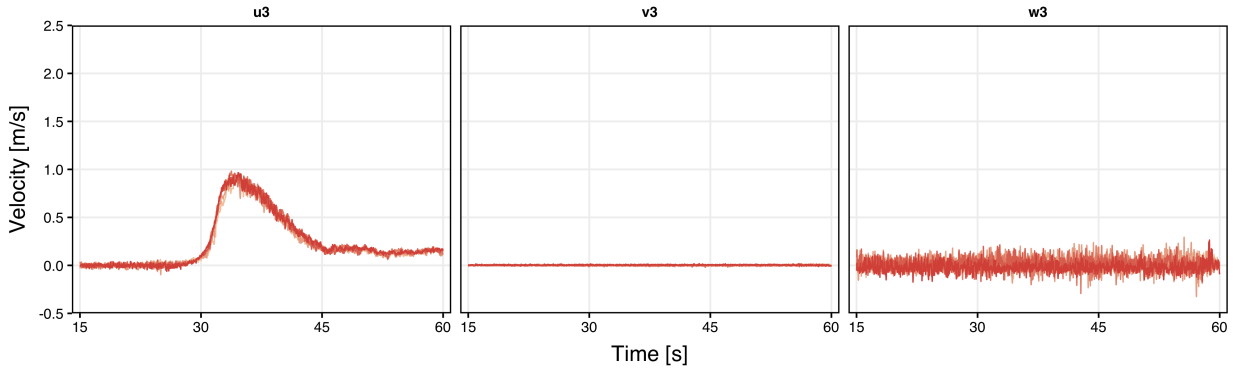


(a) ADV3; 0.234 m below SWL

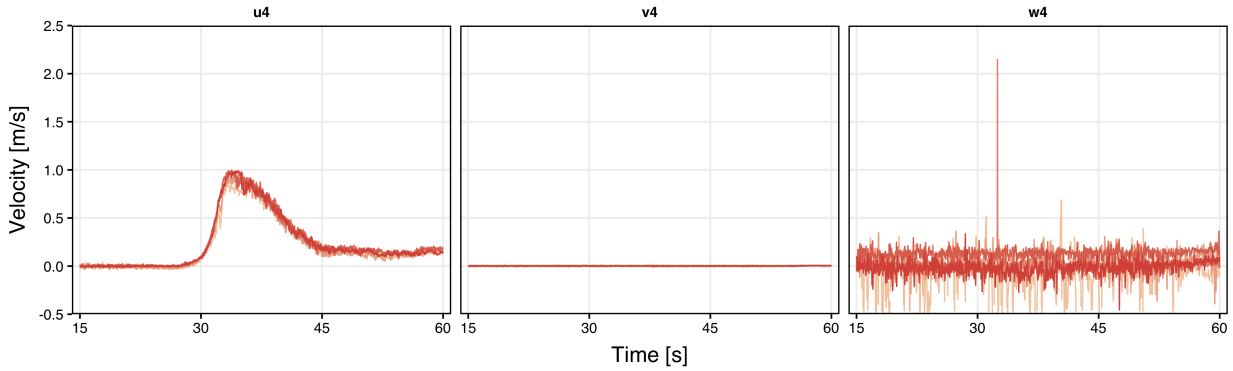


(b) ADV4; 0.234 m below SWL

Figure 3.6: ADVs 3 and 4 for "Pre-Stiffening" unbroken wave trials; sampled at 120 Hz without filtering. Color gradient shows different trials.

ADVs 5 and 6 are the next velocimeters in the direction of wave propagation. ADV5 is located to the east side of the structure and at a similar elevation to ADVs 3 and 4. ADV6 is at a similar elevation but is located underneath the test structure at an approximate streamwise centerline. The velocity time histories for ADVs 5 and 6 are shown in Figure 3.7.

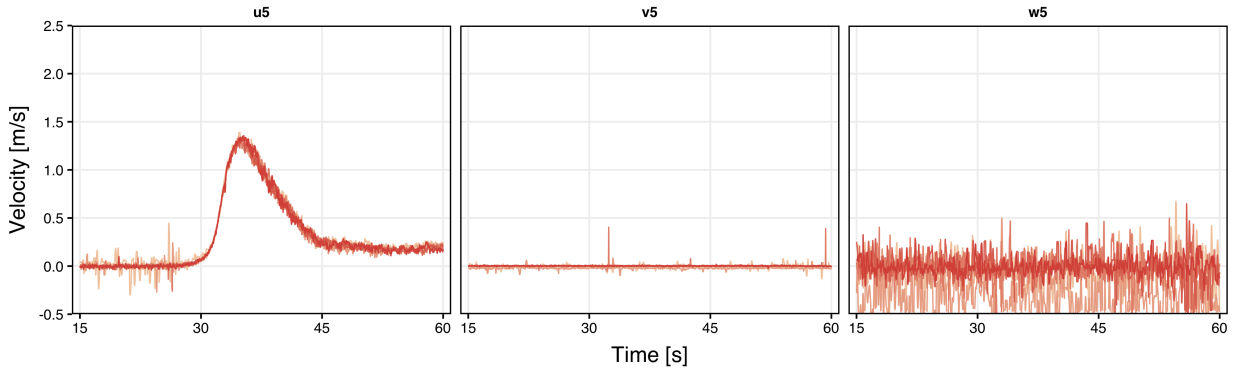


(a) ADV5; 0.241 m below SWL

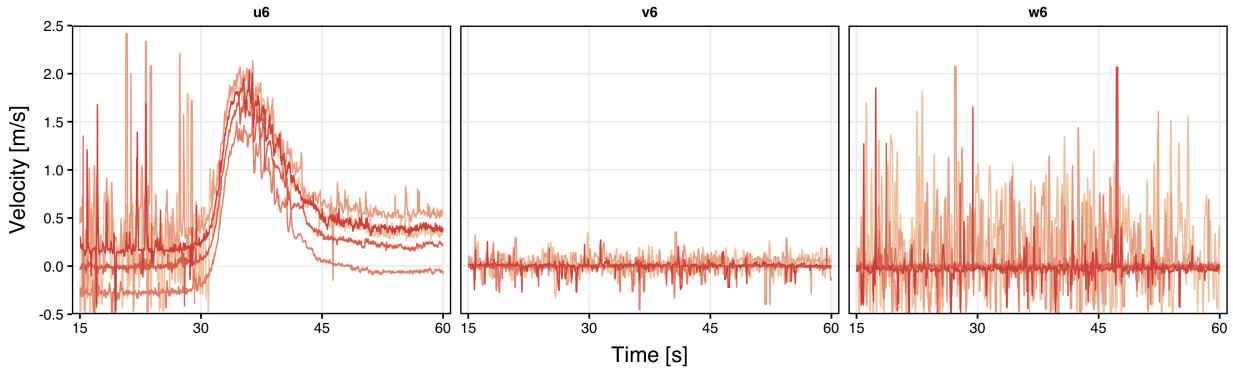


(b) ADV6; 0.204 m below SWL

Figure 3.7: ADVs 5 and 6 for "Pre-Stiffening" unbroken wave trials; sampled at 120 Hz without filtering. Color gradient shows different trials.

The overall highest recorded streamwise velocity is recorded by ADV6 and has a median

peak value of 2.026 m/s. We note the noise and instrumentation offset within ADV6; however, this increase in velocity is likely due to constriction as the wave passes underneath the test structure. Given a small pathway for the flow to move, the velocity increased. While vertical velocity measurements are noisy, any fluctuation is likely due to flow separation and eddying around the legs of the structure (through which the flow must pass in this area).

The second-highest recorded streamwise velocity was recorded by ADV5 and has a median peak value of 1.343 m/s. This increase in velocity after the primary face has been contacted by the wave is likely due to channel effects, as it is directly to the side of the structures in a region of flow constriction (reference Winter et al. (2020)).

ADV7 is located at the centerline of the flume and downstream of the structure by approximately 2.5 m and is shown in Figure 3.8. Behind the structure, a high peak streamwise velocity is observed. There is a high-frequency signal in the $z$-direction, which may indicate turbulence as the wave passes around and underneath the structure.

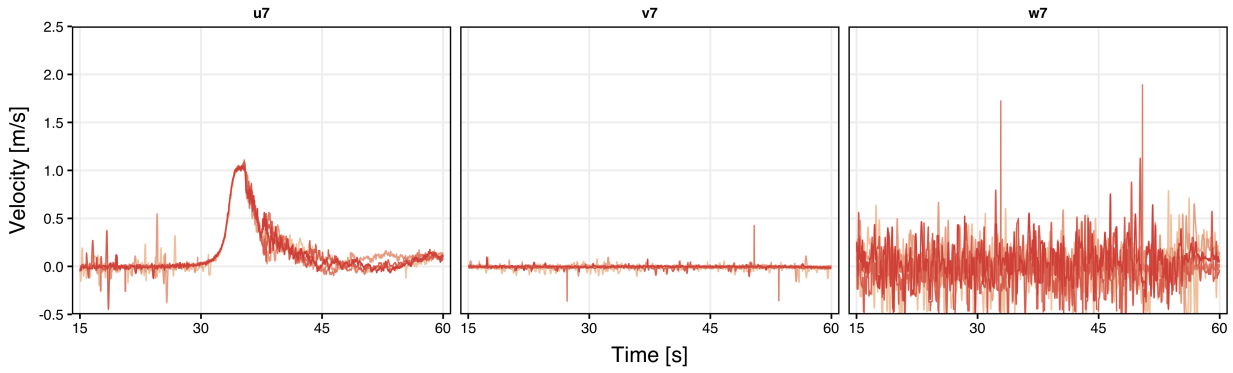


Figure 3.8: ADV7 for "Pre-Stiffening" unbroken wave trials; 0.232 m below SWL, sampled at 120 Hz without filtering. Color gradient shows different trials.

In both the transverse and vertical directions ($v$ and $w$), the velocities are small compared to the streamwise velocity ($u$). This is due to the high degree of symmetry and directionality present in the wave. The initial peak in all cases occurs at approximately 35 to 40 seconds,

which represents the initial wave passing. A negative velocity (toward the wavemaker) is observed at approximately 70 seconds, which represents the reflection of the initial wave back toward the wavemaker.

For all ADVs, there is consistency between trials. This is a critical finding, as it confirms the repeatability and predictability of the unbroken wave hydrodynamics. In general, the components of transverse or vertical velocity are small compared to the streamwise velocity. There is no intentional modification via macro-scale roughness or wavemaker properties to this flow in the shown trials or any trials later discussed, so we assume that the velocities as shown are applicable to all trials using the unbroken wave.

## *3.4 Structural Reactions*

The primary purpose of trials without debris is to understand the force on the test structure in the absence of debris, allowing the isolation of the effects of debris impacts and damming. This provides an important baseline for further analysis after the introduction of debris. As discussed in Chapter 2, there are eight load cells: two in-line load cells to measure transverse loads on the test structure, two in-line load cells to measure streamwise loads, and four pancake load cells to measure vertical loads. Since the primary direction of flow (and thus, debris motion) is streamwise, the two streamwise load cells are particularly important. However, the discussion herein includes both the transverse and vertical reactions as well.

The test structure was designed using frictionless bearings and rigid connections to load cells. After several iterations, the described load cell configuration including internal load path transfer rods provided a stiffer system. Note that the sampling was performed at 1200 Hz on the "post-stiffening" unbroken wave trials.

### *3.4.1 Streamwise Loads*

Streamwise in-line load cells were attached to the back face of the structure and were intended to measure the reactions to forces imparted by the wave and debris impact on the front of the structure. While some transfer of loads is anticipated throughout the structure, the

data acquired from their readings allow a proxy for applied loading via reaction forces. The following data and discussion come from trials conducted "post-stiffening" of the test structure.

For the six trials conducted, the following two plots in Figure 3.9 represent the time history during the unbroken wave. The streamwise load cell data is consistent among the six trials. We observe the maximum load occurs at approximately 33.5 seconds, which is consistent with the arrival of the unbroken wave. The peak values are taken for each trial, and then the medians and interquartile ranges are reported, as shown in Table 3.1.

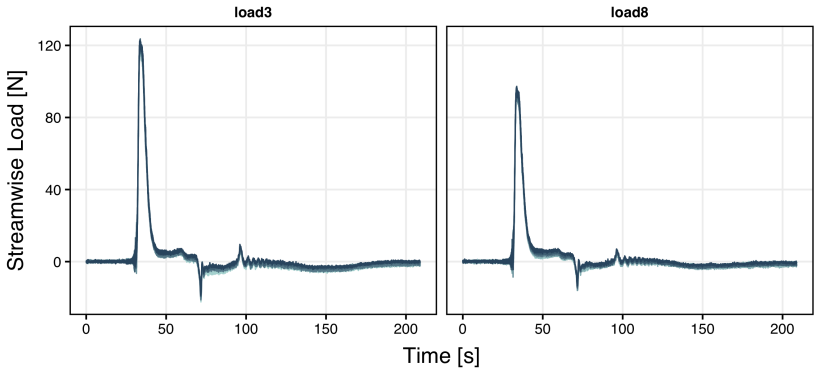


Figure 3.9: Load cells 3 and 8 (eastmost and westmost streamwise load cells, respectively); 1200 Hz sampling frequency between 25 and 50 seconds (20 Hz otherwise), full time history, individual trials are shown as gradient.

Table 3.1: Streamwise load cells 3, 8, and summed median peak values and range (% "+/-")

| Name | Median Peak Load [N] | IQR [N] | Median Time at Trial Peak |
|---|---|---|---|
| load3 | 120.9 | 3.1 | 33.68 |
| load8 | 94.4 | 3.0 | 33.54 |
| Streamwise Total | 214.4 | 6.4 | 33.57 |

We observe that load cell 3 (eastmost) reads approximately 25% higher during symmetric

loading. This is taken to be a result of minor structural asymmetry. Given experimental tolerance, the measurements are still able to provide a consistent baseline during the unbroken wave. We see consistency between the time at peak for each trial, represented by the median peak value time per trial.

A more useful value for further understanding streamwise loads is the total streamwise load, taken by summing the data from both streamwise load cells at each instance for each trial. Figure 3.10 shows the total streamwise loading for the full time history, as well as for the portion of time around the wave event (25 to 50 seconds). The total streamwise load cell data is shown in Table 3.1.

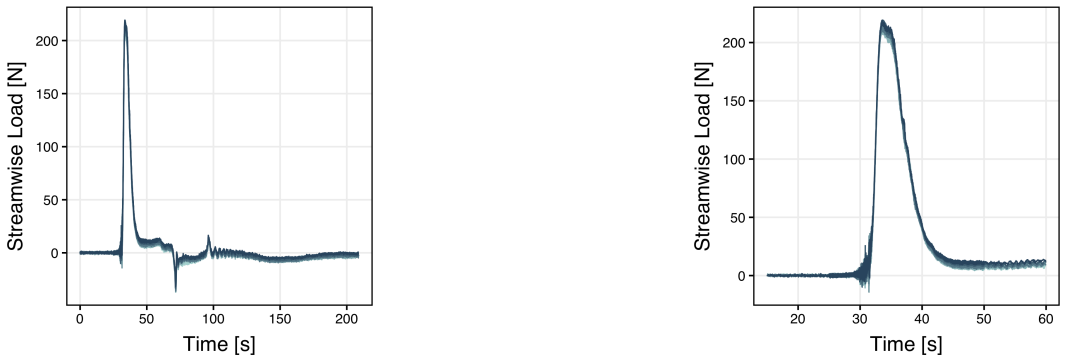


(a) Total streamwise load cell values full time history.

(b) Total streamwise load cell values time history during contact with test structure.

Figure 3.10: Total streamwise load cells (above) are the addition between load cells 3 and 8 per time step; 1200 Hz sampling frequency between 25 and 50 seconds (20 Hz otherwise), individual trials are shown as gradient.

It can be observed that the results from the total streamwise load cell data are consistent across trials throughout the entire time history, as well as the median peak value time per trial for both total and individual streamwise load cells. Variation in loading across trials and between tests in streamwise loading can thus be taken to be a result of debris field

interaction in the following chapters.

### *3.4.2 Transverse Loads*

Transverse loads were measured by two in-line load cells attached to the support frame at the top of the structure. They were both attached to the easternmost side of the box (in the negative $y$-direction from the flume streamwise centerline), so their values cannot be assumed to be symmetrical; thus, they are not added as in the case of streamwise load cells, but are taken to work independently. Figure 3.11 shows the transverse load cell time histories. Load cell 1 is located upstream and load cell 2 is located downstream of the center of the test structure. We observe similar consistency between trials for each load cell. The median peak forces, interquartile range, and median time of the peak value are taken for each load cell and are reported in the Table 3.2.

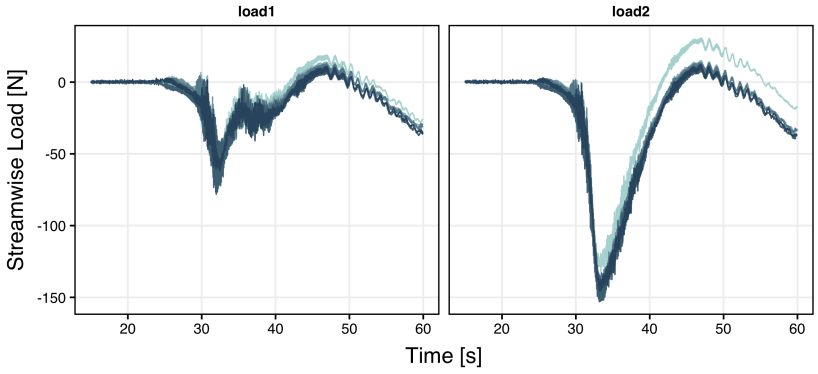


Figure 3.11: Load cells 1 and 2 (upstream and downstream transverse load cells, respectively); 1200 Hz sampling frequency, full time history, individual trials are shown as gradient.

There is a difference in maximum reaction force between the upstream (1) and downstream (2) load cells, and an offset of these peak values of approximately one second. A negative force values correspond to tension in the in-line load cells (i.e., reaction forces resisting test structure motion toward the west side of the flume). This offset and large tensile

Table 3.2: Transverse load median peak values and interquartile range and median peak value time per trial

| Name | Median Peak Load [N] | IQR [N] | Median Time at Trial Peak [s] |
|---|---|---|---|
| load1 | -62.2 | 1.4 | 32.11 |
| load2 | -146.1 | 2.73 | 33.34 |

value is likely due to the restraint system of the test structure, as the only transverse attachments are situated on the east side of the structure. Additionally, although the flow is symmetrical, there is likely some eddying and flow separation occurring as the wave passes the structure, creating turbulent transverse forces. We observe that the shown reaction forces are repeatable in this system, and thus can be considered a baseline against trials with debris.

Figure 3.12 shows load cells 1 and 2 overlaid, which shows the disparity between peak tensile forces in the first peak for a selected trial. Subsequent tensile peaks match more closely, which indicates that the system is not necessarily resisting rotation about the $z$-axis, but instead is resisting transverse forcing.

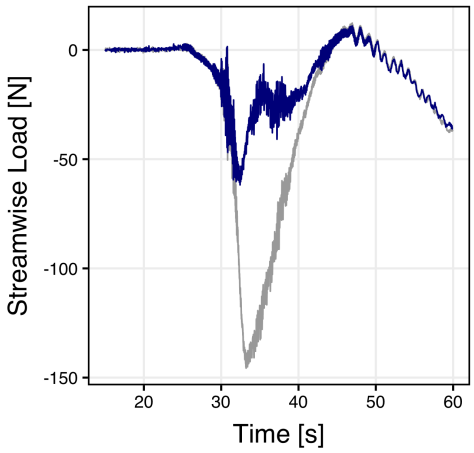


Figure 3.12: load cells 1 (BLUE) and 2 (GREY) for one selected trial (upstream and downstream transverse load cells, respectively); 1200 Hz sampling frequency, full time history.

### *3.4.3 Vertical Reactions*

Four pancake load cells were positioned on the top face of the test structure near its corners. Designed to measure vertical reactions due to the wave and debris, they provide a proxy of imparted uplift forces from the wave itself and from the debris. They also serve as the vertical points of attachment for the structure.

Figure 3.13 shows time histories for the load cells, oriented with wave propagation direction to the right. Load cells 4 and 5 are the front corners of the structure, whereas load cells 6 and 7 are the back corners of the structure. Again, consistency throughout the entire time history is observed. The dominant maximum forces are uplift (compressive): the test structure supports are resisting vertical forces imparted by the passing wave. The initial wave impact shows significantly higher uplift forces in the back two load cells. Table 3.3 gives peak forces in each load cell and the median time at peak value per trial.

The time of maximum load is consistent between the two front load cells and, separately, the two back load cells. Front load cells have consistently lower and earlier peak forces. This

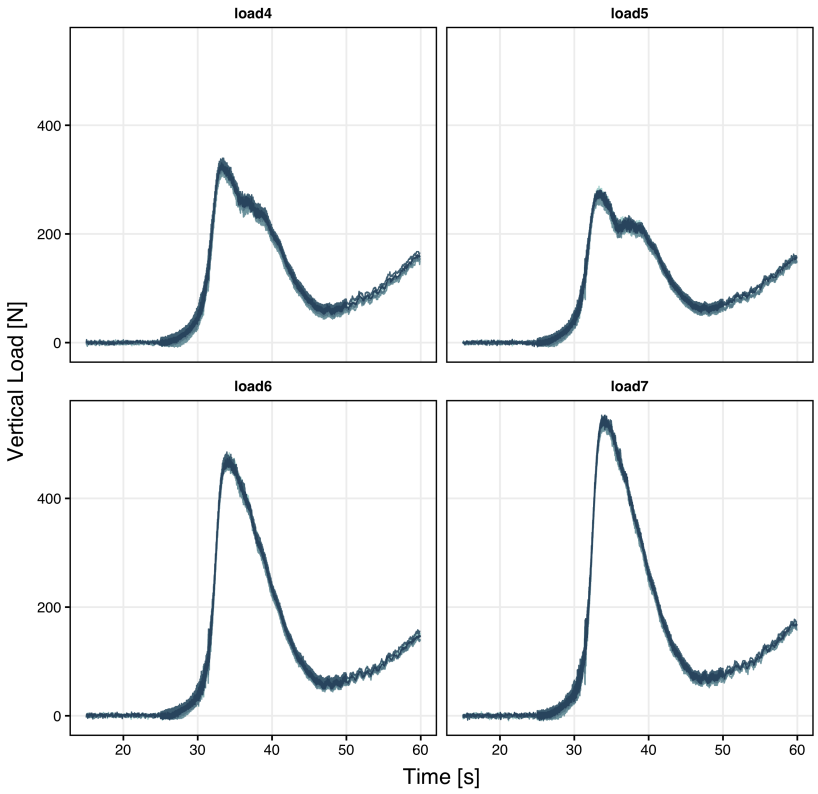


Figure 3.13: Load cells 4, 5, 6, and 7 (southeast, southwest, northeast, and northwest vertical load cells, respectively); 1200 Hz sampling frequency, wave only time history, individual trials are shown as gradient.

Table 3.3: Vertical load median peak values, interquartile range, and median peak value time per trial

| Name | Median Peak Load [N] | IQR [N] | Median Time at Trial Peak [s] |
|---|---|---|---|
| load4 | 328.5 | 3.0 | 33.28 |
| load5 | 278.9 | 8.3 | 33.46 |
| load6 | 473.2 | 10.3 | 34.16 |
| load7 | 549.3 | 6.0 | 34.06 |

is likely due to increased flow channeling underneath the structure at the upstream portion and the fact that wave contacts the back of the structure at a later time.

Figure 3.14 shows overlay and temporal interplay between the load cells for one selected trial. There is consistency between the time histories as shown within the selected trial. However, the highest peaks are later and from the downstream vertical load cells. Smaller, later peaks are seen at similar times for all load cells, and represent reflected waves after the primary wave event.

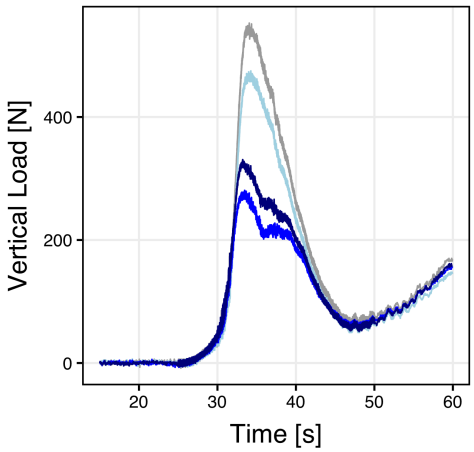


Figure 3.14: Load cells 4 (dark blue), 5 (blue), 6 (light blue), and 7 (grey) (southeast, southwest, northeast, and northwest vertical load cells, respectively) for one selected trial; 1200 Hz sampling frequency, full time history.

# Chapter 4

# STREAMWISE REACTIONS DUE TO REGULAR DEBRIS CONFIGURATIONS

This chapter discusses 10 tests conducted with the following conditions: 1) unbroken wave, 2) wooden (lift) frame, 3) standard-sized debris, and 4) regular (tightly-packed) configurations. This set of tests is termed herein referred to as "regular" tests.

The hydrodynamics of the unbroken wave yields a streamwise load profile that is predictable and repeatable (as discussed in Chapter 3). The wooden frame was employed as it is able to hold a regular configuration steady until the arrival of the wave. Debris size was not modified and is per Figure 2.8. This section manipulates the following variables:

1. number of debris
2. individual debris orientation and configuration

The general method of data analysis is discussed during the analysis of single debris tests. This method will be extended throughout this chapter and Chapters 5 and 6.

This set of 10 tests was conducted with 10 trials per test. All configurations were tightly-packed (i.e., the initial debris field had a 100% surface area density). All configurations were configured symmetrically along the center axis of the flume in the direction of flow ($y = 0$), with the furthest downstream face of debris situated 2m from the front face of the test structure.

Configurations with one, 8, 16, and 24 debris were tested. For all debris quantities, the configurations were either oriented with the individual longest debris axes parallel to the direction of flow (i.e., *longitudinal*) or perpendicular to the direction of flow (i.e., *transverse*). Using the wooden/lift frame allowed for the tightly-packed, specific configurations to be

maintained on the surface of the free surface before the arrival of the wave. Figure 4.1 shows all of the configurations tested in this test phase.

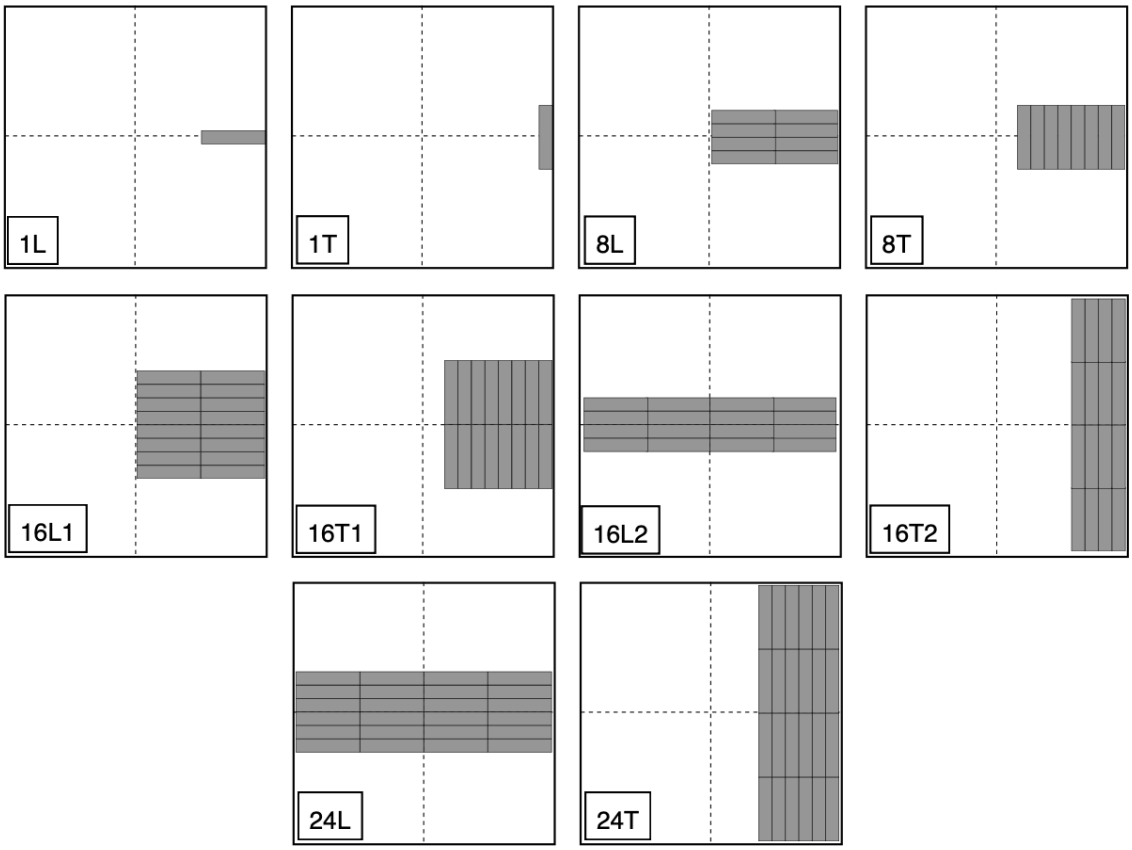


Figure 4.1: 10 configurations tested with an unbroken wave, wooden (lift) frame, standard-sized debris, with regular (tightly-packed) configurations. The direction of wave flow is from left to right, with the test structure located 2m from the rightmost outer edge of each configuration.

Data discussed within this section is raw and sampled at 1200 Hz to capture high-frequency impact events. For ease of data use, the data is downsampled to 20 Hz before the wave event and after the wave event (from 25 to 50 seconds experiment time). During the time range discussed within this section (30-45 seconds), the full sampling history is used

in analysis.

### *4.1 General Methodology & Single Debris: Longitudinal & Transverse*

Two tests were conducted with a single, full-sized debris with an unbroken wave. Understanding the loading caused by a singular debris is imperative to compare the loading due to more complex debris fields. A singular debris was tested both longitudinally and transverse to the direction of flow.

The total streamwise load is the summation of load cell 3 and load cell 8, both in-line load cells located behind the test structure and intended to measure force in the direction of flow. Figure 4.2 shows load cells 3 and 8, as well as their sum total for a single debris oriented longitudinally and subjected to the unbroken wave.

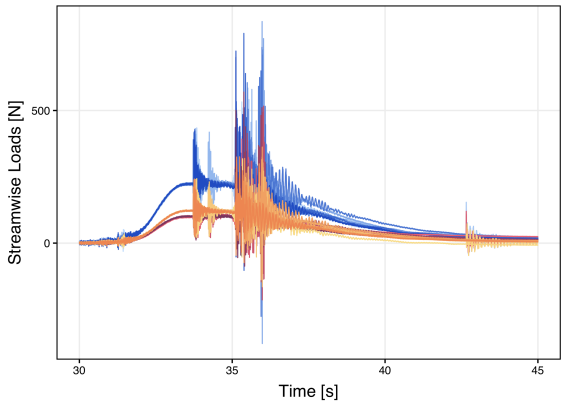


Figure 4.2: Load cell 3 (indicated in ORANGE gradient), load cell 8 (indicated in PURPLE gradient), and total streamwise load (indicated in BLUE gradient) for each of the 10 trials conducted with an unbroken wave and single debris oriented longitudinally to the direction of flow.

Generally observable within time histories in this scope are negative forces (indicating loading in the direction opposite the flow and/or tensile strains within in-line load cells). This is a product of high-frequency excitation and vibration within the load cells and test

structure due to debris impacts that tapers off after an initial impact. While a high-frequency filter could be used to attempt to remove some experimental noise, the peak values are substantially reduced through this process, and thus this process is not used in analysis; reference Appendix A for further discussion.

In Figure 4.2 for this specific case, we can observe that both load cell 3 and load cell 8 are approximately equal in value and sum to the full value, implying the loads were approximately symmetric. Additionally, all 10 trials tend to have similar patterns and peak load values. The initial impact was largely head-on from the smallest face of the debris and struck the test structure at approximately the center. The photograph shown in Figure 4.3 shows a typical strike.

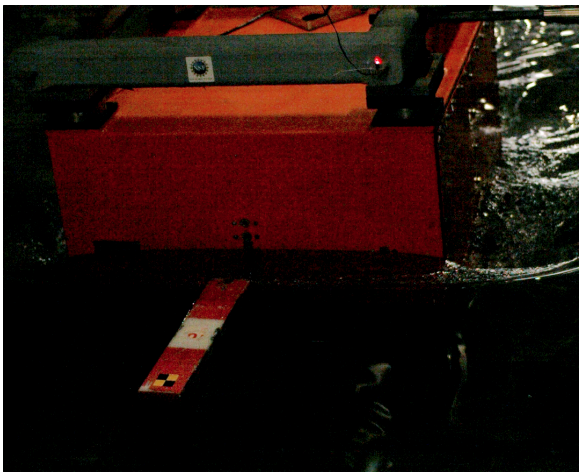

Figure 4.3: Selected trial captured by high-speed camera prior to impact for single debris oriented longitudinally to the direction of flow.

The transverse orientation of the single debris shows a lower peak value, but has similar symmetry between load cells 3 and 8. All 10 trials show consistency in each load cell, shown in Figure 4.4. The single piece of transversely oriented debris typically struck the test structure along its second-largest face. Figure 4.5 shows a typical transverse strike.

While the mass and wave velocity are consistent between the two tests, the transverse

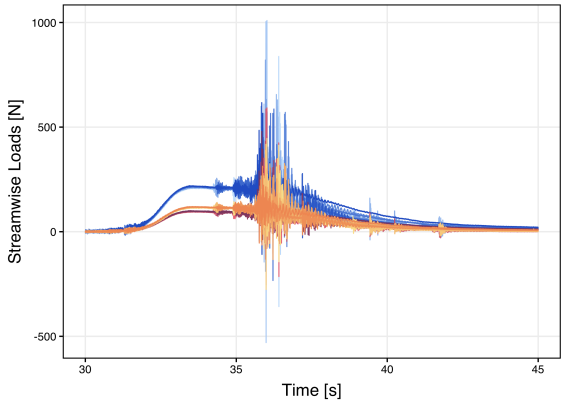


Figure 4.4: Load cell 3 (indicated in ORANGE gradient), load cell 8 (indicated in PURPLE gradient), and total streamwise load (indicated in BLUE gradient) for each of the 10 trials conducted with an unbroken wave and single debris oriented transversely to the direction of flow.

Figure 4.5: Selected trial captured by high-speed camera prior to impact for single debris oriented transversely to the direction of flow.

debris is oriented with the second broadest face in the direction of flow. The longitudinal orientation instead is defined with the debris' narrowest face oriented in the direction of flow,

lending to lower drag and thus more hydrodynamic efficiency. Conversely, the transverse debris slows slightly just before impact and begins to roll over its longest axis before contacting the test structure.

We can compare the longitudinal and transverse single debris orientations to the unbroken wave loading. Figure 4.6 shows all three tests with all trials.

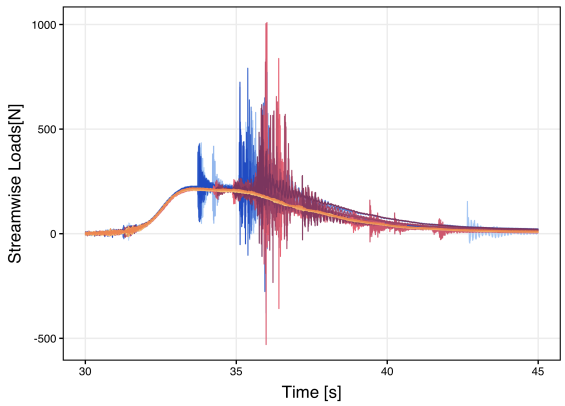


Figure 4.6: Unbroken Wave without debris total streamwise load (indicated in ORANGE gradient), Single Transverse Debris full streamwise load (indicated in PURPLE gradient), and Single Longitudinal Debris total streamwise load (indicated in BLUE gradient) for all respective trials conducted.

One can observe again that the unbroken wave load time history is consistent between trials. All three time histories are similar until high-frequency signals are observed at around 33.5 seconds in both debris tests. In both debris signals, we also see a second impact with higher magnitude occur after 35 seconds. The first impact is higher in the longitudinal configuration than in the transverse, indicating that the first contact with the box is a higher force than that of the transverse orientation.

Until the first impact, the low-frequency signal of the wave-induced loading is very similar to trials in which only the wave without debris is tested. This consistency implies that variations in the load profile are due to the streamwise impact of debris.

The nature of the loading due to debris shows the pattern discussed above, which indicates a first peak before 35 seconds, and a second peak after 35 seconds. After these peaks, a higher, low-frequency signal is observed in all trials from the longitudinal and transverse debris case, until the signal returns to approximately zero after 40 seconds. In Shekhar et al. (2020), this effect is termed "damming" and is quantified after higher frequency signals are removed from the debris trials via inverse Fast Fourier Transform. We introduce this general form observed in streamwise loads first with single debris, then extend to higher quantities of debris with various configurations.

### *4.1.1 Peak Loads*

To quantify and discuss the first and second impacts observed in single debris trials, we separate the impacts based on observation by separating experiment time as either less than 34.5 seconds or greater than 34.5 seconds (corresponding to the first and second peak, respectively). The absolute maximum streamwise load value is also calculated. As previously discussed, the data in this time region is neither filtered nor downsampled (see Appendix A).

Absolute maximum, first, and second peak values are found for each trial. Due to the nondeterministic nature of debris impacts, there is variance in peak value between trials. To understand the statistical significance of each peak, we investigate the distribution of the peaks between trials for each experiment. In this case, we consider streamwise loads due to single debris oriented either longitudinally or transverse, and the unbroken wave-only streamwise loads.

For all 10 trials, we can begin to understand the peak values via quantile-quantile plots, or QQ-plots. We suspect the maximum values in each trial are distributed normally, and QQ-plots offer a visual means to understand the normality of a distribution. A QQ-plot shows the quantiles of the standard normal distribution on the $x$-axis (mean at 0 and standard deviation of 1) and the sample's quantiles on the $y$-axis. A line is drawn between both the theoretical and the sample first and third quantiles. A distribution that is approximately

normal will appear linear and will have the majority of values within the -1 and 1 standard deviations of the mean. Figure 4.7 shows QQ-plots for the unbroken wave-only test with six trials, and all 10 trials for both the single longitudinal debris and single transverse debris.

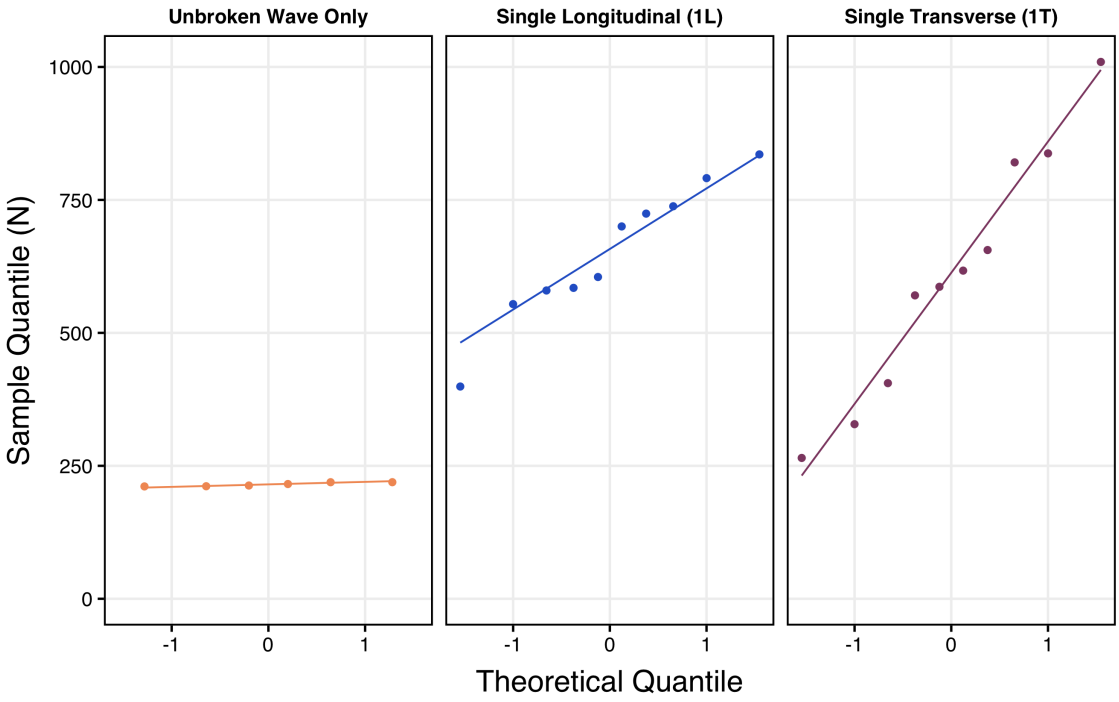


Figure 4.7: QQ-plots for peak streamwise loads due to unbroken wave only, single longitudinal debris, and single transverse debris trials.

By visual inspection, we observe a linear correlation in all three plots. The wave-only plot shows consistent peak values between all six trials, as discussed in-depth in Chapter 3.

Single Longitudinal (1L) and Single Transverse (1T) are both linear, but show a range of maximum peak values per trial. We can assume they are similar to a normal distribution. To quantify the normality of these distributions, we conduct a statistical evaluation of normality called the Shapiro-Wilk test (Ghasemi and Zahediasl (2012)). The Shapiro-Wilk test states a null hypothesis that the sample distribution is normal. We assign a p-value $p < 0.05$ in

order to reject the null hypothesis. For each of the experiments, p-values are shown in Table 4.1.

Table 4.1: P-values from Shapiro-Wilk Test for Normality for Maximum Peak Streamwise Loads per Trial

| Experiment Name | P-Value |
|---|---|
| Unbroken Wave Only | 0.18 |
| Single Longitudinal (1L) | 0.75 |
| Single Transverse (1T) | 0.86 |

Each p-value is greater than the requisite to reject the null hypothesis that the distribution is normal. Thus, we assume via visual inspection (QQ-plots) and the Shapiro-Wilk test that these distributions are approximately normal. We then characterize the absolute maximum peak value per test as the median trial value (assuming that the median is approximately equal to the mean in approximately normal distributions). This median peak load is calculated by taking the maximum value of each trial, then taking the median value of the maximum values. As a measure of spread, we characterize the range of values and normalize them by the mean as a percentage above and below the median peak values.

For all three tests, the absolute maximum peak value and measures of spread are shown in Table 4.2. The table also includes the absolute maximum peak for the trial with the median absolute maximum peak value which is found by taking the time at the absolute maximum for each trial, then taking the median.

We observe that the single longitudinal debris has the highest median total streamwise force throughout the entirety of the experiment time. We also observe that the peak values when debris are present, unlike during the wave, occur after 34.5 seconds, whereas the median peak time is only 33.5 seconds for the wave only. Additionally, the variability of observed values is high for tests with debris. The transverse debris has higher variability than the longitudinal debris. This is due to the nondeterministic nature of the introduction of debris

Table 4.2: Total streamwise loads median peak values, interquartile range, and median time of absolute peak value per trial

| Name | Median Peak Load [N] | IQR [N] | Median Time at Trial Peak [s] |
|---|---|---|---|
| Unbroken Wave Only | 214.4 | 6.4 | 33.57 |
| Single Longitudinal (1L) | 652.6 | 153.7 | 35.46 |
| Single Transverse (1T) | 601.8 | 332.6 | 36.00 |

to the flow, but the comparison of median values is non-sensitive to extreme values between individual trials, and thus will be employed throughout this discussion.

To fully understand the trends throughout the trial, we investigate the observed first peak and second peak separately. We can conduct a similar analysis to determine if the first and second peaks between trials are distributed normally. By filtering for peaks occurring before 34.5 seconds, we observe the following from the debris tests as shown in Figure 4.8. One can observe that both the longitudinal and transverse trials are approximately linear, with an outlier observed in the longitudinal trials. The results of the Shapiro-Wilk test are shown in Table 4.3.

Table 4.3: P-values from Shapiro-Wilk Test for Normality for First Peak Streamwise Loads per Trial

| Experiment Name | P-Value |
|---|---|
| Single Longitudinal (1L) | 0.0017 |
| Single Transverse (1T) | 0.10 |

Although the null hypothesis (i.e., that the distribution is normal) can be rejected in the case of the single longitudinal trial since $p < 0.05$, we can visually inspect via the QQ-plot that this is due to a single low outlier. Using the median enables an understanding of the central tendency of the first peak value. Table 4.4 shows both median values, interquartile range, and median time of the first peak per trial. We observe that both experiments' first

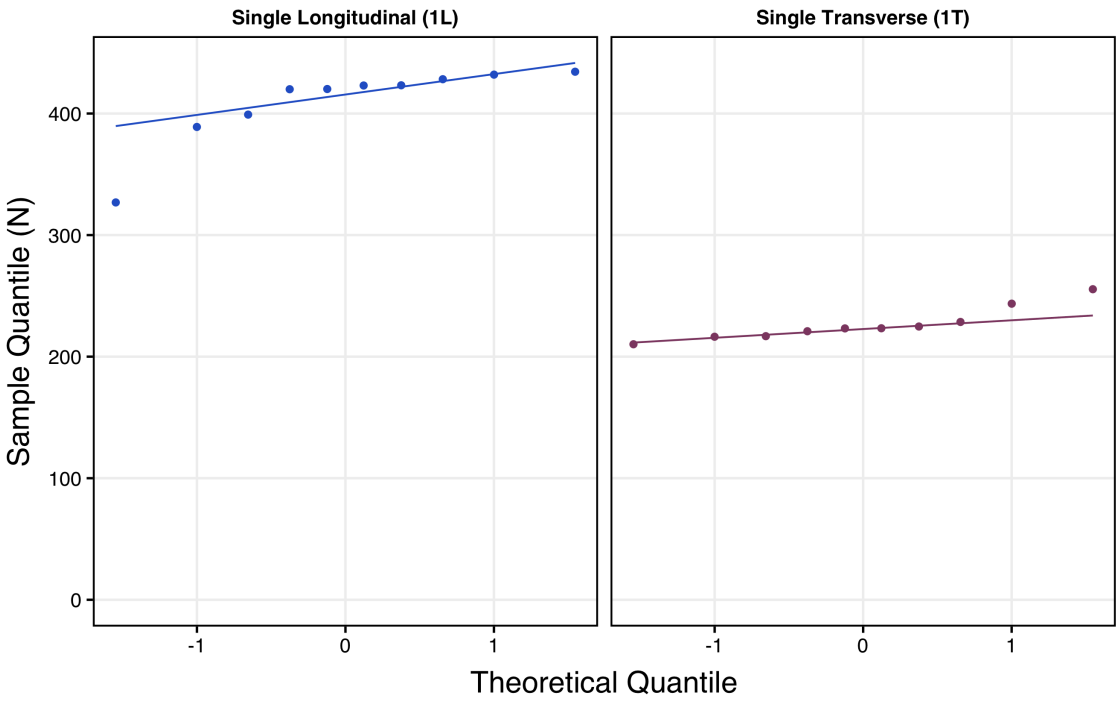


Figure 4.8: QQ-plots for the FIRST peak streamwise loads due to single longitudinal debris and single transverse debris trials.

peak values are lower than their absolute maximum peak, but the single longitudinal first peak value is greater than the single transverse first peak value. This indicates the initial impact with the test structure is greater when the debris is oriented longitudinally in the direction of flow.

Table 4.4: Total streamwise loads median FIRST peak values, interquartile range, and median time of first peak value per trial

| Name | Median Peak Load [N] | IQR [N] | Median Time at First Trial Peak [s] |
|---|---|---|---|
| Single Longitudinal (1L) | 421.6 | 22.7 | 33.78 |
| Single Transverse (1T) | 223.3 | 9.7 | 34.39 |

A similar analysis is performed with the second peak, which occurs after 34.5 seconds. The QQ-plot and Shapiro-Wilk test results are as follows in Figure 4.9 and Table 4.5. We cannot reject the null that the second peak distributions are normally distributed, and that can be further corroborated via visual inspection of QQ-plots. Table 4.6 explains the second peak distributions.

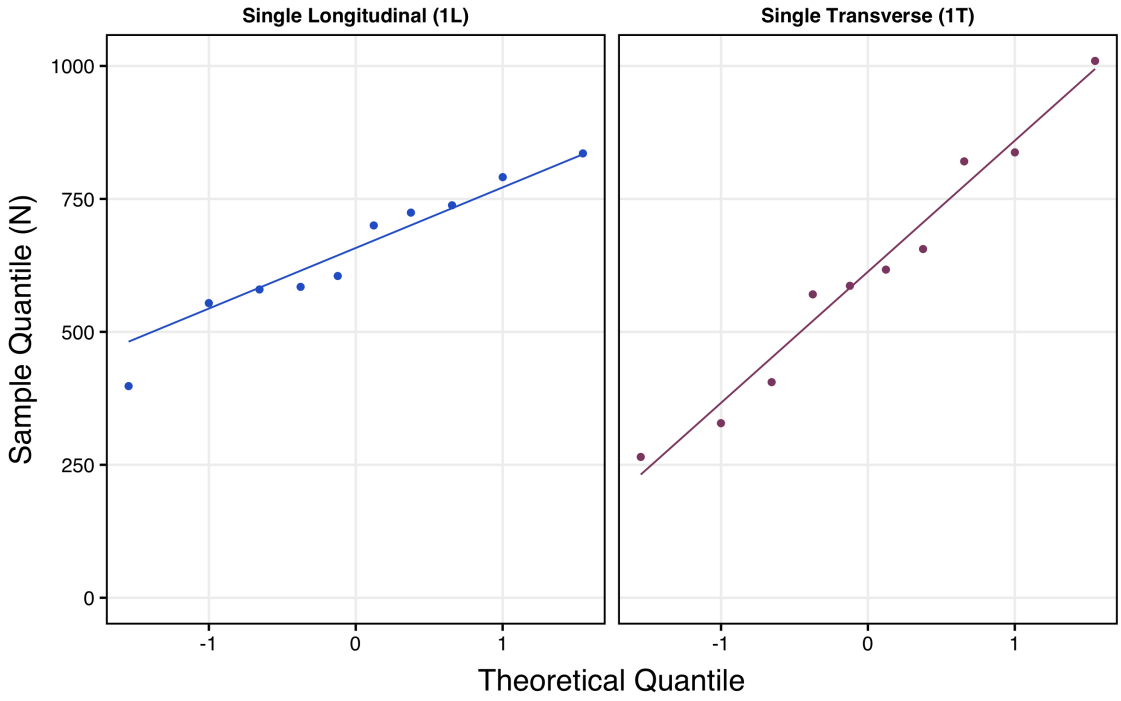


Figure 4.9: QQ-plots for SECOND peak streamwise loads due to unbroken wave only, single longitudinal debris, and single transverse debris trials.

In the case of the second peak, the medians are close in value, but the transverse trial has a larger spread of values (including a higher upper bound). In both cases, the second peak value is higher than the first peak value.

The process for quantifying absolute maximum, first peak, and second peak values will be extended to experiments with higher numbers of debris and different initial configurations

Table 4.5: P-values from Shapiro-Wilk Test for Normality for First Peak Streamwise Loads per Trial

| Experiment Name | P-Value |
|---|---|
| Single Longitudinal (1L) | 0.75 |
| Single Transverse (1T) | 0.86 |

Table 4.6: Total streamwise loads median SECOND peak values, interquartile range, and median time of first peak value per trial

| Name | Median Peak Load [N] | IQR [N] | Median Time at Second Trial Peak [s] |
|---|---|---|---|
| Single Longitudinal (1L) | 652.6 | 153.6 | 35.48 |
| Single Transverse (1T) | 601.8 | 332.6 | 36.00 |

in later sections.

### *4.1.2 Comparison to In-Air Elastic Debris Collisions*

Some existing discussions of analogous debris impact scenarios (including in ASCE 7) assume momentum transfer based on the conservation of momentum (Shekhar et al. (2020)). This provides an idealized impact force for a single debris impact in air to be quantified as a single degree-of-freedom elastic collision between a solid block and rigid boundary without energy loss (ref. B, and can be expressed as:

$$F_{calc} = v\sqrt{mk}$$

where

$$k = EA/L$$

and $m$ is the debris mass, $E$ is the modulus of elasticity of an ideal linear elastic material, and $A$ is the cross-sectional area of the debris (assuming a simple, single degree-of-freedom system). Per Shekhar, the approximate maximum velocity of a single piece of debris driven

by the unbroken wave regardless of orientation is $v = 1.3m/s$. The stiffness $k$ is dependent also on the length of the debris $L$. Given this simple calculation for a debris oriented longitudinally, $F_{calc} = 5950N$.

This value far exceeds reaction forces measured via the test structure and attached load cells and does not account for gradual slowing due to drag or other complex fluid-debris interactions. Table 4.2 summarizes maximum measured reactions, which are an order of magnitude less than the calculated force. This is an important finding, as it indicates that the existing understanding of methodology for understanding debris impacts in inundation-type flows is likely highly conservative.

Note: velocity measurements for specific experiments are observable via video data analysis outside of the scope of this text, but will provide further insight into the motion of debris versus an idealized elastic condition. Measurements within the system are reaction forces to an applied load, and are discussed as a means to compare relative forces between different configurations.

### *4.1.3 Damming Loads*

Observing the time histories in Figure 4.6 (see above) shows that low-frequency streamwise load signal due to the unbroken wave only appears to be lesser than in cases where there is debris present from approximately 37.5 seconds to 40 seconds. Shekhar et al. (2020) refers to this increase in loading as the effect due to damming of debris, particularly on the legs of the test structure.

In Shekhar et al. (2020), damming forces are discussed in terms of the hydrodynamic parameter, which is defined as $\frac{1}{2}A\rho v^2$. $\rho = 1000kg/m^3$ is the density of water, $A$ is the area of the first impacting face depending on orientation, and $v$ is the observed flow velocity.

As mentioned, the loads measured by load cells attached to the test structure are reaction forces, and the measurements provide a means of comparison across configurations. Therefore, the following method is used to understand these relative forces.

To understand damming, the high-frequency impact signals are filtered out. This is per-

formed via Fast Fourier Transform to transform the time history of impacts into the frequency domain, and then remove frequencies over a certain threshold. Fast Fourier Transform is an algorithm that performs a discrete Fourier Transform: this decomposes a signal in a time-domain to components of different frequencies in a frequency domain. For the purposes of single debris tests, the following process is employed.

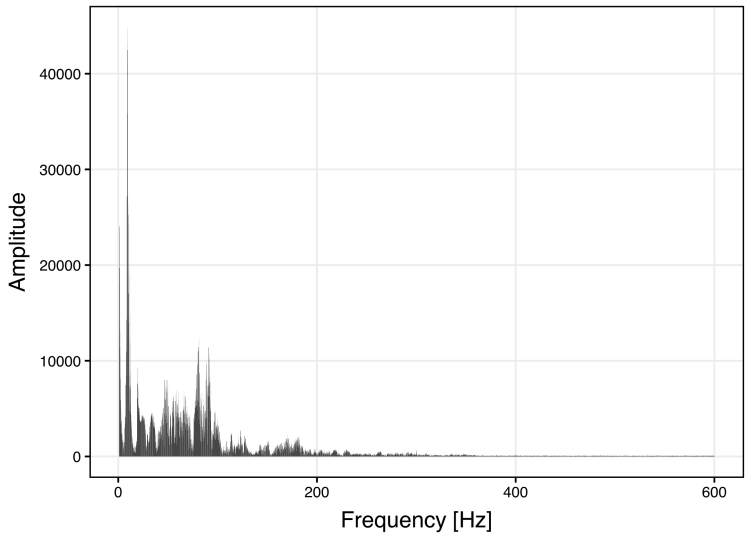


Figure 4.10: Frequency Domain of Single Longitudinal debris (1L) for one selected trial.

Since Fast Fourier Transform are resolved at a maximum frequency (called the Nyquist Frequency) of 1/2 the sampling rate (1200 Hz), the frequency domain extends only to 600 Hz. However, we see that the relative amplitude above 200 Hz is negligible compared to lower frequencies. Following the methods used in Shekhar et al. (2020), one can apply the following low pass filter to gradually bring frequencies above 4 Hz to 0. The zero-ing function is a cumulative density function and is shown in Figure 4.11 with mean at 4 Hz and standard deviation of 1 Hz.

Applying the coefficients as shown leads to a modified frequency domain, which can be reconstructed to the time domain using an inverse Fast Fourier Transform. The reconstructed

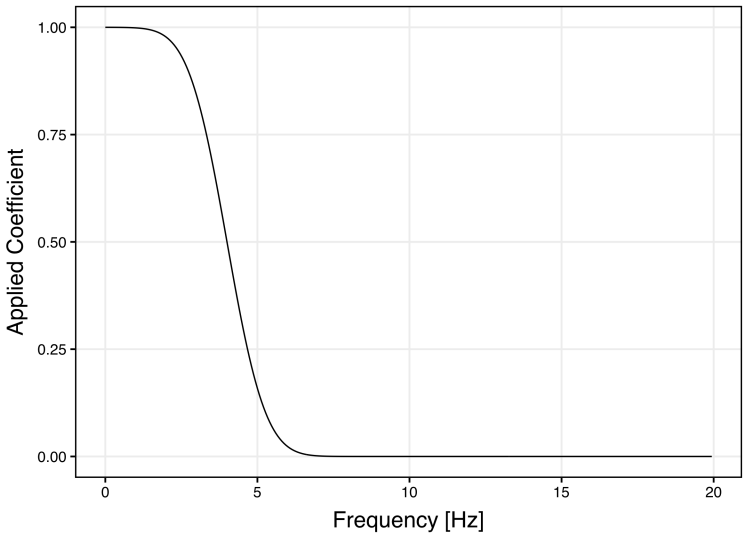


Figure 4.11: Cumulative density function for coefficient applied in frequency domain (continues to Nyquist Frequency; limited view shown to see variation at low frequencies).

time history for the selected trial from the test of Single Longitudinal debris is shown in Figure 4.12. Applying this same methodology to all trials of the unbroken wave only, Single Longitudinal (1L), and Single Transverse Trials (1T), Figure 4.13 is obtained.

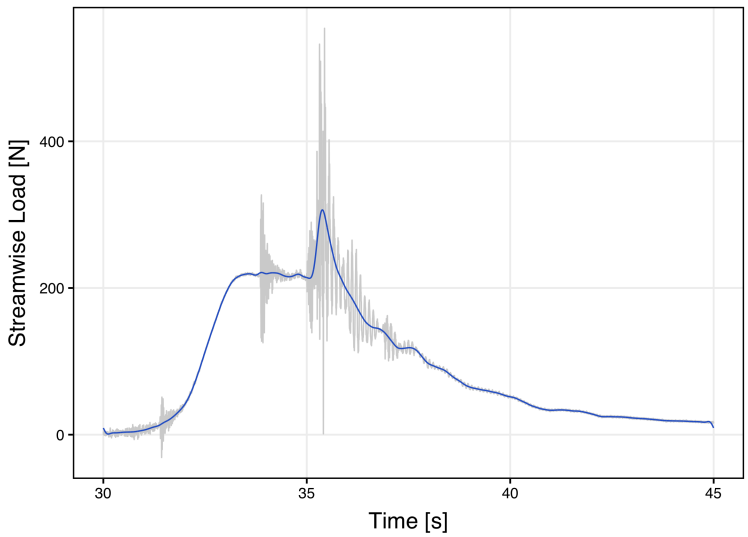


Figure 4.12: High-pass filtered streamwise load values of Single Longitudinal debris (1L) selected trial in BLUE versus unfiltered values in GRAY.

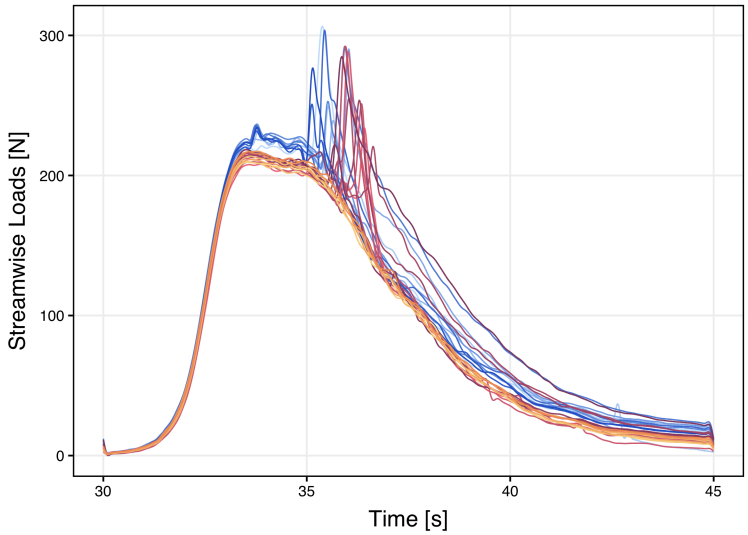


Figure 4.13: All trials of high-pass filtered streamwise load values of Single Longitudinal (BLUE gradient), Single Transverse (PURPLE gradient), and Unbroken Wave Only (ORANGE gradient).

The large, high-frequency peaks have been filtered out of the time history and the low-frequency signal remains. The unbroken wave-only trials remain consistent and of a similar profile to unfiltered values, since the signal is primarily low-frequency.

We define a region after the impacts but before a return to "0". By visual inspection, approximately 38.75 seconds is after peaks occur but before trials reconverge at 0. At 38.75 seconds experiment time, the median-value trial for each experiment is plotted in Figure 4.14, with median values shown in Table 4.7.

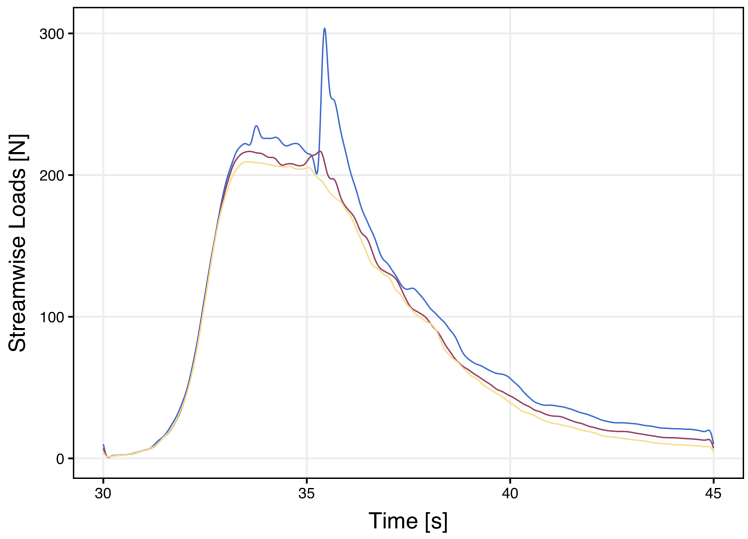


Figure 4.14: Median-value trials after high-pass filtering for Single Longitudinal (BLUE), Single Transverse (PURPLE), and Unbroken Wave Only (ORANGE).

Table 4.7: Median damming streamwise loads and interquartile range

| Name | Median Damming Load at 38.75 s [N] | IQR [N] |
|---|---|---|
| Unbroken Wave Only | 66.60 | 2.53 |
| Single Longitudinal (1L) | 13.6 | 44.1 |
| Single Transverse (1T) | 17.4 | 78.5 |

Taking the median trial, there is negligible difference between the damming forces seen in the debris trial and the forces for the wave only. However, one can observe a significant range in the values measured at this instance. If one takes the maximum trial instead of the median trial, Figure 4.15 and Table 4.8 are obtained.

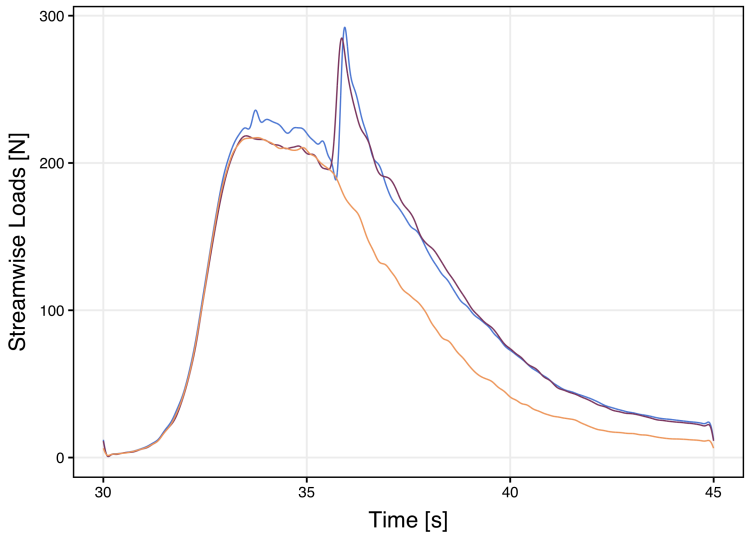


Figure 4.15: Max-value trials at 38.75 seconds after high-pass filtering for Single Longitudinal (BLUE), Single Transverse (PURPLE), and Unbroken Wave Only (ORANGE).

Table 4.8: Max damming streamwise loads and interquartile range

| Name | Max Damming Load at 38.75 s [N] |
|---|---|
| Unbroken Wave Only | 70.0 |
| Single Longitudinal (1L) | 107.6 |
| Single Transverse (1T) | 114.2 |

While these trials do not represent the median values that are discussed in the majority of this analysis, they represent valid trials in which an increase of surface area led to increased streamwise load due to the trapping of the single piece of debris. Regardless of orientation,

it is observable that the trapping of a single piece of debris leads to an increased damming force of approximately 50 N, which is nearly 160% of the streamwise load at this time due to the wave only. With the larger numbers of debris in subsequent analysis, this is an important phenomenon.

## *4.2 Multiple Debris: Longitudinal & Transverse*

In the previous section, discussion focused on single debris tests and the unbroken wave only. Now, the discussion is extended to include structured and tightly-packed configurations of multiple debris in which the orientation of individual debris is either longitudinal or transverse to the direction of flow. Refer to Figure 4.1 for configurations of debris.

### *4.2.1 Maximum, First, & Second Peak Loads*

Following the same method applied to single debris trials, we investigate the normality of the regular trials with multiple debris. Unfiltered time histories for all 10 trials with 8 debris and unbroken wave-only trials are shown in Figure 4.16. Note: certain trials have been removed from the following discussion due to erroneous load cell data that do not return to approximately zero via setting a bound that the average value after 200 seconds can not exceed one-quarter peak unbroken wave load median value in magnitude. Load cell data from these trials are assumed to be in error due to instrument malfunction. No more than two trials have been removed per test in this set.

A similar pattern in which there are two impact periods and then sustained damming force after impacts is observed as in the single debris trials. The magnitude of these forces, however, has increased.

Figure 4.17 investigates all four tests with 16 debris in regular configuration. While the orientations of debris in longitudinal and transverse trials were maintained, different arrays were tested. Figure 5.5c investigates both tests in which 24 debris in a regular configuration were investigated. All time histories follow an approximately normal distribution for the absolute maximum peak, first peak, and second peak. QQ-plots for all peak values are shown

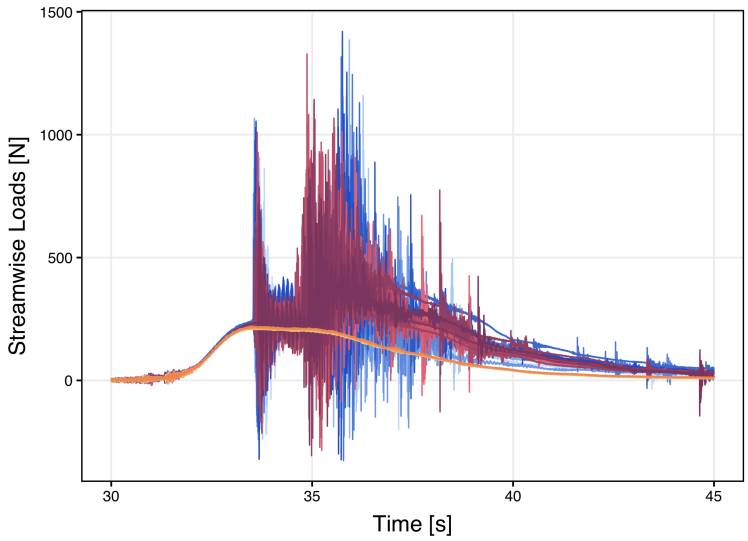


Figure 4.16: All 8 Longitudinal (BLUE gradient), 8 Transverse (PURPLE gradient), and Unbroken Wave Only (ORANGE gradient) trials streamwise load time histories.

in Appendix C. Table 4.9 shows the Shapiro-Wilk value, the median load, the interquartile range for each trial, and the median time of peak impact for each trial. Table 4.10 shows the Shapiro-Wilk value, the median peak load, the interquartile range for each trial, and the median time of FIRST peak impact for each trial. Table 4.11 shows the Shapiro-Wilk value, the median peak load, the interquartile range for each trial, and the median time of SECOND peak impact for each trial.

For the absolute maximum values per trial, we resolve the median values for each experiment and normalize them by the median absolute peak value obtained for single longitudinal debris trials. The "1L" absolute peak value median was selected as a normalization factor because it is highly repeatable and can be used as a basis of comparison for all debris configurations. Sorting by number of debris, we obtain Figure 4.19. One can observe a clear trend of increasing force with increasing number of debris. This is logical given an increase in mass in the debris field, which one would expect to have increased force according to

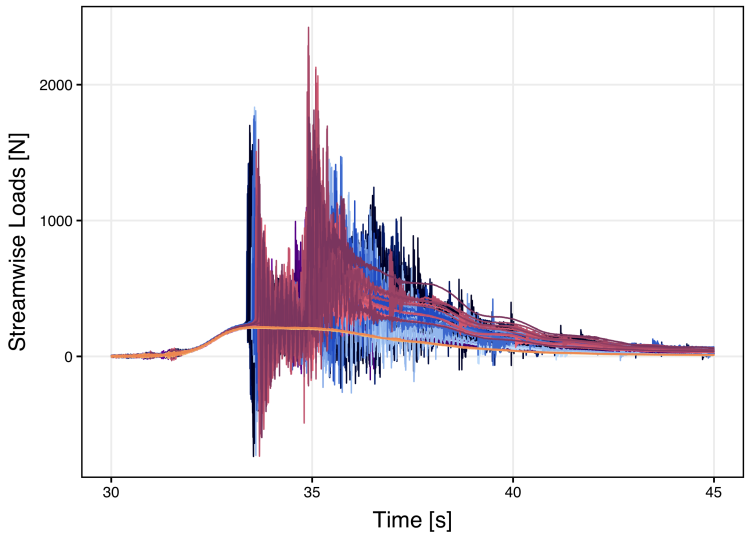


Figure 4.17: All 16 Longitudinal Configuration 1 (LIGHT BLUE gradient), 16 Transverse Configuration 1 (LIGHT PURPLE gradient), 16 Longitudinal Configuration 2 (DARK BLUE gradient), 16 Transverse Configuration 2 (DARK PURPLE gradient), and Unbroken Wave Only (ORANGE gradient) trials streamwise load time histories.

Table 4.9: Total streamwise loads median maximum peak values, interquartile range, and median time of maximum peak value per trial for all multiple debris, regular configurations

| Name | P-Value | Median Peak Load [N] | IQR [N] | Median Time at Peak per Trial [s] |
|---|---|---|---|---|
| 8L | 0.54 | 1107.2 | 253.7 | 35.77 |
| 8T | 0.42 | 973.9 | 142.1 | 35.12 |
| 16L1 | 0.14 | 1463.7 | 477.1 | 33.6 |
| 16T1 | 0.59 | 1662.3 | 580.6 | 35.07 |
| 16L2 | 0.76 | 1429.3 | 140.2 | 33.45 |
| 16T2 | 0.030 | 671.7 | 196.3 | 34.58 |
| 24L | 0.59 | 2116.9 | 286.3 | 33.47 |
| 24T | 0.031 | 1211.4 | 473.5 | 35.03 |

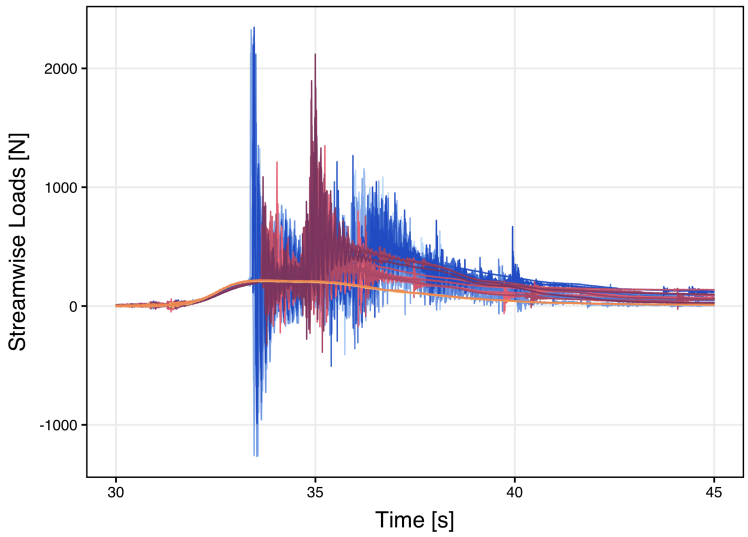


Figure 4.18: All 24 Longitudinal (BLUE gradient), 24 Transverse (PURPLE gradient), and Unbroken Wave Only (ORANGE gradient) trials streamwise load time histories.

Table 4.10: Total streamwise loads median FIRST peak values, interquartile range, and median time of first peak value per trial for all multiple debris, regular configurations.

| Name | P-Value | Median Peak Load [N] | IQR [N] | Median Time at First Peak per Trial [s] |
|---|---|---|---|---|
| 8L | 0.57 | 941.4 | 133.0 | 33.59 |
| 8T | 0.080 | 675.9 | 135.2 | 33.65 |
| 16L1 | 0.13 | 1389.5 | 477.1 | 33.58 |
| 16T1 | 0.85 | 1284.1 | 225.6 | 33.67 |
| 16L2 | 0.76 | 1429.3 | 140.2 | 33.45 |
| 16T2 | 0.37 | 603.3 | 69.8 | 33.81 |
| 24L | 0.59 | 2116.9 | 286.3 | 33.47 |
| 24T | 0.089 | 797.3 | 115.9 | 33.86 |

$F = ma$. However, a linearly increasing peak force is not observed with linearly increasing mass. Instead, we see force increasing at decreasing rate with number of debris. In regards to the exception at 16 debris with configuration T2, many debris are actually outside of the

Table 4.11: Total streamwise loads median SECOND peak values, interquartile range, and median time of second peak value per trial for all multiple debris, regular configurations.

| Name | P-Value | Median Peak Load [N] | IQR [N] | Median Time at Second Peak per Trial [s] |
|---|---|---|---|---|
| 8L | 0.88 | 1107.2 | 328.5 | 35.86 |
| 8T | 0.42 | 973.9 | 142.1 | 35.12 |
| 16L1 | 0.11 | 1391.9 | 244.2 | 35.70 |
| 16T1 | 0.59 | 1662.3 | 580.6 | 35.07 |
| 16L2 | 0.94 | 1017.5 | 137.3 | 36.55 |
| 16T2 | 0.015 | 636.0 | 223.8 | 34.63 |
| 24L | 0.63 | 1059.7 | 163.8 | 36.09 |
| 24T | 0.031 | 1211.4 | 473.5 | 35.03 |

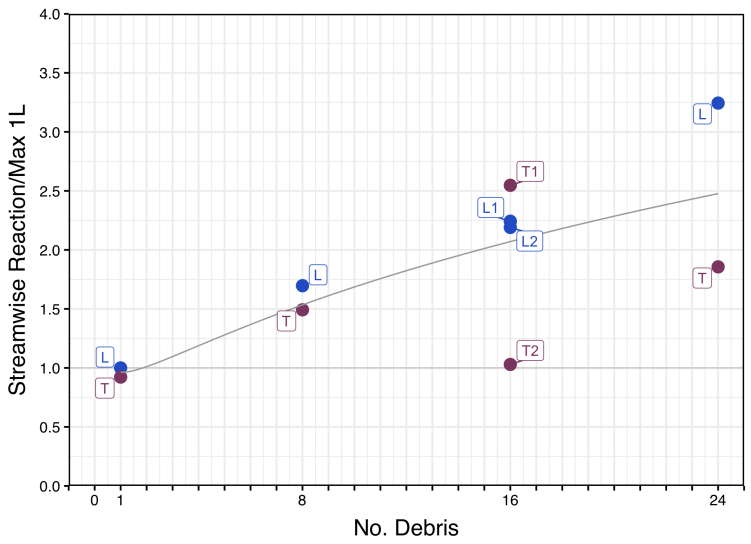


Figure 4.19: Median maximum trial values for all "regular" debris configurations; BLUE indicates longitudinal orientation, PURPLE indicates transverse orientation.

front face area of the test structure; in other words, the debris may miss the test structure and flow past. See Figure 4.20.

Also visible in the plot is that for most numbers of debris, the longitudinally oriented

Figure 4.20: Initial configuration for 16 debris transverse configuration 2.

configurations tend to have a higher peak value. All debris act together as the front faces of the front debris contact the structure, with the following debris contacting the debris in front within a short amount of time; the peak is close to the combined mass impacting at once. An exception is 16 debris with configuration T1. In this case, all of the debris hit the structure concurrently and have the same shape as debris test L1. This indicates that the mass impacting the tightly-packed structured debris field is more directly correlated with peak force than the orientation of individual debris when the debris field has the same extents.

The normalized interquartile range is plotted for the median maximum trial value in Figure 4.21. The normalized interquartile range decreases after one debris, but remains fairly level throughout trials with higher numbers of debris. This is somewhat counterintuitive, because more debris could yield higher variability due to more opportunities for varied impacts with the structure. The normalized interquartile range scales approximately proportionally to the number of debris for higher number trials. We see the longitudinal configurations tend

to yield higher variation. This result may mean more debris impact at once, thus yielding less variation during the maximum peak time range. Transverse debris appear to have a higher normalized interquartile range for the same number of debris.

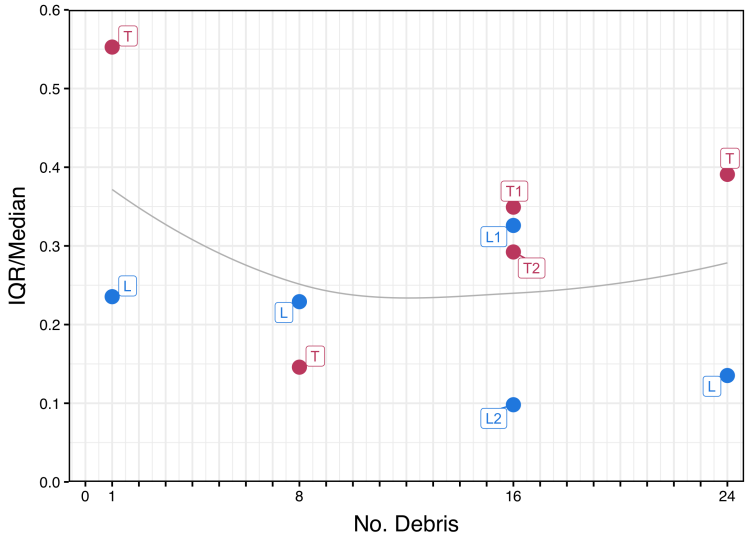


Figure 4.21: Normalized interquartile range for absolute maximum trial values for all "regular" debris configurations; BLUE indicates longitudinal orientation, PURPLE indicates transverse orientation.

To more thoroughly understand the trends within tightly-packed configurations, we explore the first and second peak medians between trials. Figure 4.22 shows the first peak medians normalized by the median absolute peak value for single longitudinal debris trials. Given the first peak values above, the longitudinal values are higher than transverse values for all numbers of debris. Also, longitudinal configurations show a clear increase with number of debris; however, transverse configurations seem to show that 8, 16, and 24 debris tests have a fairly similar first peak value. This is likely due to a lack of cohesion in the debris field. In single debris trials with transverse configuration, slowing and rotation before contact with the test structure tended to be present. In the same way, one can conclude that

there is a decreasing debris field density and a lack of field cohesion on initial contact with the structure; therefore, less of the total mass is contacting at once.

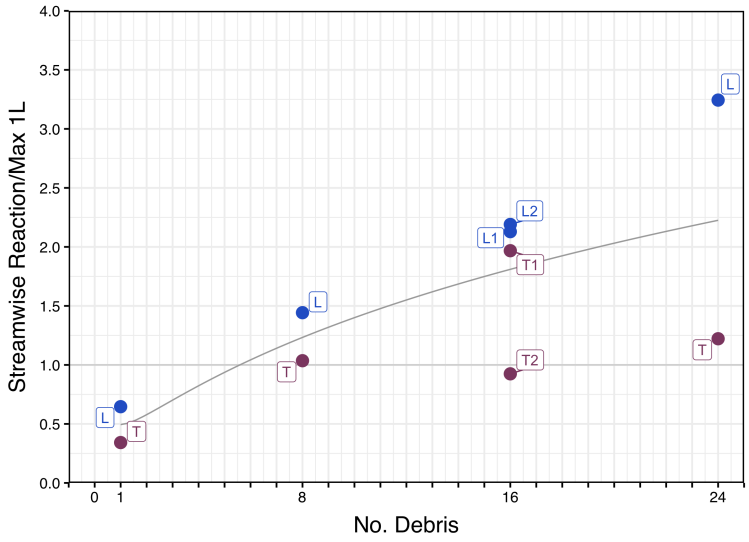


Figure 4.22: Median FIRST peak values for all "regular" debris configurations; BLUE indicates longitudinal orientation, PURPLE indicates transverse orientation.

The normalized interquartile range is plotted for median first peak trial value in Figure 4.23. For the FIRST maximum peak value, the normalized interquartile range increases moderately with number of debris, but is lower per configuration than the absolute maximum peak ranges. In this case, single debris have the lowest normalized interquartile range. The first impact with a single debris is singular and similar to an elastic collision, so this result is in line with intuition. Additionally, during the first peak (hypothesized to be the first contact with the box) the configuration is still regular and can experience impact in a very short time amount of time. In general, we observe that longitudinal configurations have smaller ranges.

Figure 4.24 shows the second peak medians normalized by median absolute peak value for single longitudinal debris trials. The second peak medians show a less clear correlation

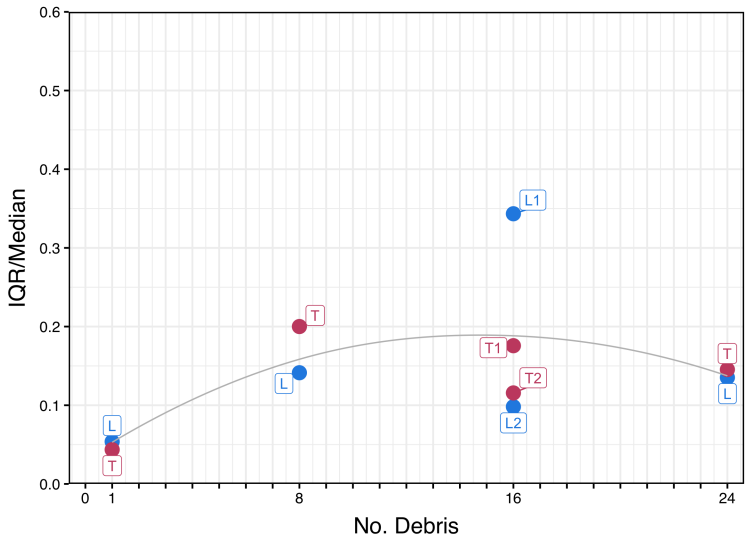


Figure 4.23: Normalized interquartile range for first peak trial values for all "regular" debris configurations; BLUE indicates longitudinal orientation, PURPLE indicates transverse orientation.

with number of debris and with longitudinal and transverse debris. This is likely due to the increasingly chaotic nature of the second impact time period. Observing the time histories in earlier figures, the second peak is chaotic and likely due to multiple impacts occurring as debris flow underneath and around the structure. In the case of 24 debris, more debris are likely to miss the structure given the size of the initial layouts (i.e., the layout extents exceed the face of the test structure). Additionally, 24 debris in a longitudinal configuration had a high initial impact force, which likely served to break up the long debris field and cause debris pieces to miss the structure during the second impact time frame.

The normalized interquartile range is plotted for median second peak trial value in Figure 4.25. The SECOND peak ranges follow a similar trend to absolute peak ranges. This makes sense since most absolute peaks occur as second peaks. In general, longitudinal values tend to be lower, except at 8 debris tests. The single debris trials have the highest normalized

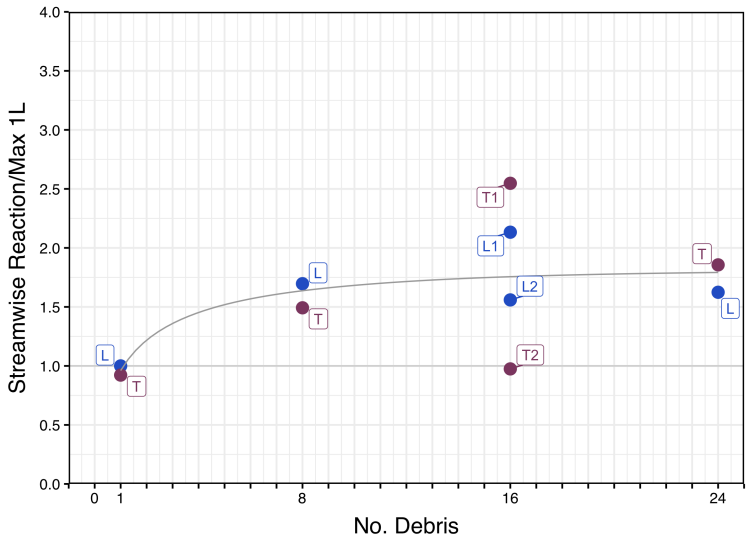


Figure 4.24: Median SECOND peak values for all "regular" debris configurations; BLUE indicates longitudinal orientation, PURPLE indicates transverse orientation.

interquartile ranges.

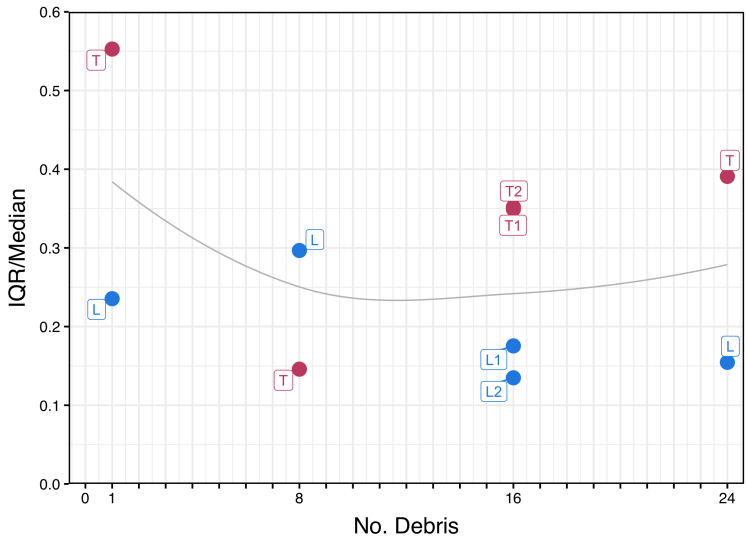


Figure 4.25: Normalized interquartile range for second peak trial values for all "regular" debris configurations; BLUE indicates longitudinal orientation, PURPLE indicates transverse orientation.

### *4.2.2 Damming Loads*

Damming loads exist after the initial impact as debris caught on the test structure increase the surface area of the test structure and thus the applied hydrodynamic load. By following the same method employed for single debris trials, we can filter out frequencies in excess of approximately 4 Hz and reconstruct time histories via inverse Fast Fourier Transform. The following median damming loads are reported at 38.75 s experiment time in Table 4.12.

Substantial ranges of damming loads are observed. Figure 4.26 shows median damming loads less the median wave-only reaction force at 38.75 seconds, then normalized by the median peak reaction force at all times due to the wave throughout all trials. This method both isolates and normalizes the damming loads. The highest median damming forces appear to occur at the 16 debris range, with T2 (i.e., most debris pieces missing the structure) excepted. T1 is the highest median damming value. The median damming values for both

Table 4.12: Median damming streamwise loads per trial and interquartile range

| Name | Median Damming Load at 38.75 s [N] | IQR [N] |
|---|---|---|
| 8L | 159.2 | 41.5 |
| 8T | 165.1 | 15.9 |
| 16L1 | 202.7 | 74.3 |
| 16T1 | 248.4 | 102.5 |
| 16L2 | 181.4 | 89.9 |
| 16T2 | 81.2 | 30.3 |
| 24L | 192.9 | 58.8 |
| 24T | 182.4 | 76.6 |

single debris trials are highly similar (as seen in the above section focusing on single debris trials). The maximum median damming value is for 16 debris configuration T1 - this indicated that transverse debris are more likely to become caught and dam. 24 debris trials are not higher than 16 debris trials at median, which likely indicates that after initial impacts, debris tend to miss the structure and not dam. We note that although median damming forces do not exceed the wave-only load at 38.75 seconds, they can be up to approximately 90%. This is structurally significant due to the low-frequency, sustained nature of damming.

The normalized interquartile range is plotted for all regular tests in Figure 4.27. For damming loads, the normalized interquartile ranges increase for moderate numbers of debris as shown by the trend line; however, there is substantial variation in 8 debris tests, where the longitudinal configuration has a much higher range than the transverse debris configuration. The normalized interquartile range for 24 debris is relatively low, likely due to its high damming force. In general, there is a less clear correlation between damming force ranges than with peak force ranges.

Since each debris motion and propensity for damming during each trial is independent of other trials, one can also use each test's maximum value trial at 38.75 seconds as a point of comparison of damming loads. The maximum values are represented in Table 4.13 below.

Figure 4.28 shows all maximum trial values for damming loads less the median wave-only

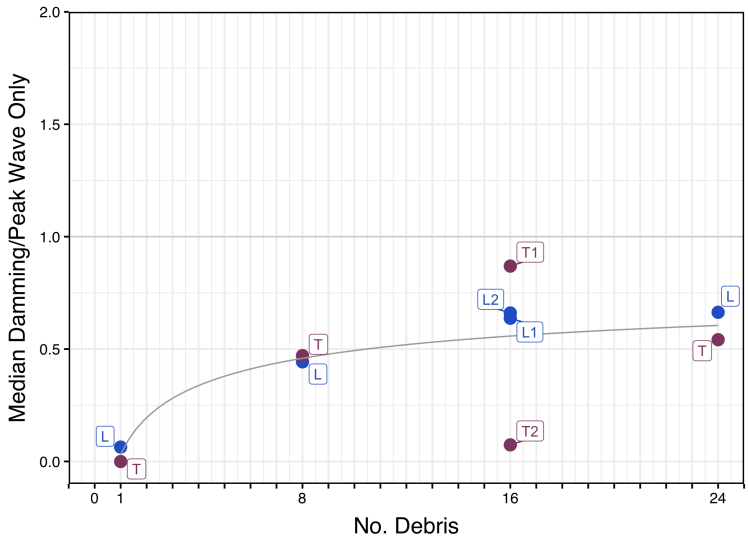


Figure 4.26: Median damming values taken at 38.75 s for all "regular" debris configurations; BLUE indicates longitudinal orientation, PURPLE indicates transverse orientation.

Table 4.13: Maximum trial damming streamwise loads for "regular" tests

| Name | Max Damming Load at 38.75 s [N] |
|---|---|
| 8L | 278.6 |
| 8T | 210.3 |
| 16L1 | 269.5 |
| 16T1 | 386.6 |
| 16L2 | 288.3 |
| 16T2 | 175.5 |
| 24L | 311.7 |
| 24T | 253.5 |

load at that time and normalized by the median peak reaction force at all times due to the wave throughout all trials. The same approximate pattern is observed as with median trials: the highest damming occurs at 16 debris configuration T1. In general, tests with longitudinal debris orientations have higher maximum damming forces.

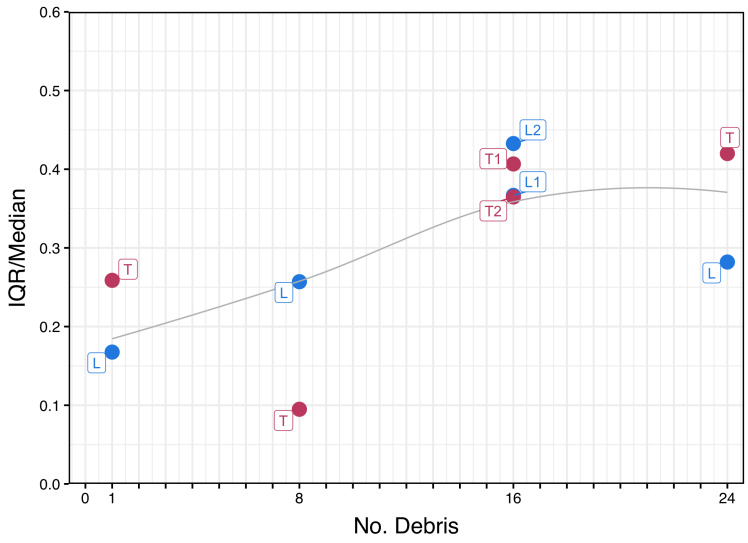


Figure 4.27: Normalized interquartile range for damming loads for all "regular" debris configurations; BLUE indicates longitudinal orientation, PURPLE indicates transverse orientation.

In most cases with more than single debris, the damming loads represent a 200% increase in loads from just the unbroken wave case at that instant. Again, this indicates that low-frequency damming loads found via high pass filtering are significant, sustained structural loads and should be the subject of further study.

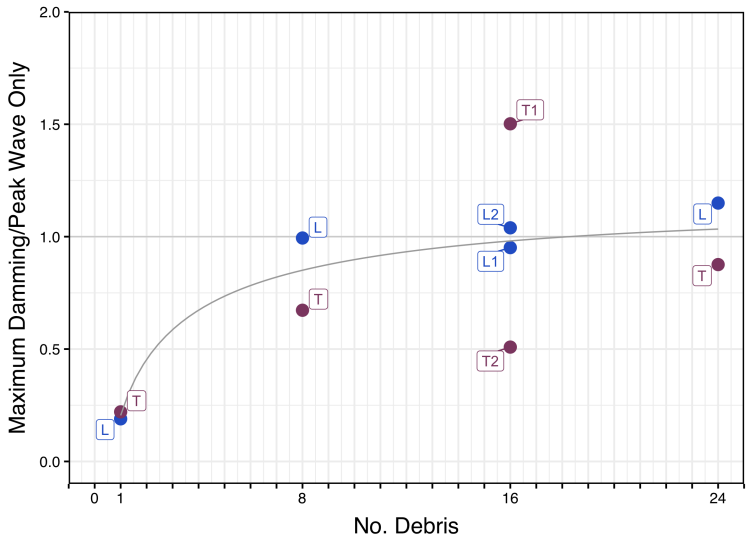


Figure 4.28: Maximum damming values taken at 38.75 s for all "regular" debris configurations; BLUE indicates longitudinal orientation, PURPLE indicates transverse orientation.

## *4.3 Qualitative Video Analysis*

This analysis focuses on distinct phenomena that occur in time series recorded by two in-line load cells located on the downstream face of the test structure. The time histories show two distinct impact regions and a region of elevated force correlated to damming phenomena after these impacts. While the correlation of the peak phenomena to specific events requires in-depth video analysis to follow this scope of work, this text hypothesizes that the "double-peak" pattern is due to an initial collision between the downstream face of the debris field and the upstream face of the box.

In this section, images and video are qualitatively analyzed to explain the dominant phenomena seen in streamwise time history forcing. Again, specific image analysis is not within the scope of this text but will be pursued in future work.

Beginning with single debris, both high speed (500 frames per second) and GoPro (120 frames per second) were trained on the front face of the test structure and path of debris,

respectively. Figure 4.29 shows a time history of a single trial for a single, longitudinally oriented debris.

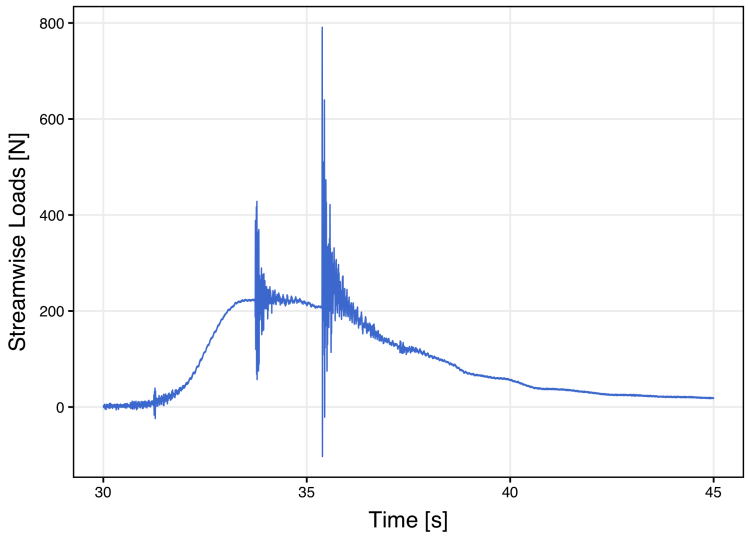


Figure 4.29: Time history for total streamwise force a selected trial conducted with a single longitudinal debris.

The time history shows a distinct, high-frequency signal at the first impact of the debris, which occurs at approximately 33.5 seconds. The next peak is at approximately 35 seconds. Stills captured show an initial impact at 33.5 when the front face of the debris contacts the box. The collision time is approximately 0.00175 seconds under ideal conditions. The dynamics of the initial impact of a single longitudinal is discussed in more depth in Appendix B, which considers a single degree of freedom system impact of an axial rod under ideal, in-air conditions.

Qualitative analysis is performed by identifying the first visible impact of the debris with the test structure. We hypothesize that this impact is the first "peak" that deviates from an otherwise smooth, low-frequency signal presented by the unbroken wave load profile (ref. Chapter 3). The images used are taken from a high-speed camera video taken of the above

trial with 500 frames per second over a period of 10 seconds. The total high-speed video time is 167 seconds, which translates to roughly 16.7 seconds of video time to 1 second of real experiment time.

The first impact maximum value occurs at 33.77 seconds, and the second impact maximum value at approximately 35.38. With a total separation of 1.61 seconds, the expected frames representing this segment are more than 800, and represent a high-speed video separation of 26.8 seconds. Figure 4.30 shows a series of images from video starting at the initial impact and continuing through visible debris motion.

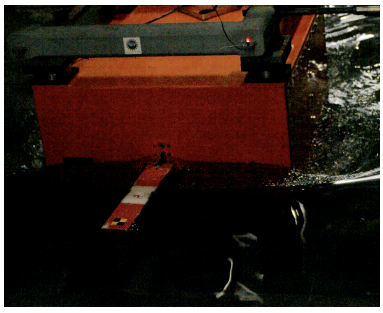

(a) Image at approximate time of first collision.

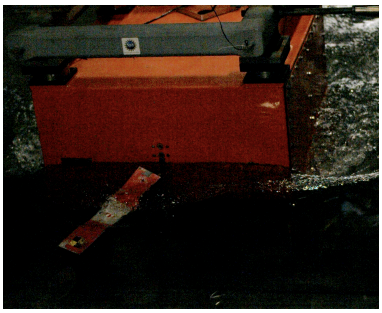

(b) Image at approximately 0.8 seconds after first collision and 0.8 seconds before second collision.

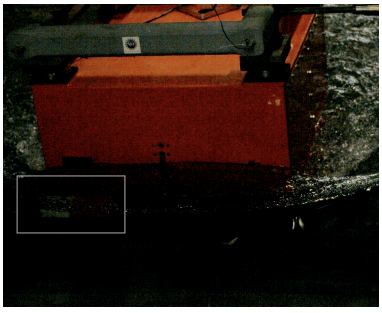

(c) Image at time of hypothesized second collision.

Figure 4.30: Images from hypothesized first and second collision times from selected trial of single longitudinal debris. Box indicates location of submerged debris.

Just after this initial impact, the debris shows motion in the opposite direction of flow, similar to an elastic collision, in which it loses contact with the box. Within approximately 0.8 seconds, the debris has rotated and pitched such that debris is beginning to submerge and change its orientation while it again accelerates in the direction of flow. The last image shows the debris submerged and underneath the test structure face, where it is hypothesized to contact the structure's legs at 1.6 seconds after the initial impact.

Damming is considered to be when debris increases the hydrostatic force on the structure due to an increase in the area exposed to the flow, as a debris may become trapped underneath the test structure within the legs of the test structure. In the case of a single longitudinal debris, the debris goes underneath the structure, and thus has no video data available.

We note that while the hypothesized causes of the first and second impact appear supported by qualitative data analysis, further video analysis is required to confirm the causality of time history features. However, further supporting evidence is provided by considering a larger debris field and conducting a similar visual analysis. Figure 4.31 shows the selected time history from a single trial of 8 debris oriented longitudinally (8L). In this case, the maximum value for the first peak is 33.69 seconds. The next peak value occurs at 36.27 seconds. The high-speed has captured this instance in approximately 1300 frames. A similar analysis is performed with an 8 longitudinal debris trial as with the single debris trial, shown in Figure 4.32. We note that there are more, smaller peaks after the second large peak in the shown time history; for the purposes of this text, the "second" peak is taken to be the maximum peak value in the region following the initial collision. In most trials with multiple debris, several peaks are observed.

A typical pattern is observed between all regular configurations with multiple debris. After the first impact, the upstream debris (further from the face) experience a collision in which the debris field breaks up. The debris lose the regularity of their configuration as they lose contact with the box, rotating and changing directions of motion from purely streamwise. They are either pushed around the box in its wake or are submerged and flow underneath. In this case, the debris are not shown at the time of the hypothesized second peak, indicating they are underneath the test structure. Damming, again, is not visible in the images due to the angle of the camera, but in this case, the low-frequency signal seen after impact at approximately 38 seconds is likely due to this phenomenon.

In general, the paths of debris throughout a trial are nondeterministic; further study seeks to reconstruct their paths via onboard accelerometers and is out of the scope of this work. Further, video analysis beyond the qualitative analysis presented here is necessary to

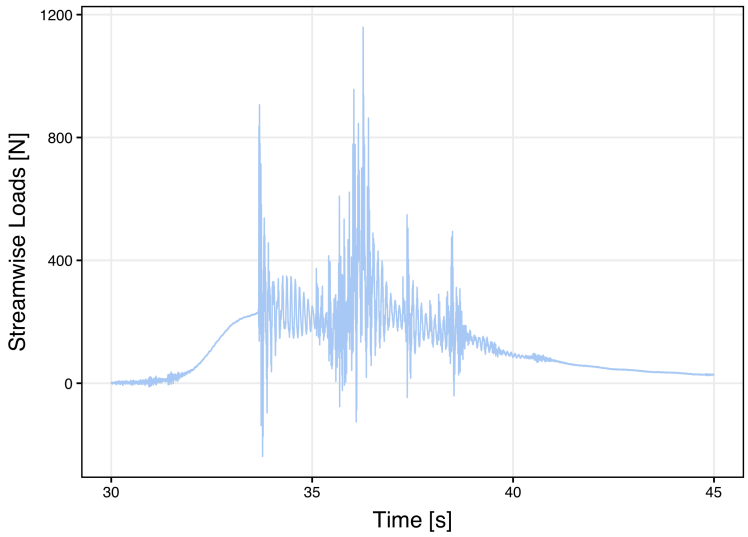


Figure 4.31: Time history for total streamwise force for a selected trial conducted with a single longitudinal debris.

understand the precise instances of time histories' peaks and collisions.

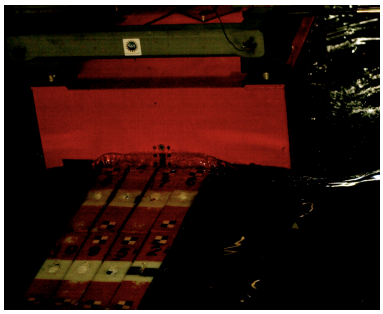

(a) Image at approximate time of first collision.

(b) Image at approximately 0.8 seconds after first collision and 0.8 seconds before second collision.

(c) Image at time of hypothesized second collision.

Figure 4.32: Images from hypothesized first and second collision times from selected trial of single longitudinal debris.

# Chapter 5

# STREAMWISE REACTIONS DUE TO RANDOM DEBRIS CONFIGURATIONS

This chapter extends the discussion from "regular" configurations, in which debris were tightly-packed and structured, to "random" configurations with lower surface area density. A total of nine tests with 10 trials each were conducted in this manner. In these tests, debris were not placed in exact positions, but rather, were placed free-floating in a specified starting area. The following conditions were employed during this phase: 1) unbroken wave, 2) wooden (lift) frame, 3) standard-sized debris, and 4) random (unstructured) configurations.

This chapter discusses the effects of the following variables:

1. number of debris
2. debris surface area density

Figure 5.1 shows a typical configuration for a random debris field. The outer extents of the debris field are situated with the rightmost edge 2m from the upstream face of the test structure. The flow is from left to right. The variable $\alpha$ represents the dimension of the square maximum debris field extents. Using $\alpha$ and the surface area of a neutrally-buoyant debris piece, one can calculate initial debris field density, defined as $\rho_f$ (the surface area of debris divided by the surface area of the debris field area). All cases in the random configuration have an initial debris field density less than 100%; this differentiates the tests from "regular", structured debris tests, in which all initial fields had 100% surface area density. The experimental configurations are listed in Table 6.1 below. Note: one test does not have square dimensions since its width was defined by the total width of the flume (3.7m).

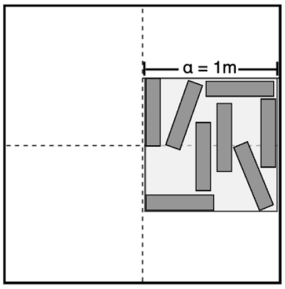


Figure 5.1: Typical "random" configuration for tests conducted with standard-sized debris, unbroken wave, and the wooden "lift" frame.

Table 5.1: List of "random" configurations: number of debris, debris field extents, and initial field density.

| No. Debris | $\alpha$ [m] | $\rho_f$ |
|---|---|---|
| 8 | 0.75 | 0.73 |
| 8 | 1 | 0.41 |
| 16 | 1 | 0.82 |
| 16 | 1.25 | 0.52 |
| 16 | 1.5 | 0.36 |
| 24 | 1.25 | 0.78 |
| 24 | 1.5 | 0.54 |
| 24 | 2 | 0.31 |
| 24 | 2x3.7 | 0.17 |

### *5.1 Peak Loads*

First, we discuss random configurations independently of regular configurations. Two tests were conducted with 8 debris with initial debris extents either a 0.75-m square or 1.0-m square, with the former having greater surface area density (0.73 vs. 0.41). Figure 5.2 shows unfiltered time histories for all trials with 8 debris in a random configuration. The unbroken wave-only trials are also shown. Note: certain trials have been removed from the following

discussion due to erroneous load cell data that do not return to an approximately "zero-ed" position via setting a bound that the average value after 200 seconds could not exceed one-quarter peak unbroken wave load median in magnitude. Load cell data from these trials are assumed to be in error due to equipment malfunction. No more than two trials have been removed per test in this set.

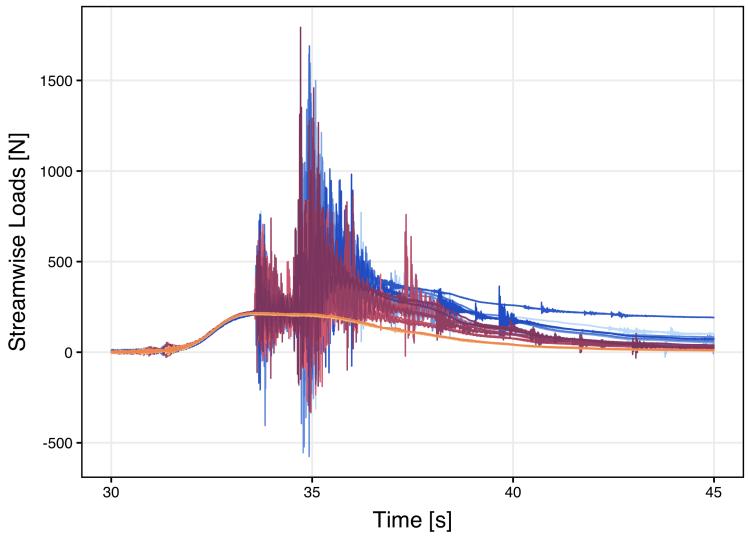


Figure 5.2: All trials of random configurations with 8 debris tests and unbroken wave-only tests. PURPLE gradient indicates $\rho_f = 0.41$; BLUE gradient indicates $\rho_f = 0.73$; ORANGE gradient indicates Unbroken Wave-Only trials.

Similar to the "regular" configurations, the peaks for the trials with debris are much higher than the wave only, there are two dominant peaks (one before 34.5 seconds and one after), and the low-frequency signal after impacts is elevated above the Unbroken Wave-Only signal and indicates damming loads (after approximately 37 seconds). By observation, one can conclude that trials shown in Figure 5.2 are of similar shape to those observed in "regular" configurations.

There are additional peaks shown after the two primary peak regions that occur in single,

individual trials. The presence of these single-trial peaks outside of the primary peak region is not as prominent in the regular configurations, and thus may indicate increased variability between trials in random configurations. Additionally, a single trial in the $\rho_f = 0.41$ test indicates a high damming signal. This is not determined to be a result of equipment variability, as it does not meet the "non-zeroing" criteria required to be considered an excluded trial. As discussed within regular debris configurations (Chapter 4), excluded trials require the absolute value of the average load after 200 seconds to be more than one-quarter of the maximum wave-only load ( 50 N). This event is thus not excluded and is considered in damming analysis. Again, the presence of this high damming value within an individual trial indicates the higher degree of variability between trials represented by random configurations.

Figure 5.3 shows all three tests with 16 debris in "random" configurations. Density increases from $\rho_f = 0.36$ to $\rho_f = 0.82$. The highest peaks are observed during the second peak period (after 34.5 seconds) from the most dense test, $\rho_f = 0.82$. We see single trial peaks at later times indicative of high variability between trials. The first peak, second peak, and post-peak damming loads are observable.

Figure 5.4 shows all trial time histories for four random configurations with 24 debris. The lowest density test spans the full width of the flume (3.7m) and extends to fill the 2m extents of the debris frame in the streamwise direction. The highest peaks are from $\rho_f = 0.78$ trials during the first peak duration (before 34.5 seconds). This is the densest test in the random configurations. The shape of the trials follows similar patterns (first peak, second peak, then damming). Again, we observe peaks throughout the time history within singular trials, and conclude that there is randomness between trials of the same configurations.

To show the diversity of random configurations during the experiment, Figure 5.5 shows selected trials for three configurations with varying numbers of debris.

Table 5.2 summarizes the statistics related to the total streamwise absolute maximum peaks for all random configurations tested with the unbroken wave, wooden (lift) frame, and standard-sized debris. Shapiro-Wilk tests are applied to all tests and reported (further statistical discussion is found in Chapter 4). A P-value above 0.05 indicates the distribution

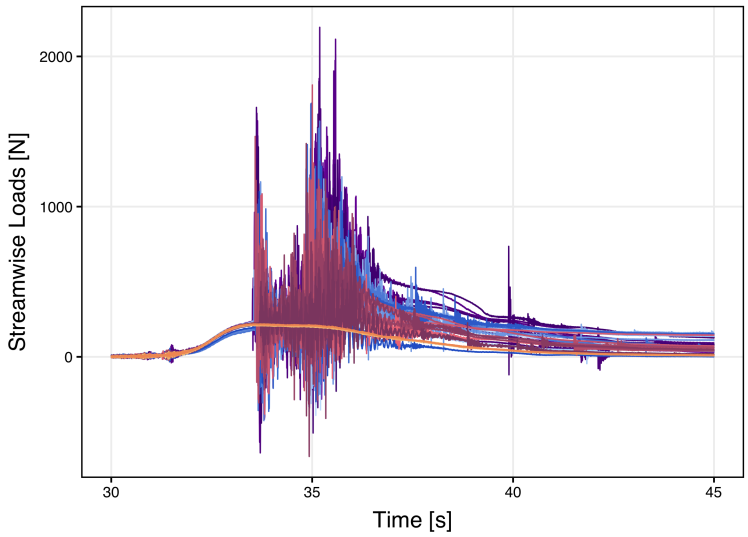


Figure 5.3: All trials of random configurations with 16 debris tests and unbroken wave-only tests. PURPLE gradient indicates $\rho_f = 0.36$; BLUE gradient indicates $\rho_f = 0.52$; DARK PURPLE gradient indicates $\rho_f = 0.82$; ORANGE gradient indicates Unbroken Wave-Only trials.

can be assumed normal; while some P-values are under this value, observation of QQ-plots (reference Appendix C) indicates approximate linearity. In all cases, a median value is taken.

Table 5.3 follows a similar process for the maximum values before 34.5 seconds experiment time (i.e., FIRST peak values). Table 5.4 follows the process for after 34.5 seconds (i.e., SECOND peak). We observe that most median times of peak values per trial from the median absolute maximum load occur after 34.5 seconds. The densest 24 debris trials are an exception, with its median peak value time before 34.5 seconds. During the first peak, the largest median peak load values are observed in the densest configurations with 16 and 24 debris. The majority of values are not the absolute maximum values. There is a large spread for most of the configurations, with larger interquartile ranges generally found for less dense configurations and more debris.

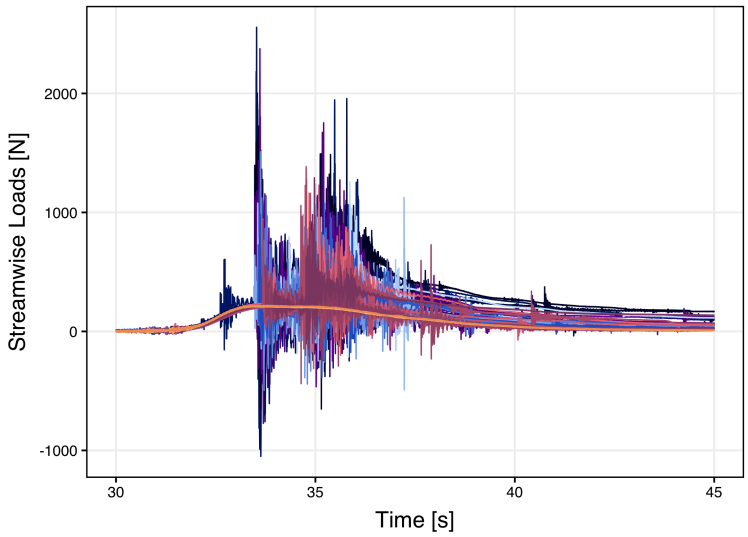


Figure 5.4: All trials of random configurations with 24 debris tests and unbroken wave-only tests. PURPLE gradient indicates $\rho_f = 0.17$; BLUE gradient indicates $\rho_f = 0.31$; DARK PURPLE gradient indicates $\rho_f = 0.54$; DARK BLUE gradient indicates $\rho_f = 0.78$; ORANGE gradient indicates Unbroken Wave-Only trials.

Second peak values are generally higher than their first peak counterparts. Additionally, the interquartile range tends to be lower during the second peak. Despite the time histories showing variation between trials, most trials have similar maximum value locations and show relatively low ranges in peak values during this time period.

(a) Initial configuration for selected trial with 8 debris and $\rho_f = 0.73$.

(b) Initial configuration for selected trial with 16 debris and $\rho_f = 0.52$.

(c) Initial configuration for selected trial with 24 debris and $\rho_f = 0.17$.

Figure 5.5: Initial configurations for select random configuration trials.

Table 5.2: Total streamwise median maximum peak values per trial, Shapiro-Wilk P-value, interquartile range, and median time of absolute max peak value per trial for all multiple debris, random configurations.

| No. Debris | $\rho_f$ | P-Value | Median Peak Load [N] | IQR [N] | Median Peak Time [s] |
|---|---|---|---|---|---|
| 8 | 0.73 | 0.085 | 1173.9 | 456.5 | 34.94 |
| 8 | 0.41 | 0.0020 | 845.4 | 382.3 | 35.01 |
| 16 | 0.82 | 0.94 | 1616.1 | 417.7 | 35.18 |
| 16 | 0.52 | 0.90 | 1273.3 | 369.4 | 35.17 |
| 16 | 0.36 | 0.49 | 1100.6 | 515.5 | 35.07 |
| 24 | 0.78 | 0.42 | 1673.8 | 380.7 | 33.55 |
| 24 | 0.54 | 0.020 | 1139.1 | 401.3 | 35.11 |
| 24 | 0.31 | 0.75 | 1132.3 | 208.7 | 34.87 |
| 24 | 0.17 | 0.099 | 869.5 | 568.4 | 35.20 |

Table 5.3: Total streamwise median FIRST peak values per trial, Shapiro-Wilk P-value, interquartile range, and median time of FIRST peak value per trial for all multiple debris, random configurations.

| No. Debris | $\rho_f$ | P-Value | Median Peak Load [N] | IQR [N] | Median Peak Time [s] |
|---|---|---|---|---|---|
| 8 | 0.73 | 0.34 | 631.5 | 122.1 | 33.72 |
| 8 | 0.41 | 0.43 | 604.8 | 145.5 | 33.80 |
| 16 | 0.82 | 0.51 | 1357.7 | 349.3 | 33.64 |
| 16 | 0.52 | 0.19 | 973.8 | 368.2 | 33.68 |
| 16 | 0.36 | 0.20 | 751.8 | 327.5 | 33.78 |
| 24 | 0.78 | 0.22 | 1607.4 | 438.2 | 33.55 |
| 24 | 0.54 | 0.0054 | 878.0 | 471.4 | 33.62 |
| 24 | 0.31 | 0.096 | 760.0 | 477.7 | 33.61 |
| 24 | 0.17 | 0.0064 | 454.3 | 120.1 | 33.95 |

Table 5.4: Total streamwise median SECOND peak values per trial, Shapiro-Wilk P-value, interquartile range, and median time of SECOND peak value per trial for all multiple debris, random configurations.

| No. Debris | $\rho_f$ | P-Value | Median Peak Load [N] | IQR [N] | Median Peak Time [s] |
|---|---|---|---|---|---|
| 8 | 0.73 | 0.085 | 1173.9 | 456.5 | 35.94 |
| 8 | 0.41 | 0.0020 | 845.4 | 382.3 | 35.02 |
| 16 | 0.82 | 0.34 | 1457.7 | 525.5 | 35.34 |
| 16 | 0.52 | 0.94 | 1273.3 | 379.3 | 35.17 |
| 16 | 0.36 | 0.28 | 1055.3 | 325.0 | 35.28 |
| 24 | 0.78 | 0.077 | 1307.3 | 433.9 | 35.37 |
| 24 | 0.54 | 0.060 | 1002.6 | 309.4 | 35.33 |
| 24 | 0.31 | 0.64 | 1064.3 | 127.4 | 35.12 |
| 24 | 0.17 | 0.099 | 869.5 | 568.4 | 35.20 |

Using data from the regular and random configuration tests, we can understand the variation in peak values correlated with initial debris field surface density. The following plots compare median peak values to those for 10 regular and 9 random tests to create a spread of initial surface area density from 0.17 to 1.0 (structured and tightly-packed). The following also include the median peak values from the unbroken wave only.

Figure 5.6 shows the absolute maximum peak value median between trials for all 20 tests. Reaction forces are normalized by the median absolute peak streamwise reaction measured during tests with a single debris oriented longitudinally (1L). The gradient is darkest at the densest debris initial fields. Throughout all numbers of debris, there are consistently higher forces for the same number of debris for higher initial debris field density. The exceptions are cases where regular debris configurations may exceed the maximum width of less dense configurations, thus increasing the likelihood for individual debris pieces to miss the test structure. Higher initial field density lends toward a higher probability that the field remains together and impacts the structure during one distinct impact that accounts for most of the mass of the field. The pattern is reflected in the absolute maximum loading.

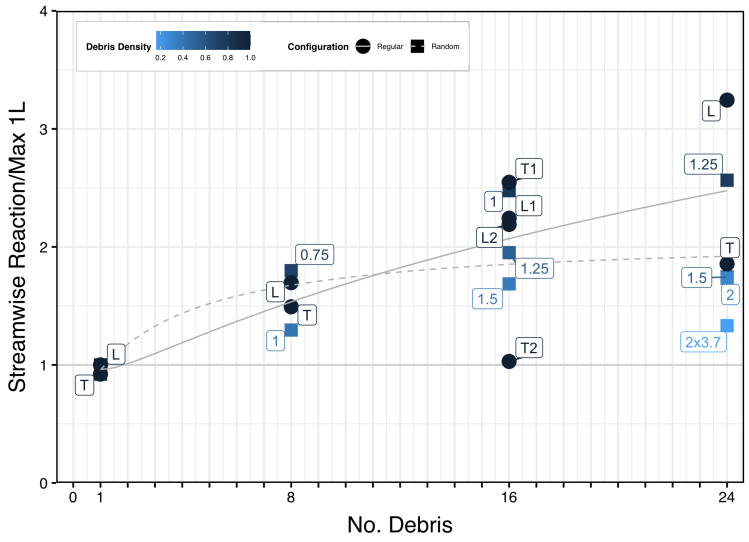


Figure 5.6: Maximum peak values for regular and random test configurations.

To understand the variation of absolute maximum values, the interquartile range of peak values per trial over the median peak value is plotted in Figure 5.7. Both trend lines tend to decrease and then remain level after single debris. Regular configurations have lower normalized interquartile ranges in general. Given the 100% density and lack of variation between trials in the regular configurations, this observation is in line with intuition. In random configurations, higher density configurations tend to have lower normalized interquartile ranges. Additionally, higher forces observed with greater number of debris may contribute to the consistent normalized interquartile ranges that do not significantly vary despite increasing number of debris.

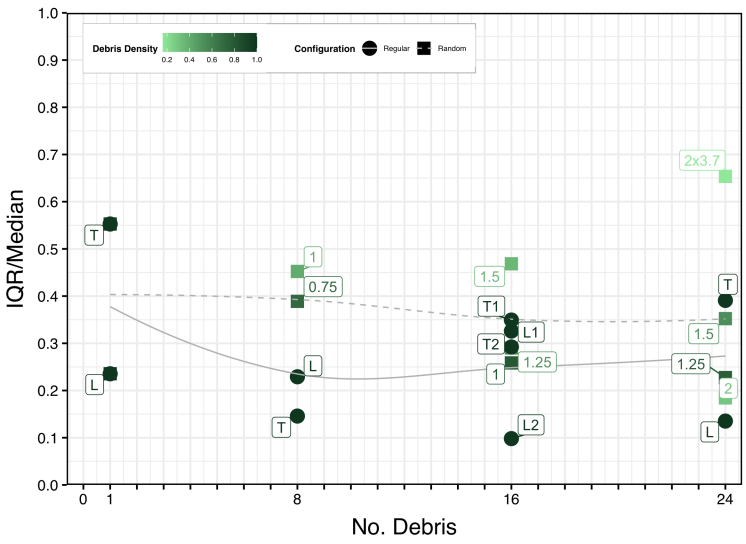


Figure 5.7: Normalized interquartile range for absolute maximum peak value for regular and random test configurations.

Figure 5.8 shows the FIRST peak medians for all 20 tests (i.e., before 34.5 seconds experiment time). Again, reaction forces are normalized by the median absolute peak streamwise reaction measured during tests with a single debris oriented longitudinally (1L). These values correlate to the first contact of debris with the test structure. During the first peak time

range, we again see higher forces for the same number of debris with greater initial field density. The largest observed force is a regular configuration with 24 debris oriented longitudinally. This configuration has all debris aligned such that all debris contact the structure and the debris field acts cohesively during the initial impact. The next highest impact force is from the next most dense configuration with 24 debris ($\rho_f = 0.78$). The least dense configurations with 24 debris have the lowest force with less than one-third of the highest impact test.

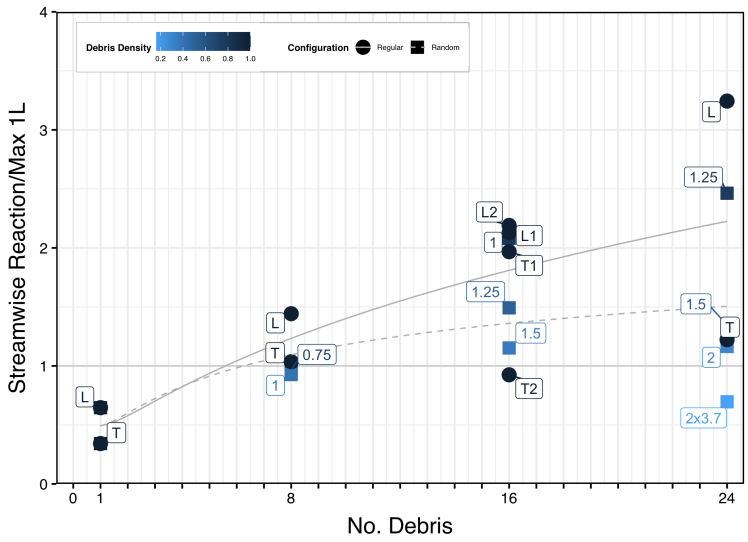


Figure 5.8: FIRST peak values for regular and random test configurations.

Normalized interquartile ranges for the FIRST peak are plotted in Figure 5.9. The first peak variation is higher for random configurations at higher numbers of debris and increases linearly to 24 debris. Regular debris configurations, conversely, level off after having a low variation at single debris trials. In general, lower debris surface area density has higher variation during the first peak. This is likely due to random configurations varying between trials and allowing different numbers of debris to be involved in one single collision, whereas regular debris configurations tend to behave cohesively through the first impact. The highest

variation is near 100% with 24 debris and $\rho_f = 0.54$. This configuration is wider than the test structure, and thus can have a variety of debris contact the box (i.e., it is likely that some trials may have most debris miss, and some have most debris collide.)

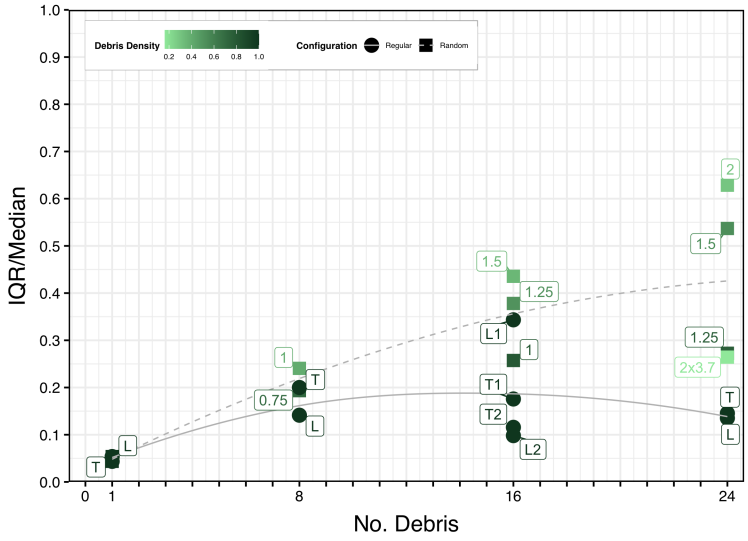


Figure 5.9: Normalized interquartile range for FIRST peak values for regular and random test configurations.

Figure 5.10 shows all median SECOND peak values (after 34.5 seconds experiment time). This is important to understand the interaction of debris with the test structure after the first contact (i.e., as debris move chaotically around and underneath the structure). In the case of the second peak, we see key observations persist. First, denser configurations tend to have higher values within the same number of debris. The highest first peak value (24L) is no longer the highest value during the second peak; this indicates the debris field breaks up and dissipates so as to not act cohesively during the second impact. However, most tests show higher second peak than first peak values.

Additionally, it is observed that the trend lines for both regular and random configurations are very similar, compared to the first peak trend lines where regular configurations

are consistently higher. Again, this is hypothesized to be due to post-impact breakup of the debris field. Once a "regular" configuration breaks up from its 100% density initial configuration, it can impact similarly to less dense configurations.

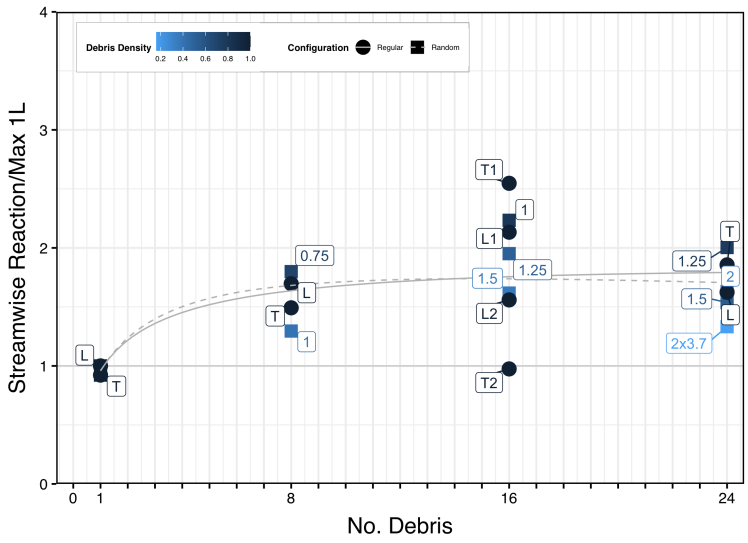


Figure 5.10: SECOND peak values for regular and random test configurations. BLUE gradient indicates initial debris field density.

Normalized interquartile range for the SECOND peak are plotted in Figure 5.11. Second peak normalized interquartile ranges show regular configurations decreasing with number of debris and leveling; random configurations decrease linearly but are generally higher for 8 and 16 debris configurations. Despite the propensity for more chaotic debris fields after an initial impact, the normalized interquartile ranges are not significantly different than those observed during the first peak.

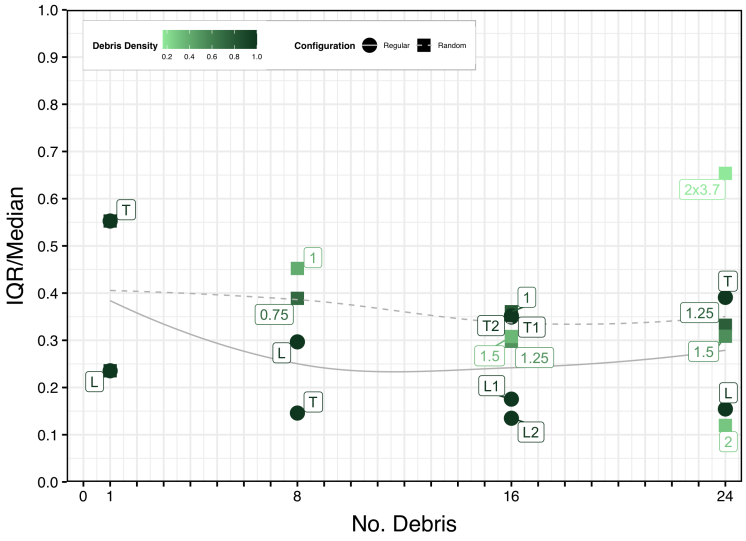


Figure 5.11: Normalized interquartile range for SECOND peak values for regular and random test configurations.

## *5.2 Damming Loads*

To understand low-frequency loading after impact, the same process of Fast Fourier Transform, filtering higher frequencies, then reconstructing time histories via inverse Fast Fourier Transform is employed (see discussion in Chapter 4).

We first discuss random configuration tests separately from regular configurations. By visual observations, time histories indicate that there are higher than solely hydrodynamic forces after the impact; this means that there are low-frequency effects due to debris damming (Shekhar et al. (2020)). Table 5.5 shows the median streamwise load values taken at 38.75 seconds experiment time. Median damming values are all higher than the unbroken wave-only load during this time frame. There is a correlation between debris field density and damming: the higher the initial field density, the higher the median damming force. There is significant interquartile range in this case, which indicates high variability between trials.

Table 5.6 shows the maximum trial damming load at 38.75 seconds. We use this value as

Table 5.5: Median damming streamwise loads per trial and interquartile range

| No. Debris | $\rho_f$ | Median Damming Load at 38.75 s [N] | IQR [N] |
|---|---|---|---|
| 8 | 0.73 | 226.3 | 66.2 |
| 8 | 0.41 | 135.5 | 49.0 |
| 16 | 0.82 | 255.0 | 83.8 |
| 16 | 0.52 | 230.4 | 46.6 |
| 16 | 0.36 | 160.1 | 37.4 |
| 24 | 0.78 | 187.7 | 132.5 |
| 24 | 0.54 | 189.0 | 80.5 |
| 24 | 0.31 | 113.9 | 40.8 |
| 24 | 0.17 | 114.2 | 109.3 |

opposed to just median peak value because the median and maximum trials are independent and valid. Due to the nondeterministic nature of damming, the maximum is considered simultaneously. The maximum damming values show the same positive correlation between initial field density and load measured. These are significant and sustained loads that appear to be influenced by how dispersed the debris field is on contact with the structure.

Table 5.6: Max damming streamwise loads per trial

| No. Debris | $\rho_f$ | Max Damming Load at 38.75 s [N] |
|---|---|---|
| 8 | 0.73 | 301.0 |
| 8 | 0.41 | 195.2 |
| 16 | 0.82 | 388.4 |
| 16 | 0.52 | 245.7 |
| 16 | 0.36 | 209.9 |
| 24 | 0.78 | 334.9 |
| 24 | 0.54 | 231.2 |
| 24 | 0.31 | 277.9 |
| 24 | 0.17 | 220.9 |

To understand the variation of damming forces across regular and random configurations,

Figure 5.12 compares the median damming forces based on debris field density. The median values found in Table 5.5 now are less the median wave reaction force at 38.75 seconds, and then are normalized by the median peak reaction force at all times measured across wave-only trials. In general, there is no significant difference between the wave-only values and single debris trials. Single debris are unlikely to get caught on the structure. Adding additional debris tends to increase the median damming force until 24 debris. In this case, it is likely that debris fields are large and dispersed enough for many debris to go around the test structure. The damming forces in 16 debris trials are more likely to fit within the front-facing area of the test structure where they are more likely to be caught and cause damming. There is a trend of increasing density indicating higher damming forces, although it is less consistent than the trends observed in peak forces.

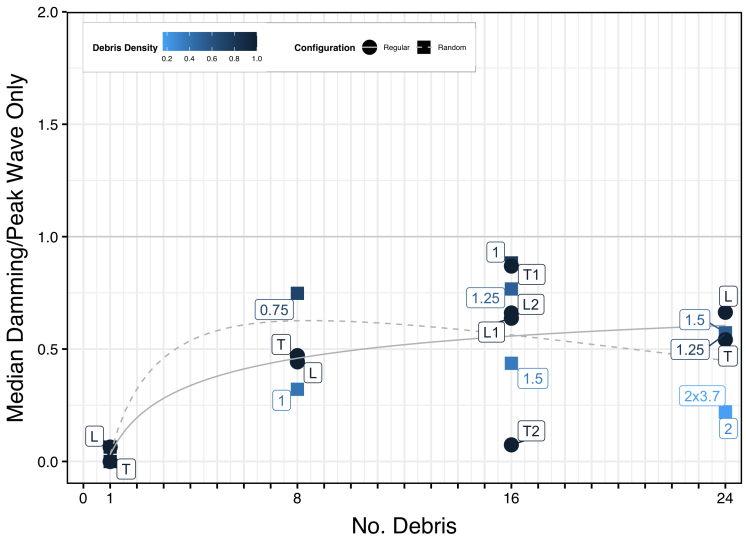


Figure 5.12: Median damming values at 38.75 s for regular and random test configurations. BLUE gradient indicates initial debris field density.

Figure 5.13 shows normalized interquartile ranges for damming. In this plot, we see very high normalized interquartile ranges and can conclude that damming is nondeterministic in

nature, particularly for large numbers of debris. During a single trial with 24 debris, it is possible that any number of debris may become caught within the legs of the test structure (which is hypothesized to cause damming). Still, trends present include decreasing normalized interquartile range with increasing number of debris in regular debris configurations, while random configurations show increasing normalized interquartile range with increasing number of debris. Overall, such a variation in normalized interquartile range during this observed phenomenon indicates that chaos tends to override trends after peak loading is observed.

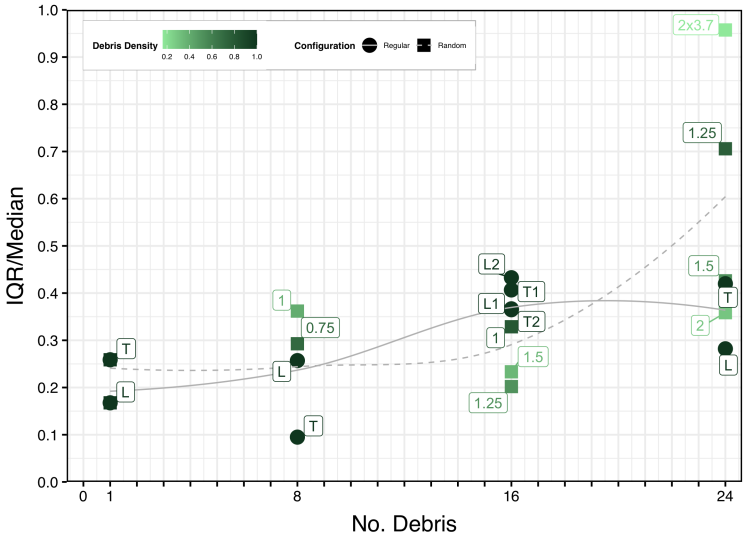


Figure 5.13: Normalized interquartile range for median damming forces.

Since there is a high degree of variation between trials, maximum values can be considered independent of the median, and are considered in Figure 5.14. The values in Table 5.6 now are less the median wave reaction force at 38.75 seconds and are normalized by the median peak reaction force at all times measured across wave-only trials. We observe a more visible trend of increasing density correlating to increased damming forces using maximum damming forces and very similar trend lines between regular and random. 16T2 generally does not follow

these trends, as many debris pieces miss the structure due to the width of the configuration. The highest damming values are found with the densest 16 debris configurations, but 24 debris also has high maximum damming forces.

The maximum damming cases likely are those in which a maximum number of debris were caught and dammed. Whether or not debris become dammed (and how many pieces per trial with multiple debris become dammed) is highly nondeterministic. In all cases with more than a single piece of debris, the damming forces should be considered as a significant forcing component of the event regardless of debris field density.

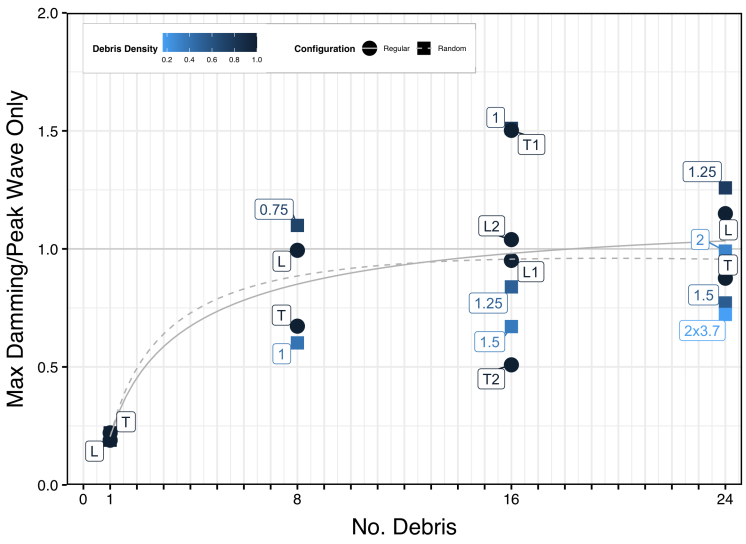


Figure 5.14: Maximum damming values at 38.75 s for regular and random test configurations. BLUE gradient indicates initial debris field density.

## *5.3 Qualitative Video Analysis*

In this section, images and video are qualitatively analyzed to hypothesize an explanation for dominant phenomena seen in streamwise time history forcing. Considering a trial for 16 debris with $\rho_f = 0.36$, one can conduct a qualitative visual analysis. Figure 5.15 shows the

time history for the selected trial.

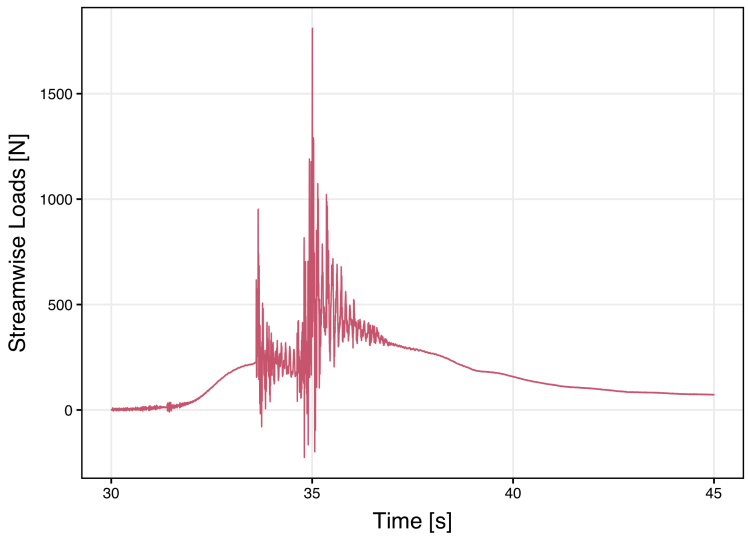


Figure 5.15: Time history for total streamwise force for a selected trial for 16 debris configuration with $\rho_f = 0.36$.

Following a similar analysis as that conducted in Chapter 4, the first impact maximum value occurs at 33.66 seconds, and the second impact maximum value at approximately 35.01. With a total separation of 1.35 seconds, the expected frames representing this segment is more than 675 (with frame rater at 500 frames per second), and represents a high-speed video separation of 22.5 seconds.

Figure 5.16 shows a series of images from video starting at the initial impact and continuing through visible debris motion. The first image shows approximately (11) of the 16 debris in this configuration in contact with each other while the downstream face of the debris field contacts the upstream face of the test structure. On the right side, one can observe three debris that will not collide head-on with the box, therefore will not be involved in the major forcing of the first collision.

Just after this initial impact, the debris shows motion in the opposite direction of flow in

which it loses contact with the box. Within approximately 0.65 seconds, the configuration of the debris has changed significantly and different debris are now upstream of the face of the debris

The last image shows debris both in contact with the front face and submerged near the legs of the test structure. The debris not in contact with the box and instead being forced around within the box wake is visible on either side of the box at 1.35 seconds after the first impact.

(a) Image at approximate time of first collision.

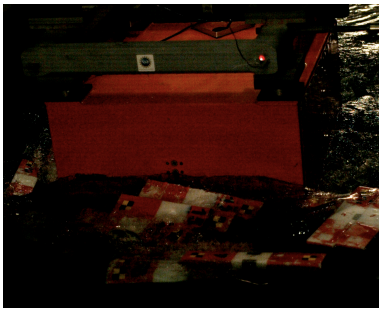

(b) Image at approximately 0.65 seconds after first collision and 0.65 seconds before second collision.

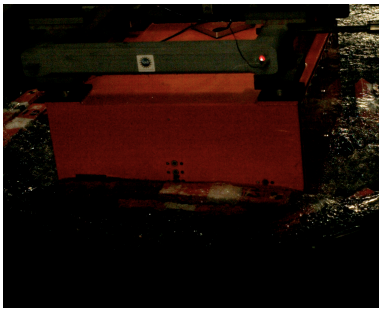

(c) Image at time of hypothesized second collision.

Figure 5.16: Images from hypothesized first and second collision times from selected trial of 16 debris configuration with $\rho_f = 0.36$.

Damming is considered to be when debris increase the force on the structure due to an increase in the area exposed to the flow, as debris may become trapped underneath the test structure within the legs of the test structure. In this case, the debris go underneath the structure, and thus no video data is available.

While the hypothesized causes of the first and second impact appear supported by qualitative data analysis, further video analysis is required to confirm causality of time history features.

# Chapter 6

# STREAMWISE REACTIONS DUE TO MULTI-SIZE DEBRIS

This chapter extends the discussion from "regular" and "random" debris configurations, in which debris are of a standard size, to configurations with debris of multiple sizes. A total of 11 tests were conducted with single pieces of debris either one-quarter or one-half the size of standard debris, or with a mix of debris sizes for larger configurations. In the cases of multiple debris, the configurations for select regular and random tests were replicated with a mix of debris sizes. The following conditions were employed during this phase: 1) unbroken wave, 2) wooden (lift) frame, 3) multi-sized debris, and 4) regular (structured) and random (unstructured) configurations.

This chapter discusses the effect of the following variables:

1. number of debris
2. debris surface area density (replicates select regular and random configurations)
3. size of individual debris

Debris size was modified by cutting standard debris into halves and quarters. Maintaining the shorter dimensions (0.102 x 0.051 m), the longest dimension is equal to 0.5 m for standard-sized debris per Figure 2.8, 0.25 m for half-sized debris, and 0.125 m for quarter-sized debris. Figure 6.1 shows all three debris sizes.

Similar to both the regular and random configurations, the outer extents of the debris field are situated with the rightmost edge 2m from the upstream face of the test structure. Regular configurations with multi-sized debris maintain the same orientation of debris axes, but with debris of multiple sizes in a space previously occupied by a standard-sized debris.

Figure 6.1: Standard, half-sized, and quarter-sized debris.

Between trials replicating random configurations, the positions of multi- and standard-sized debris are held consistent throughout all 10 trials.

For tests replicating random configurations, the debris were contained within a free-floating initial field defined similarly by the variable $\alpha$, which represents the outer dimension of the square maximum debris field extents. Using $\alpha$ and the surface area of a neutrally-buoyant debris piece, one can calculate the initial debris field density, termed $\rho_f$. All cases in the random configuration have an initial debris field density less than 100%. Multi- and standard-sized debris were all randomly placed in the initial field for each trial, but the number of each size of debris was maintained through all trials. Experimental configurations are summarized in Table 6.1 below. Note: one test does not have a specific orientation because quarter-sized debris are approximately square.

Table 6.1: List of configurations with multiple sizes of debris: number of "whole" debris, debris field extents and/or debris orientation, field density, and the number of debris of various sizes.

| # Debris | Orientation/$\alpha$ [m] | $\rho_f$ | # 1/4 Debris | # 1/2 Debris | # Full Debris |
|---|---|---|---|---|---|
| 0.25 | L/T* | 1.00 | 1 | 0 | 0 |
| 0.5 | L | 1.00 | 0 | 1 | 0 |
| 0.5 | T | 1.00 | 0 | 1 | 0 |
| 8 | T | 1.00 | 0 | 8 | 4 |
| 8 | 0.75 | 0.73 | 0 | 8 | 4 |
| 8 | 1 | 0.41 | 0 | 8 | 4 |
| 16 | 1 | 0.82 | 16 | 8 | 8 |
| 16 | 1.25 | 0.52 | 16 | 8 | 8 |
| 16 | 1.5 | 0.36 | 16 | 8 | 8 |
| 24 | 1.25 | 0.78 | 16 | 8 | 16 |
| 24 | 1.5 | 0.54 | 16 | 8 | 16 |

### *6.1 Peak Loads*

First, configurations with multiple-sized debris are discussed independently from the standard-sized debris counterparts. Figure 6.2 shows all single debris trials, in which quarter- and half-sized debris were tested. Note: certain trials for the 11 multi-sized debris tests have been removed from the following discussion due to erroneous load cell data that do not return to an approximately "zero-ed" position via setting a bound that the average value after 200 seconds could not exceed one-quarter peak unbroken wave load median in magnitude. Load cell data from these trials are assumed to be in error due to equipment malfunction. No more than four trials have been removed per test in this set.

The time histories for quarter- and half-sized debris show a similar pattern of a first and second peak. Very little low-frequency elevated forcing after the impacts (i.e., damming) is observable after the impact period. Since the debris are smaller than full-sized debris, there is a much lower likelihood of debris becoming caught within the legs of the test structure.

Note: there is a slight difference in the wave profile ahead of the peaks compared to the wave-only profile. This is assumed to be within experimental error and to not affect the rest of the time history.

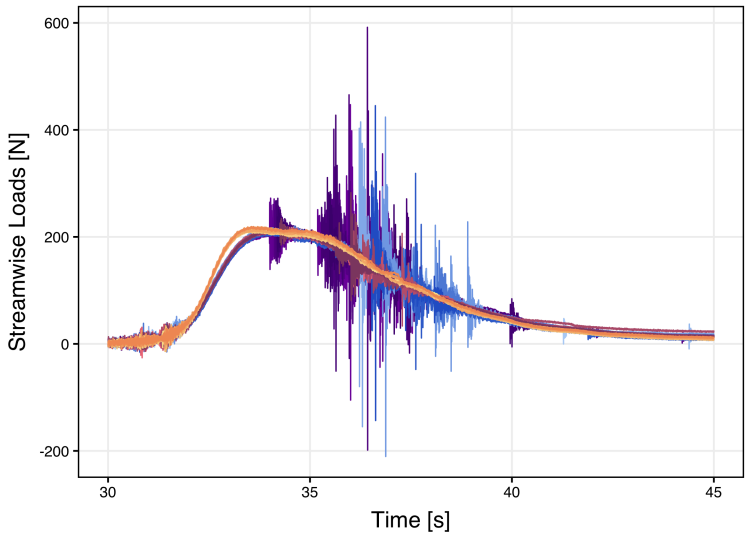


Figure 6.2: All trials of tests with single debris tests with quarter- and half-sized debris and unbroken wave-only tests. LIGHT PURPLE gradient indicates quarter-sized debris trials; BLUE gradient indicates half-sized debris oriented longitudinally; DARK PURPLE indicates half-debris oriented transversely; ORANGE gradient indicates unbroken wave-only trials.

Figure 6.3 shows unfiltered time histories for trials with multi-sized debris equating to 8 standard-sized debris. The first and second peaks are evident in all configurations. Visual observation yields similar peak magnitudes and variation among trials. Low-frequency damming loads are visible after the impacts. This is similar to counterparts with standard-sized debris.

Figure 6.4 shows unfiltered time histories for all 16 debris-equivalent trials. While the same first and second peak pattern is observed, we note the presence of peaks beginning much earlier in the trial time history for a trial with $\rho_f = 0.52$. This is likely due to a small

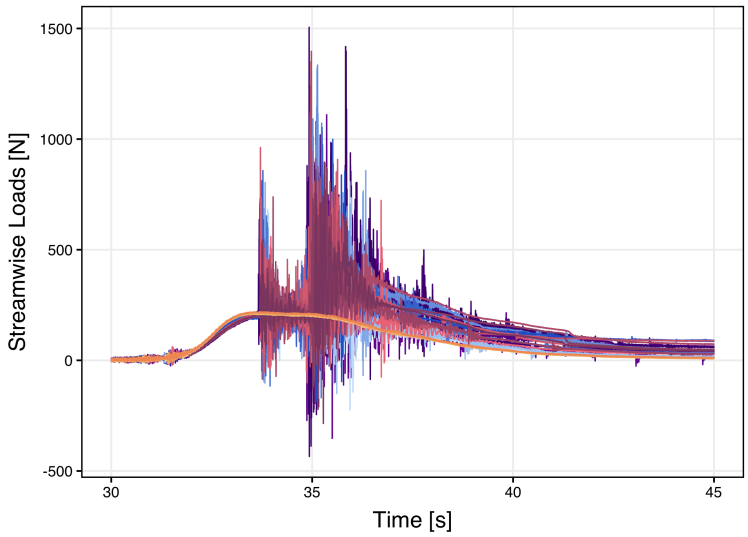


Figure 6.3: All trials with multiple-sized debris equating to 8 full-size debris and wave-only trials. LIGHT PURPLE gradient indicates 8 debris-equivalent with $\rho_f = 0.41$; BLUE gradient indicates 8 debris-equivalent with $\rho_f = 0.73$; DARK PURPLE indicates 8 debris-equivalent in regular configuration oriented transversely to the direction of flow; ORANGE gradient indicates unbroken wave-only trials.

debris with higher velocity due to the flow at the front of the debris field; the overall profile and analysis are not impacted by this occurrence, but it warrants further investigation in future scopes of work. Largely, it speaks to the nondeterministic nature of trials.

Figure 6.5 shows unfiltered time histories for all 24 debris-equivalent trials. The same first and second peaks are visible. Damming forcing is apparent after the impact region. Uniquely, the higher density configuration shows at least one trial with a high first peak compared to subsequent peaks.

Figure 6.6 shows a selected, example trial with the equivalent of 8 standard debris comprised of multi-sized debris oriented transversely to the direction of flow for reference.

Table 6.2 summarizes the statistics related to the total streamwise absolute maximum

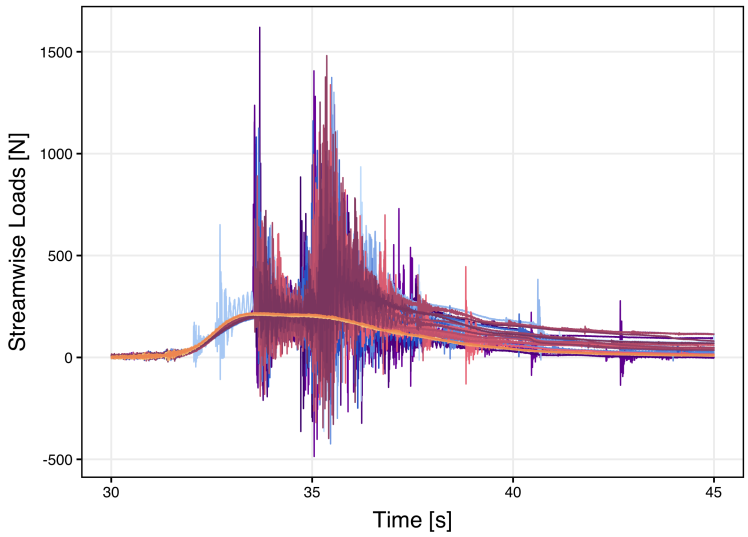


Figure 6.4: All trials with multiple-sized debris equating to 16 full-size debris and wave-only trials. LIGHT PURPLE gradient indicates 16 debris-equivalent with $\rho_f = 0.36$; BLUE gradient indicates 16 debris-equivalent with $\rho_f = 0.52$; DARK PURPLE indicates 16 debris-equivalent with $\rho_f = 0.82$; ORANGE gradient indicates unbroken wave-only trials.

peaks for all multi-sized debris configurations tested with the unbroken wave, wooden (lift) frame, and standard- sized debris. Shapiro-Wilk tests are applied to all tests and reported (further statistical discussion is found in Chapter 4). P-value above 0.05 indicates the distribution can be assumed normal; while some P-values are under this value, observation of QQ-plots (see Appendix C) indicates approximate linearity. In all cases, a median value is taken. Tables 6.3 and 6.4 follow a similar process for the maximum values before 34.5 seconds experiment time (i.e., FIRST peak values) and after 34.5 seconds (i.e., SECOND peak), respectively.

Most median times of peak values per trial from the median absolute maximum load occur after 34.5 seconds. The densest 24 debris-equivalent trials are an exception, with their median peak value time before 34.5 seconds. This pattern is the same as observed with

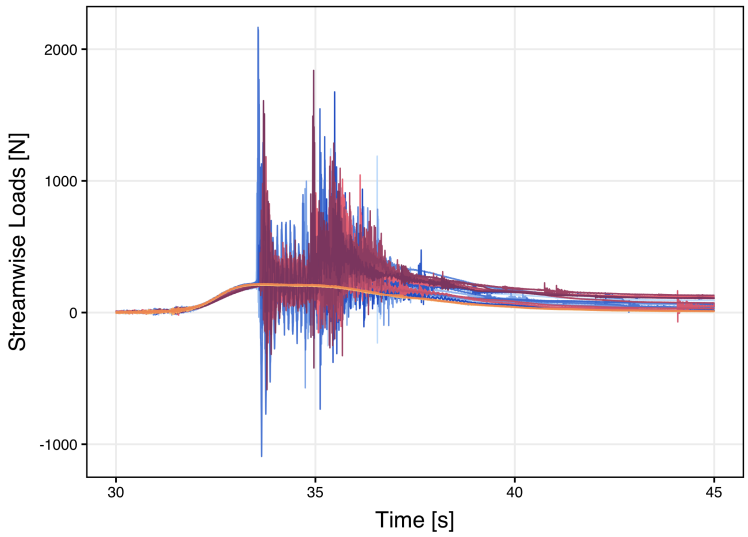


Figure 6.5: All trials with multiple-sized debris equating to 24 full-size debris and wave-only trials. PURPLE gradient indicates 24 debris-equivalent with $\rho_f = 0.54$; BLUE gradient indicates 24 debris-equivalent with $\rho_f = 0.78$; ORANGE gradient indicates unbroken wave-only trials.

equivalent random configurations with only standard-sized debris.

During the first peak, the largest median peak load values are observed in the densest configurations with 24 debris. The majority of values are not the absolute maximum values. There is a large spread for most of the configurations, with larger interquartile ranges generally found for less dense configurations and more debris. In particular, the highest value load for 24 debris with $\rho_f = 0.78$ also has the highest interquartile range. This is similar to equivalent random debris configurations with standard-sized debris only. We note very small interquartile range values for the first peak for the smallest pieces of debris (i.e., quarter- and half-sized).

Second peak values are generally higher than their first peak counterparts. Additionally, the interquartile range tends to be lower during the second peak. Despite the time histories

Figure 6.6: Selected trial with equivalent of 8 full-sized debris using multi-sized debris.

Table 6.2: Total streamwise median maximum peak values per trial, Shapiro-Wilk P-value, interquartile range, and median time of absolute max peak value per trial for all multiple debris, random configurations.

| Debris | Orient./$\alpha$ | $\rho_f$ | P-Value | Med. Peak Load [N] | IQR [N] | Med. Peak Time [s] |
|---|---|---|---|---|---|---|
| 0.25 | L/T* | 1.00 | 4.2e-05 | 216.3 | 2.6 | 34.55 |
| 0.5 | L | 1.00 | 0.029 | 307.6 | 135.2 | 35.81 |
| 0.5 | T | 1.00 | 0.051 | 289.8 | 172.3 | 36.25 |
| 8 | T | 1.00 | 0.33 | 1019.0 | 215.4 | 35.04 |
| 8 | 0.75 | 0.73 | 0.025 | 859.9 | 141.9 | 35.25 |
| 8 | 1 | 0.41 | 0.024 | 876.1 | 88.9 | 35.31 |
| 16 | 1 | 0.82 | 0.97 | 1619.9 | 283.9 | 35.18 |
| 16 | 1.25 | 0.52 | 0.88 | 1373.8 | 188.0 | 35.39 |
| 16 | 1.5 | 0.36 | 0.16 | 1481.1 | 207.1 | 35.35 |
| 24 | 1.25 | 0.78 | 0.13 | 2166.1 | 453.0 | 33.65 |
| 24 | 1.5 | 0.54 | 0.12 | 1838.8 | 222.7 | 35.35 |

Table 6.3: Total streamwise median FIRST peak values per trial, Shapiro-Wilk P-value, interquartile range, and median time of FIRST peak value per trial for all multiple debris, random configurations.

| Debris | Orient./$\alpha$ | $\rho_f$ | P-Value | Med. Peak Load [N] | IQR [N] | Med. Peak Time [s] |
|---|---|---|---|---|---|---|
| 0.25 | L/T* | 1.00 | 0.0076 | 215.3 | 3.5 | 34.20 |
| 0.5 | L | 1.00 | 0.13 | 258.9 | 17.8 | 34.20 |
| 0.5 | T | 1.00 | 0.56 | 213.4 | 4.2 | 34.19 |
| 8 | T | 1.00 | 0.76 | 654.1 | 100.4 | 33.72 |
| 8 | 0.75 | 0.73 | 0.76 | 652.9 | 193.6 | 33.83 |
| 8 | 1 | 0.41 | 0.24 | 545.7 | 182.9 | 33.95 |
| 16 | 1 | 0.82 | 0.10 | 833.9 | 374.3 | 33.66 |
| 16 | 1.25 | 0.52 | 0.0056 | 643.1 | 124.6 | 33.72 |
| 16 | 1.5 | 0.36 | 0.73 | 623.0 | 170.4 | 33.88 |
| 24 | 1.25 | 0.78 | 0.017 | 1059.1 | 290.7 | 33.65 |
| 24 | 1.5 | 0.54 | 0.29 | 826.3 | 281.6 | 33.72 |

showing variation between trials, most trials have similar maximum value locations and show relatively low ranges in peak values during this time period.

Table 6.4: Total streamwise median SECOND peak values per trial, Shapiro-Wilk P-value, interquartile range, and median time of SECOND peak value per trial for all multiple debris, random configurations.

| Debris | Orient./$\alpha$ | $\rho_f$ | P-Value | Med. Peak Load [N] | IQR [N] | Med. Peak Time [s] |
|---|---|---|---|---|---|---|
| 0.25 | L/T* | 1.00 | 4.9e-05 | 215.4 | 3.0 | 34.63 |
| 0.5 | L | 1.00 | 0.040 | 307.6 | 136.2 | 35.88 |
| 0.5 | T | 1.00 | 0.52 | 289.8 | 172.3 | 35.44 |
| 8 | T | 1.00 | 0.33 | 1019.0 | 215.5 | 35.04 |
| 8 | 0.75 | 0.73 | 0.025 | 859.9 | 141.9 | 35.25 |
| 8 | 1 | 0.41 | 0.0071 | 876.1 | 62.1 | 35.36 |
| 16 | 1 | 0.82 | 0.90 | 970.7 | 402.9 | 35.42 |
| 16 | 1.25 | 0.52 | 0.61 | 966.0 | 486.1 | 35.54 |
| 16 | 1.5 | 0.36 | 0.16 | 1099.9 | 207.1 | 35.35 |
| 24 | 1.25 | 0.78 | 0.24 | 1010.1 | 301.4 | 35.28 |
| 24 | 1.5 | 0.54 | 0.18 | 1095.9 | 4 278.6 | 35.42 |

Using median peak values for both the absolute maximum, first, and second peaks for tests with multi-sized debris and their standard-sized debris counterparts, we can understand the effect of a variety of debris sizes. Since the same surface area is covered in the initial debris field, the major difference is the mass distribution. In multi-sized debris, the mass of the debris field is stored in smaller debris, which may affect impact loading.

Figure 6.7 shows the absolute maximum peak values plotted according to number of debris, whether or not the debris field has debris of multiple sizes, and debris field density (plotted with gradient). Values are normalized by the median absolute peak value for a single standard-sized debris oriented longitudinally (discussed in Chapter 4). All 11 multi-sized debris tests and 8 regular and random debris equivalents are plotted. First, we observe that quarter- and half-sized debris, regardless of orientation, have absolute maximum peak load values lower than single, standard debris trials. Their individual impacts are within 50 N of the absolute maximum wave-only peak value. In general, equivalent configurations

with standard-sized debris have higher median values. However, the 24 debris trials with $\rho_f = 0.54$ are approximately equivalent maximum values. This pattern is seen with trend lines for standard-sized debris being a similar shape to the multi-sized debris, but with higher values.

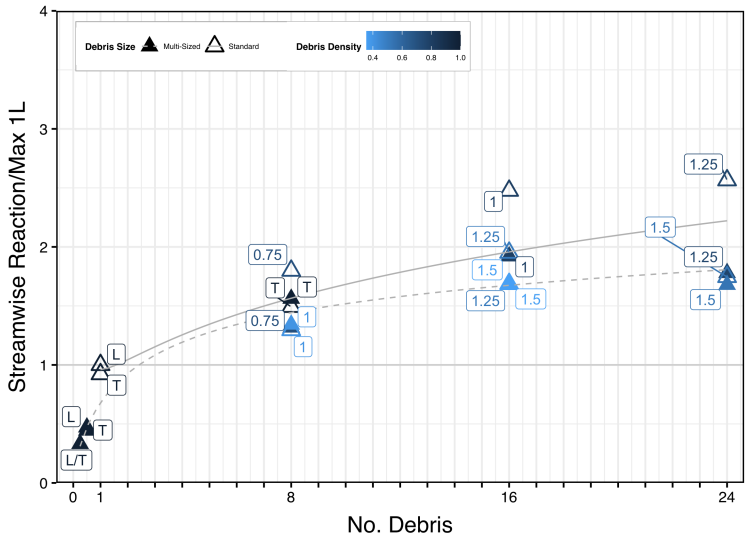


Figure 6.7: Maximum peak values for multi-sized debris test configurations and standard-sized debris equivalents.

Variation between trials is quantified using normalized interquartile range (i.e., percent of the range absolute peak values per trial divided by the median), and is shown in Figure 6.8. Normalized interquartile ranges are highest for single standard- and half-sized debris and 24 debris. Generally, higher density fields have lower normalized interquartile ranges within the equivalent debris numbers. The normalized interquartile range trend lines are of similar shape. The quarter-sized debris shows a small normalized interquartile range for the absolute maximum peak values comparatively, which pulls the trend line down near the smaller numbers of debris for multi-sized fields. Excluding that point yields very similar trend lines, by inspection. Thus, individual debris size variation does not necessarily increase

variation and randomness between trials according to the normalized interquartile range metric.

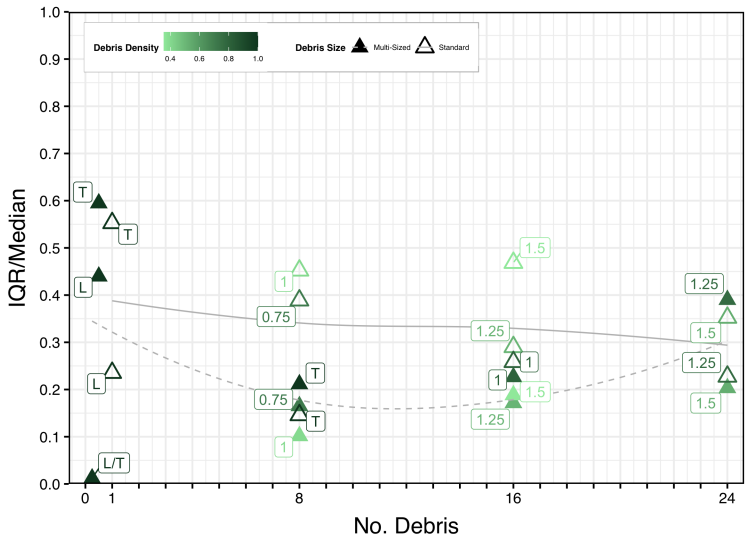


Figure 6.8: Normalized interquartile range for absolute maximum peak value for multi-sized debris test configurations and standard-sized debris equivalents.

Figure 6.9 shows the FIRST peak medians (i.e., before 34.5 seconds experiment time) plotted according to number of debris, whether or not the debris field has debris of multiple sizes, and debris field density (plotted with gradient). Values are again normalized by the median absolute peak value for a single standard-sized debris oriented longitudinally (discussed in Chapter 4). All 11 multi-sized debris tests and 8 regular and random debris equivalents are plotted. For single debris of any size, the first peak value is clustered near the wave value. At 8 debris, multi- and standard-sized fields are also tightly packed (i.e., first peak values are similar regardless of debris density or individual debris sizes). At higher numbers of debris, standard-sized debris tend to have higher first peak values for similar configurations.

Normalized interquartile ranges for FIRST peak values are shown in Figure 6.10. Nor-

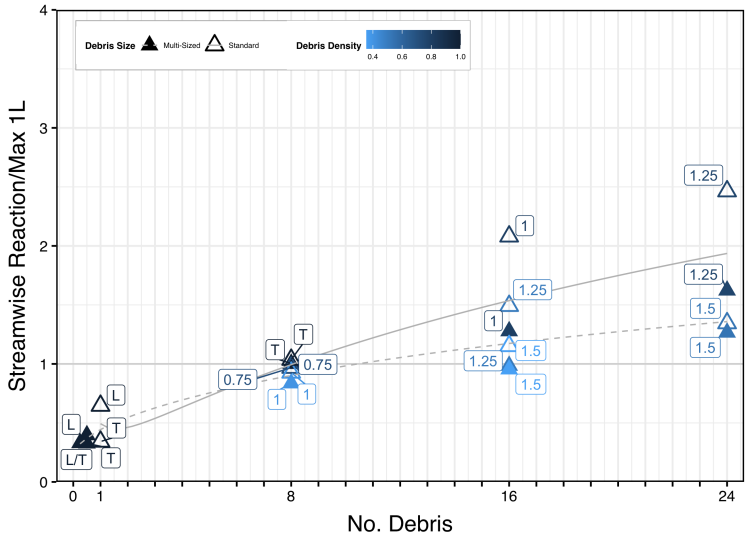


Figure 6.9: Maximum FIRST peak values for multi-sized debris test configurations and standard-sized debris equivalents.

malized interquartile ranges show an increase with number of debris regardless of individual debris size or field density. In general, the highest normalized interquartile ranges per number of debris are seen with the least dense configurations. This makes sense, as larger debris fields may exceed the width of the face of the test structure; therefore, during the first impact, debris may miss the structure or may hit the structure, and thus is nondeterministic. There is not a strong correlation between normalized interquartile range and standard- vs. multi-sized debris.

Figure 6.11 shows the normalized SECOND peak medians (i.e., after 34.5 seconds experiment time) plotted according to number of debris, whether or not the debris field has debris of multiple sizes, and debris field density (plotted with gradient). All 11 multi-sized debris tests and 8 regular and random debris equivalents are plotted. Second peak values show similar trend lines for standard- and multi-sized debris. Higher density fields tend to be higher than lower density fields. While standard-sized fields tend to have higher values,

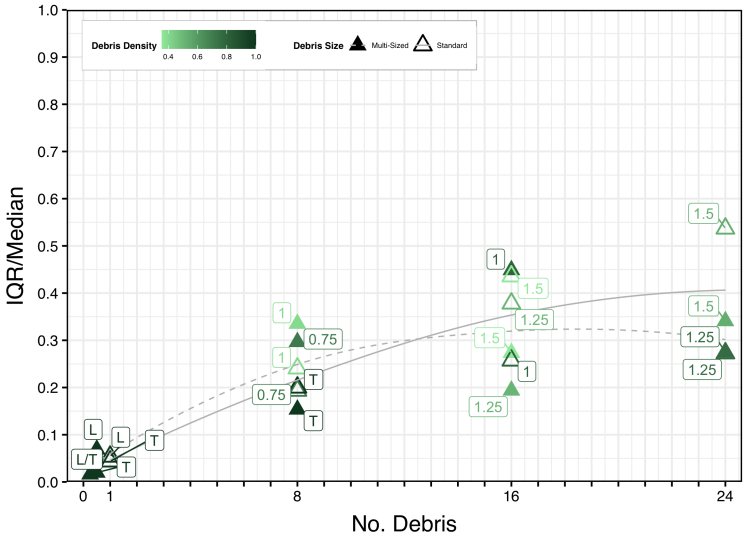


Figure 6.10: Normalized interquartile range for FIRST peak value for multi-sized debris test configurations and standard-sized debris equivalents.

the margin of differentiation is small. We note that quarter- and half-sized debris are not significantly different in the second peak loads than the wave only. However, most debris other than the densest 24 debris trials show higher second peak values than first peak.

Figure 6.12 shows normalized interquartile ranges for SECOND peak values. All 11 multi-sized debris trials and 8 standard-sized debris equivalents are shown. Similar to absolute maximum normalized interquartile ranges, second peak percent ranges are highest for single standard- and half-sized debris and 24 debris. Generally, higher density field have lower normalized interquartile ranges within the equivalent debris numbers. The normalized interquartile range trend lines are of similar shape. The quarter-sized debris pulls the trend line down near the smaller numbers of debris for multi-sized fields. Excluding that point yields very similar trend lines; thus, individual debris size variation does not necessarily increase variation and randomness between trials.

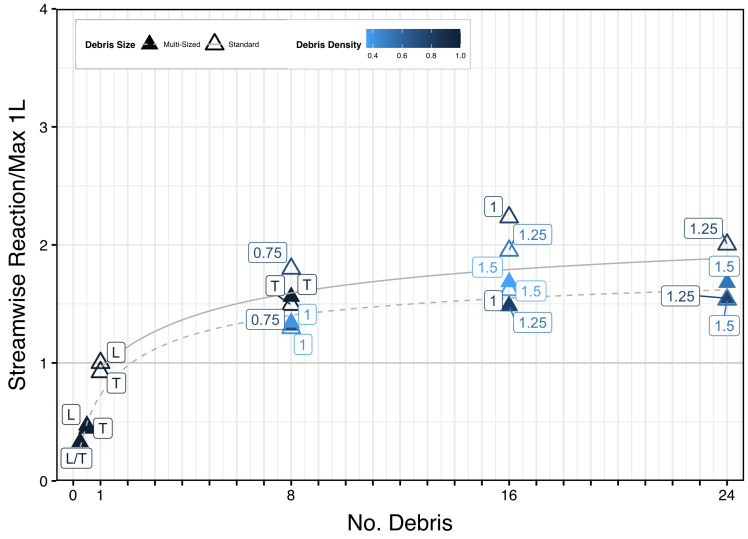


Figure 6.11: Maximum SECOND peak values for multi-sized debris test configurations and standard-sized debris equivalents.

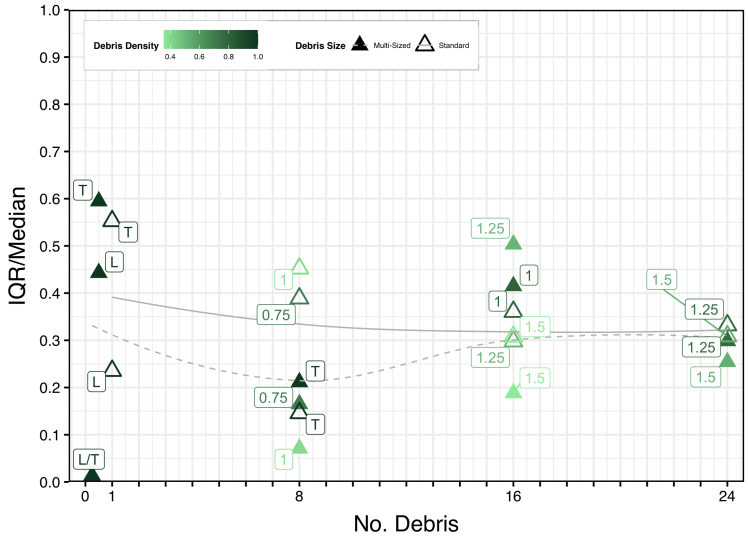


Figure 6.12: Normalized interquartile range for absolute maximum peak value for multi-sized debris test configurations and standard-sized debris equivalents.

## *6.2 Damming Loads*

Low-frequency forcing after the peak loading is compared between multi-sized debris tests and standard-sized equivalents using FFT analysis, which is described in Chapter 4. Multi-sized debris configurations' median damming values are shown in Table 6.5. Unlike their regular counterparts, the higher density fields do not necessarily have higher damming forces. This may be in part due to the nondeterministic aspect of damming (i.e., the median represents one of many possible outcomes). There is also significant interquartile range for 8 debris or more.

Table 6.5: Median damming streamwise loads per trial and interquartile range

| # Full Debris | Orientation/$\alpha$ | $\rho_f$ | Median Damming Load at 38.75 s [N] | IQR [N] |
|---|---|---|---|---|
| 0.25 | L/T* | 1.00 | 71.4 | 13.6 |
| 0.5 | L | 1.00 | 70.7 | 19.6 |
| 0.5 | T | 1.00 | 71.0 | 24.5 |
| 8 | T | 1.00 | 171.5 | 56.3 |
| 8 | 0.75 | 0.73 | 152.3 | 71.8 |
| 8 | 1 | 0.41 | 161.8 | 70.1 |
| 16 | 1 | 0.82 | 96.8 | 140 |
| 16 | 1.25 | 0.52 | 137.6 | 119 |
| 16 | 1.5 | 0.36 | 131.1 | 95.9 |
| 24 | 1.25 | 0.78 | 114.0 | 133 |
| 24 | 1.5 | 0.54 | 185.8 | 61.3 |

Addressing the nondeterministic nature of damming forces, Table 6.6 looks at maximum damming forces for all multi-sized debris tests. Maximum values are significantly higher than median values for all trials with more than half- or quarter-sized singular debris. This makes sense, since all trials with many debris have possible outcomes in which standard-sized debris, especially, may become caught in the legs of the test structure.

Figure 6.13 sheds more light on the values above, as it plots the multi-sized tests along with standard-sized equivalents for median damming forces. Values are normalized by taking

Table 6.6: Maximum damming streamwise loads per trial.

| # Full Debris | Orientation/$\alpha$ | $\rho_f$ | Max Damming Load at 38.75 s [N] |
|---|---|---|---|
| 0.25 | L/T* | 1.00 | 75.8 |
| 0.5 | L | 1.00 | 79.5 |
| 0.5 | T | 1.00 | 75.8 |
| 8 | T | 1.00 | 190.4 |
| 8 | 0.75 | 0.73 | 189.6 |
| 8 | 1 | 0.41 | 213.6 |
| 16 | 1 | 0.82 | 184.2 |
| 16 | 1.25 | 0.52 | 229.9 |
| 16 | 1.5 | 0.36 | 212.1 |
| 24 | 1.25 | 0.78 | 235.3 |
| 24 | 1.5 | 0.54 | 224.1 |

the median reaction forces measured at 38.75 seconds, subtracting the median wave-only reaction force at that time, and then dividing by the median peak wave-only reaction force at all times throughout all trials. Median damming values are very small for all single debris, regardless of size, and are comparable to the wave-only load at this time. In general, the median values at higher number of debris are lower than their standard-sized counterparts, but with a few exceptions. The trend line for multi-sized debris configurations tends to decrease with higher number of debris. Since these configurations have the same mass and surface area but with a smaller number individual of debris, damming forces are likely to be decreased since smaller individual debris are less likely to become caught in the test structure legs. In 24 debris trials, there are 16 individual quarter-sized pieces. While they may remain cohesive and/or contribute to forcing during impact loading, they are too small to cause sustained increases in hydrostatic forces since they can flow through the legs of the structure without catching.

Figure 6.14 shows normalized interquartile ranges for damming forces for multi-sized debris and standard-sized equivalents. Given the very low normalized interquartile ranges for

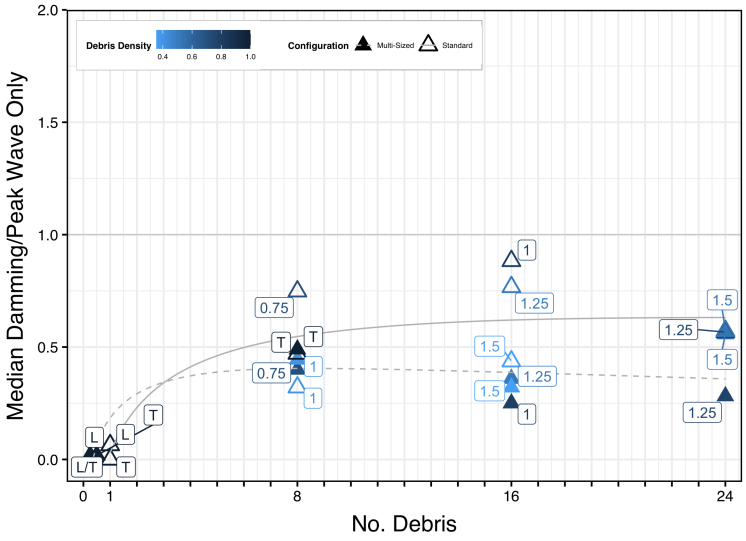


Figure 6.13: Median damming values at 38.75 s for multi-sized debris configurations and standard-sized debris equivalents.

quarter- and half-sized debris, the trend line starts low for multi-sized debris. Also, the normalized interquartile range tends to decrease for higher number of debris for multi-sized debris, but increases steadily for standard-sized debris. There is not a clear correlation between debris density and normalized interquartile ranges. The highest normalized interquartile range, however, is well over 100% and is a dense multi-sized debris test with 16 debris equivalent.

The high normalized interquartile ranges, again, warrant discussion of maximum damming loads. Figure 6.15 shows the maximum for all multi- and standard-sized equivalents. Values are normalized (similar to median damming forces) by taking the maximum reaction forces measured at 38.75 seconds, subtracting the median wave-only reaction force at that time, then dividing by the median peak wave-only reaction force at all times throughout all trials. With maximum damming forces, there is a steady increase in damming force that tapers off with number of debris for both multi- and standard-sized. The multi-sized trend

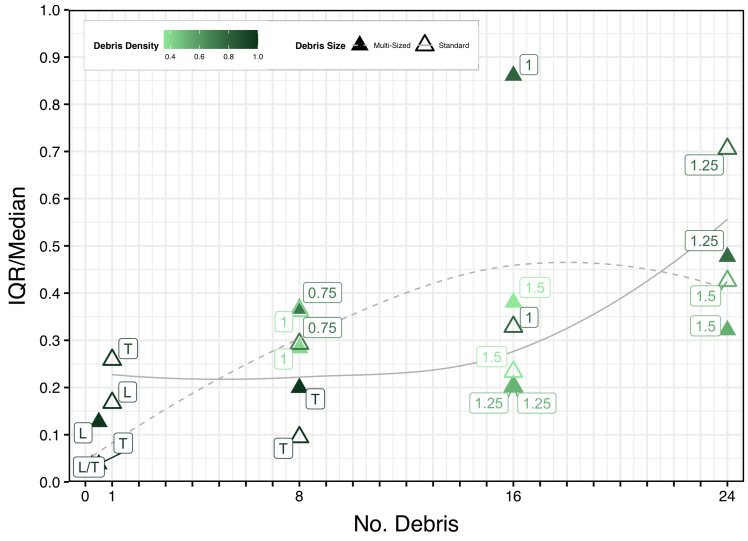


Figure 6.14: Normalized interquartile range damming values at 38.75 s for multi-sized debris configurations and standard-sized debris equivalents.

is lower than the standard-sized trend line. This makes sense, since similar configurations but comprised of smaller debris have less propensity to become caught in the test structure legs, since smaller pieces are more likely to flow through.

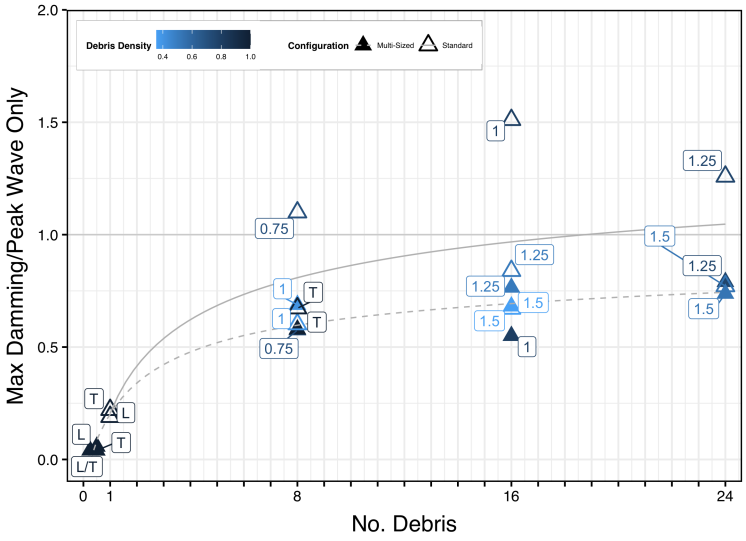


Figure 6.15: Maximum damming values at 38.75 s for multi-sized debris configurations and standard-sized debris equivalents.

### *6.3 Qualitative Video Analysis*

As performed in Chapters 4 and 5, qualitative video analysis is performed to hypothesize an explanation for dominant phenomena seen in streamwise time history forcing. High-speed camera footage is taken at 500 frames per second. A trial for 16 full-size debris equivalent and $\rho_f = 0.82$ is shown in Figure 6.16. In this configuration, 8 debris are full-sized, 8 are half-sized, and 16 are quarter-sized.

In this trial, the first peak maximum occurs at 33.57 seconds. The second peak maximum occurs at 35.50 seconds. The images shown in Figure 6.17 show the progression from the first impact until 1.63 seconds after due to video length; this is 0.3 seconds short of the 1.93 second time range from first peak maximum to the second peak maximum, but is still indicative of the events.

The first image shows a random configuration with varying debris sizes at the time of the initial contact with the test structure. The debris field is dense and debris impacts

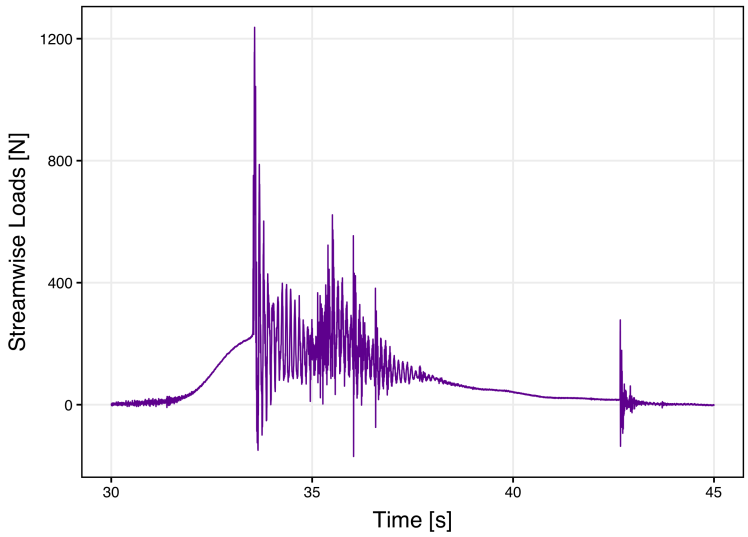


Figure 6.16: Time history for total streamwise force for a selected trial for 16 debris-equivalent configuration with $\rho_f = 0.82$.

largely as a cohesive field, which likely influences the high first peak seen in the time history. 0.97 seconds later, we see the debris no longer in contact with the box, but breaking up and beginning to move around the test structure and/or upstream of the test structure face. This is consistent with an upstream motion seen in both Chapters 4 and 5, which is hypothesized to be the break between the first and second peak phenomena.

Though the video cuts off before the time of maximum second peak value, the image 0.30 seconds before that time shows debris nearly in contact with the front face, debris in the vicinity of test structure legs, and debris that has been pushed around the test structure. In this instance, the variability of debris impact occurrences and times may influence the lower second peak value.

We note that the hypothesis of causality for peak values requires further video analysis to fully establish and is outside of the scope of this work.

(a) Image at approximate time of first collision.

(b) Image at approximately 0.97 seconds after first collision.

(c) Image at 0.30 seconds before hypothesized second collision (cut-off due to video availability).

Figure 6.17: Images from hypothesized first and second collision times from a selected trial for 16 debris-equivalent configuration with $\rho_f = 0.82$.

# Chapter 7
# DISCUSSION OF MEASURED REACTIONS

In this section, all tests within the scope of this work are discussed. Trends are identified across the four axes of variability discussed in Chapters 4 through 6, which include: a) number of debris, b) debris orientation, c) initial debris field surface area density, and d) individual debris sizes.

As discussed in preceding chapters, each set of tests varied either items b), c), or d). In addition, each set varied a): the number of debris in the debris field. Discussing all 30 tests and nearly 300 trials enables understanding of the effect of the initial debris field on measured reaction forces, which may be extended to understand patterns in otherwise nondeterministic debris motion and impact with a structure. The effects of variations in initial debris field maximum measured reactions (i.e., peak forces) and damming reaction forces in Sections 7.1 and 7.2, respectively.

## *7.1 Peak Forces*

### *7.1.1 Effect of Single Debris Pieces*

As discussed in Chapter 4, peak forces are found by taking the maximum measured reaction forces in all trials for a single test, then taking the median of trial maximums. The median value is then normalized by the median peak value for a single debris oriented longitudinally (labeled "1L"). For single-debris tests, we hypothesize that impacts are proportional to the mass of an individual debris piece and respond elastically to collision with the test structure. Figure 7.1 shows the single debris trials conducted for debris of varying lengths. Note: the mass of each debris scales approximately proportionally to its length, where a full-sized debris has a mass of 2.52 kg.

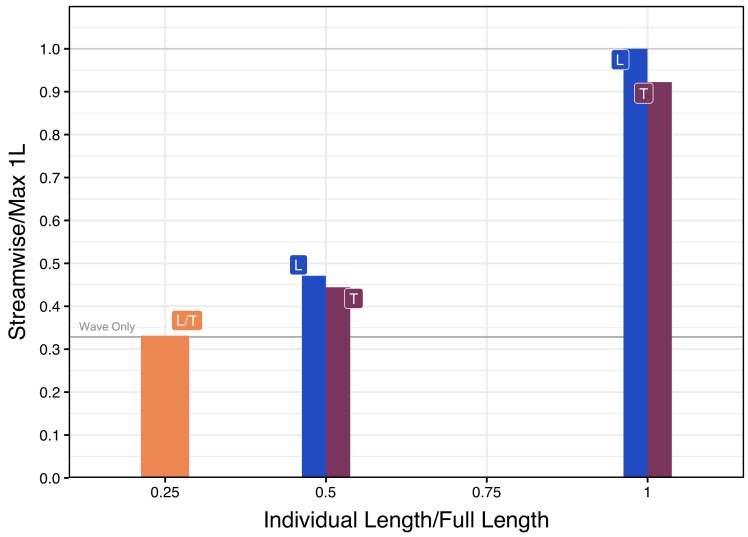


Figure 7.1: Median absolute maximum peak values for single-debris tests.

Single-debris tests have a clear scaling with the size of individual debris. The largest single-debris test is the normalization factor: a single-debris oriented longitudinally. For both half-sized and full-sized single debris, the longitudinal orientation has a slightly higher peak value than the transverse orientation. This is hypothesized to be due to slowing prior to impact with the face of the test structure, but ultimately does not result in large force discrepancies between the two orientations.

For quarter-sized debris, the longitudinal and transverse dimensions were approximately equal, therefore the individual trials cannot be categorized as either longitudinal or transverse (i.e., the orientation was approximately equivalent regardless of the orientation of debris axes). Quarter-sized debris have the smallest single debris reaction force, and barely exceed the maximum reaction force incurred by tests with the wave only. To illustrate this, the dark gray line indicated as "Wave Only" in Figure 7.1 shows the normalized wave-only test median peak value. The quarter-sized debris trial is not significantly different than the peak force imparted by the wave without debris. This indicates that the single debris made minimal

impact and is small and light enough to act as a particle with flow motion instead of causing an elastic collision with the test structure.

In addition to the median peak forces, Figure 7.2 shows the interquartile range normalized by the median for each test as a measure of variability for all single-debris trials. One can observe that for quarter-debris trials, the normalized interquartile range is negligible. This indicates very little variation between trials, which is consistent with the hypothesis that it acts like a flow particle and thus has low variation similar to the wave-only trials (discussed in Chapter 3).

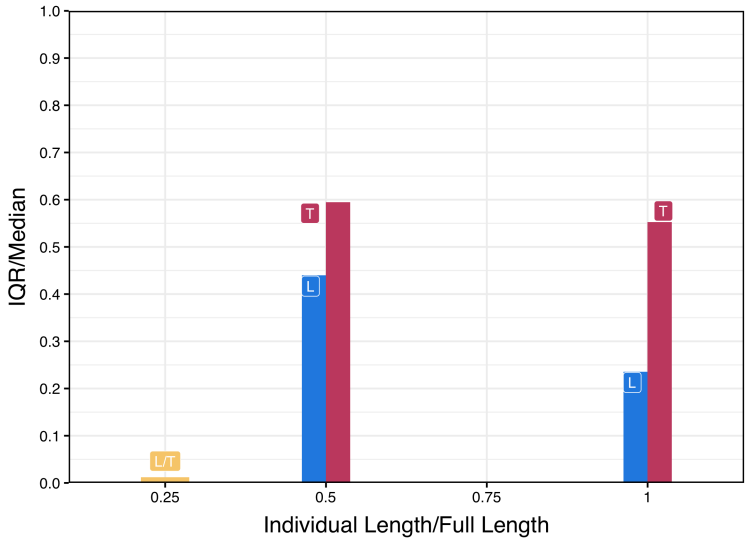


Figure 7.2: Normalized interquartile range for maximum peak values for single-debris tests.

The largest variability is seen with transverse orientations for either half- or full-sized debris. Conversely, the largest force (full-sized debris oriented longitudinally) has the lowest variability. This indicates that orientation impacts the variability and forcing seen as a result of a single-debris impact. Higher variability is likely due to the addition of drag and possible rotation of the debris before impact. Since the debris is oriented with its longest dimension perpendicular to the flow, there is increased drag and thus a higher likelihood of rotation

before impact (i.e., the debris may hit first with a corner). In the case of longitudinal single debris impacts, we see the variability is decreased. In these cases, the orientation of the debris reduces drag and thus the possibility of different impact angles.

It should be considered that maximum peak values discussed here may come from either the first or second impact. After the first impact, it is hypothesized that second peak reaction forces are due to chaotic impacts in which orientation may change from the initial debris configuration. However, both processes are chaotic in nature and thus vary between trials, yielding higher normalized interquartile ranges.

### *7.1.2 Effect of Number of Debris*

The effect of the number of debris on reaction forces is considered a key finding of this study. While it follows logically that larger debris fields with more individual debris pieces have more mass and higher impact forces, this section discusses trends throughout all tests within this scope and their median peak reaction forces normalized by single debris oriented longitudinally median peak value (i.e., "1L"). Figure 7.3 plots all normalized median peak reaction forces.

The trend lines for all three test types are shown. For debris fields with "regular" configurations, the trend line is shown to increase approximately linearly with number of debris. The highest peak value (24 debris oriented longitudinally), however, is only 3.25 times the single debris normalization factor (1L), which indicates that the impact forces are not solely a function of increasing debris field mass. We also note that, as seen with single debris, the effect of individual debris orientation yields higher forces in longitudinal configurations with the same number of debris than in transverse counterparts. This is likely due in part to drag caused by wider, transverse debris fields, as well as drag on individual debris themselves. One exception is the test 16T1, in which the impacting cross-sectional area is comparable to 16L1.

"Random" configurations show an approximately logarithmic trend line, which shows nearly constant reaction forces as debris number increases to larger debris fields. A similar,

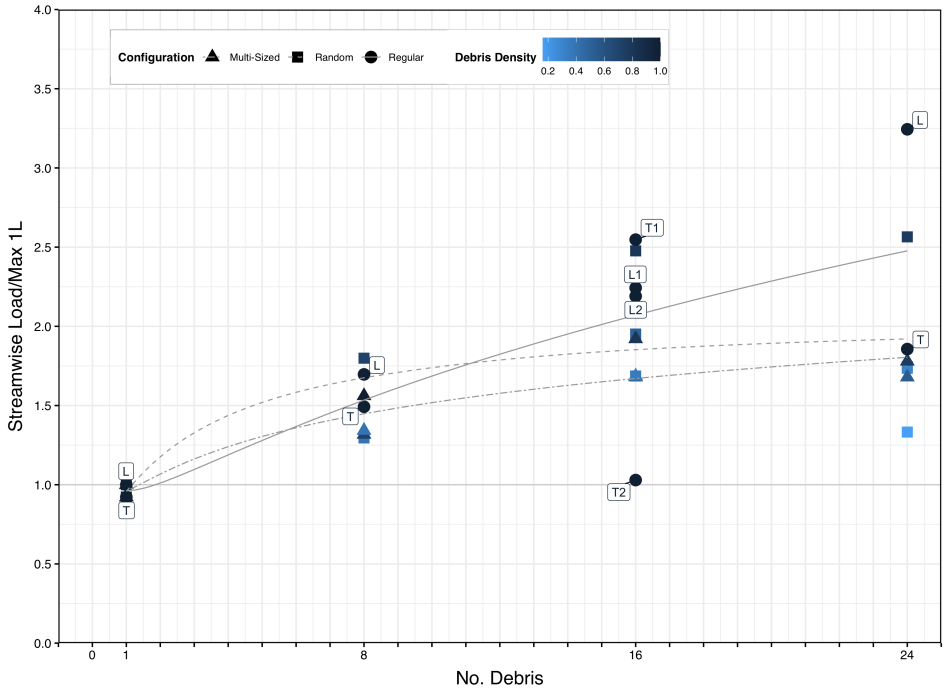


Figure 7.3: Median absolute maximum peak values for all tests.

logarithmic trend line is observed for debris comprised of a mix of full-sized and smaller debris pieces. In both cases, however, the trend lines show lower reaction forces for similar numbers of debris for both multi-sized and random configurations than for regular configurations. The effects of debris field density and composition are discussed in more depth in Sections 1.1.3 and 1.1.4.

Extreme values include the test with 16 debris in transverse configuration 2 (T2). This field is regularly configured with 100% initial debris field surface density (defined as the surface area of debris divided by the initial debris field total area) and is 2m wide, which exceeds the test structure face (approximately 1m wide). Thus, many debris miss the structure. Additionally, the width of the field may also serve to slow the motion in the direction of flow, as there is high drag with a high surface area perpendicular to the direction of flow. The least dense 24 debris "random" test also has a low force despite its mass, as the debris

field comprises the full width of the flume and debris are likely to miss impact with the test structure. To discuss variation more broadly, Figure 7.4 shows the normalized interquartile range (i.e., divided by median) for the maximum peak values for all tests.

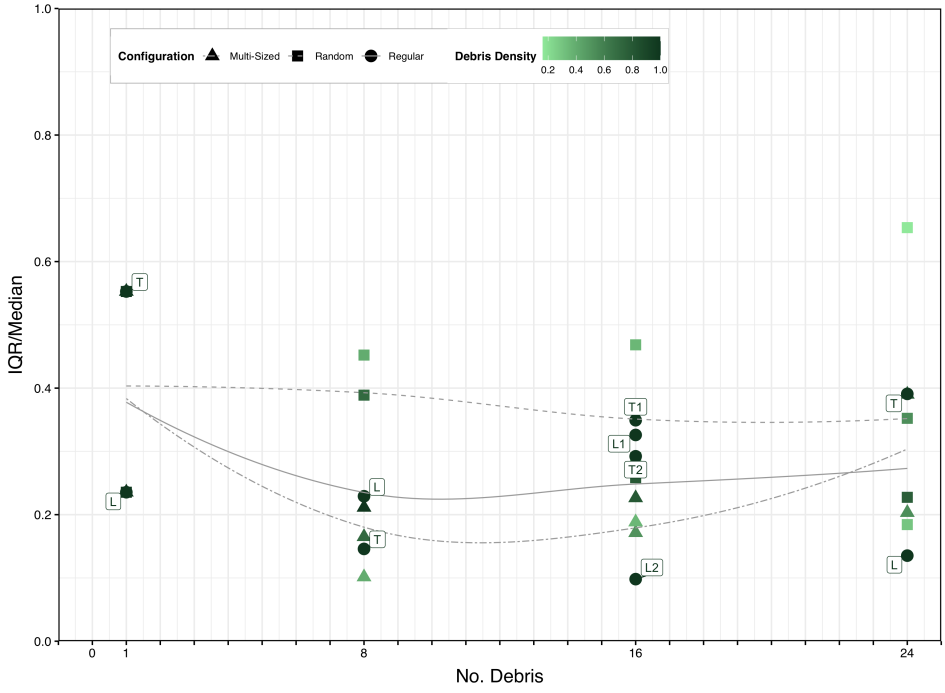


Figure 7.4: Normalized interquartile range for absolute maximum peak values for all tests.

Unlike median forces, there is less trend clarity in the normalized interquartile ranges for maximum peak values. There is not an increase in variability due to an increase in number of debris; in fact, the highest variability exists for the smallest number of debris. In a few instances, higher maximum peak reaction forces tend to have less variability (i.e., 24L and 16L2).

We see some correlation with debris field orientation for regular configurations. As observed with single debris, transverse orientations have higher variability in almost all cases.

The highest variability for number of debris tends to be low-density configurations. This is likely due to the width of debris fields exceeding the width of the test structure and/or

debris tending to be forced around the structure in its wake. In general, variability for absolute maximum peak value seems to be chaotic in nature.

### *7.1.3 Effect of Debris Field Density*

In this section, the effect of debris field density is discussed in more depth. We compare "random" vs. "regular" debris configurations. By definition, "regular" debris configurations have a 100% initial surface density (i.e., they are tightly-packed and tend to move cohesively before the first contact of the field with the structure). "Random" debris configurations have a surface area density less than 100%. We can compare tests with the same numbers of debris and size of individual debris pieces to determine the correlation of peak reaction forces and debris field density. Figure 7.5 shows normalized maximum forces as compared to debris field density.

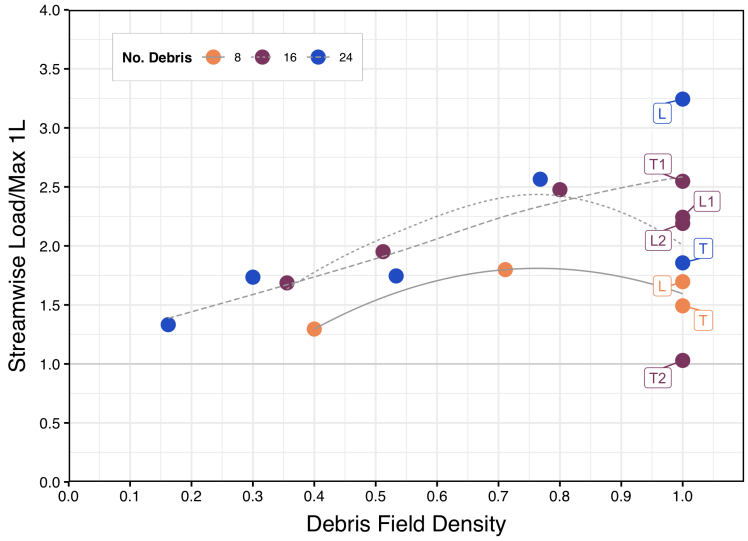


Figure 7.5: Debris field density versus median peak forces for regular and random configurations.

The number of debris is indicated via the legend shown. All points with debris field

density equal to 100% indicate regular configurations. For 8 debris, the randomly configured fields have a maximum reaction force at debris field density of approximately 70%. However, the maximum force measured at regular configurations (i.e, density equal to 100%) is not substantially lower than the maximum force among all tests. The lowest density configurations have the lowest peak force. The increasing density may lead to a higher initial impact; however, there is a possibility of the second peak exceeding the first, which may indicate a greater influence of debris interaction after a debris field's initial impact.

At 16 debris, the trend line shows higher reaction forces up to approximately 80% field density. At this point, lower reaction forces are seen at 100% density. Again, the second peak may be the higher peak; thus, the hypothesized, chaotic impacts after an initial contact may govern. Additionally, the trend line is sensitive to the extreme value discussed in the previous section (16 debris in configuration T2).

Finally, the trend line for 24 debris shows linearly increasing forces with debris field density. This indicates that for fields of this number of debris, those with 100% debris density show the highest maximum forces. Since this value (due to 24 debris oriented longitudinally) is the maximum reaction force, the governing impact is likely the initial impact of the cohesive mass with the test structure.

Overall, for all "random" configurations, increasing density is highly correlated with increasing peak force. For "regular" configurations, effects due to individual debris configuration (i.e., drag associated with transverse orientations) confound this finding for 100% debris field density in some cases, but still yield high reaction forces. If considered without maximum "regular" configuration forces, the linearly-increasing force with debris density would be apparent. However, the trend of peak force reduction observed in regular transverse debris orientations means that not all 100% dense configurations have higher reaction forces than lower density counterparts.

In addition to peak forces, variation between trials is also correlated with debris field density. Figure 7.6 shows normalized interquartile range versus debris field density for varying debris numbers. For all numbers of debris, variation tends to decrease with increasing debris

field density. However, substantial variation in peak forces from trend lines indicates that the variation between trials, even as correlated with density of the debris field, is chaotic in nature.

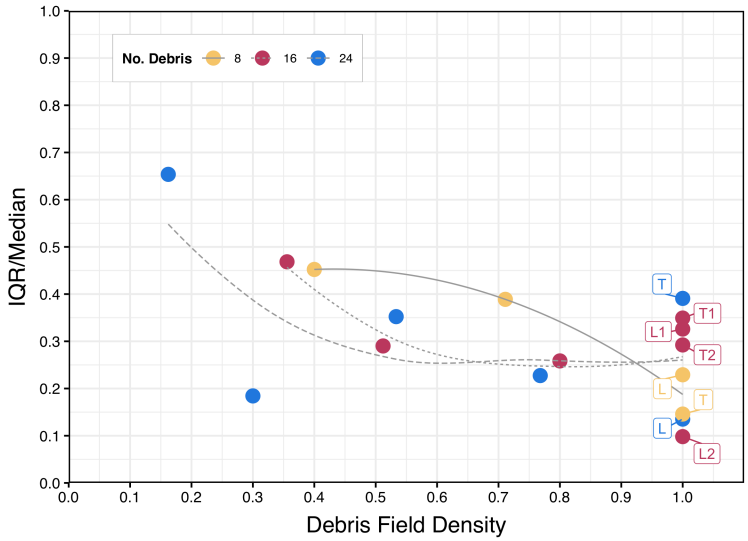


Figure 7.6: Debris field density versus normalized interquartile range for regular and random configurations.

For 8 debris, variation is lowest for regular configurations, whereas random configurations have significantly higher variation. 16 debris tests decrease in variability starting at density approximately equal to 0.35, then show approximately constant variability in the trend line after density equal to approximately 0.5. The lowest variability for 16 debris is a regular test; however, regular configurations may also have higher variability. For 24 debris, a similar trend is seen as that for 16 debris. The least dense configuration also has the highest variability among all tests shown. However, the next least dense 24 debris configuration has a variability similar to a regular configuration with 24 debris. Regular configurations also may have values higher than predicted by the trend line. While some trends in variability can be observed, the existence of extreme values indicates chaotic interactions that may confound

the prediction of variability between tests.

### *7.1.4 Effect of Composition of Debris Field*

In this section, the effect of individual debris sizes on peak forces is discussed. Within a debris field, either all standard-sized debris are used, or small debris are incorporated into the field to create an equivalent debris surface area. Configurations with the same debris density are considered in Figure 7.7, which shows normalized peak reaction forces as compared to debris field composition, number of debris, and debris field density.

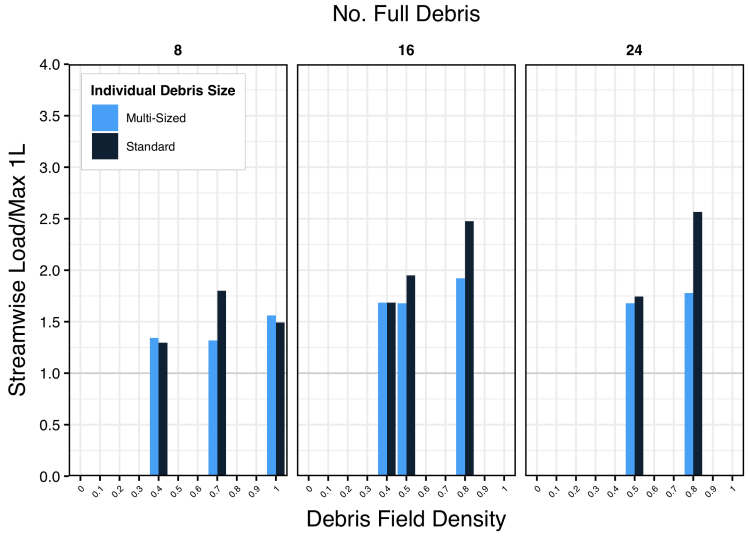


Figure 7.7: Debris field composition versus median peak forces.

Holding debris density and number of equivalent debris constant, we see a general trend of debris fields with standard-sized debris only with higher peak forces. For 8 debris, the lowest and highest debris densities indicate approximately equivalent peak values. However, 16 debris and 24 debris show standard-sized debris-only configurations have higher or equivalent forces than configurations with small debris, especially at higher densities. In general, higher density also correlates with a higher force for configurations with small debris.

In the case of 8 debris, the highest density configuration within Figure 7.7 is regular and oriented transversely to the direction of flow. The consistency of the forces for both the standard-sized debris-only field and the field with small debris is likely due to the cohesion of the debris field, acting to keep smaller debris pieces in place and involved in collisions. For all cases, the least dense configurations show equivalence between fields with small debris and fields that are standard-sized only. This is likely due to the lack of cohesion within the debris field and the propensity for lower forces (with or without small debris) since any size of debris may miss the structure. However, higher density random configurations tend to have higher maximum forces for fields with standard-sized debris only. This likely indicates that the contributions of smaller debris to the overall impact are less than standard-sized debris counterparts; they may act less cohesively since there are more and smaller pieces.

Discussion of variation is also important to understand the effects of small debris. Figure 7.8 shows normalized interquartile ranges for configurations with varying individual debris sizes. In many cases, standard-sized debris have higher variability between trials. In the most dense 8 and 24 debris trials, configurations with smaller debris have higher variability. The densest trials, by definition, have the highest degree of field cohesion. Thus, the smaller debris may play a role in decreasing cohesion and thus increasing variability between trials.

For most configurations, fields with standard-sized debris only tend to have higher variability. This may be due to the magnitude of forces due to single, full-sized debris impacts versus smaller debris (ref. Figure 7.1). In less dense configurations, more debris are likely to flow around the structure (i.e., a "miss") instead of impact it, and this may vary between trials. The effect of a small debris "miss" is less impactful to the overall field mass and impact force than the effect of a standard debris "miss"; thus, more variability may exist between trials with standard debris.

### *7.1.5 Comparison of First and Second Peaks*

As identified in Chapters 4 through 6, there are generally two peaks observed within time histories. The first peak force is hypothesized to be due to the first collision between the

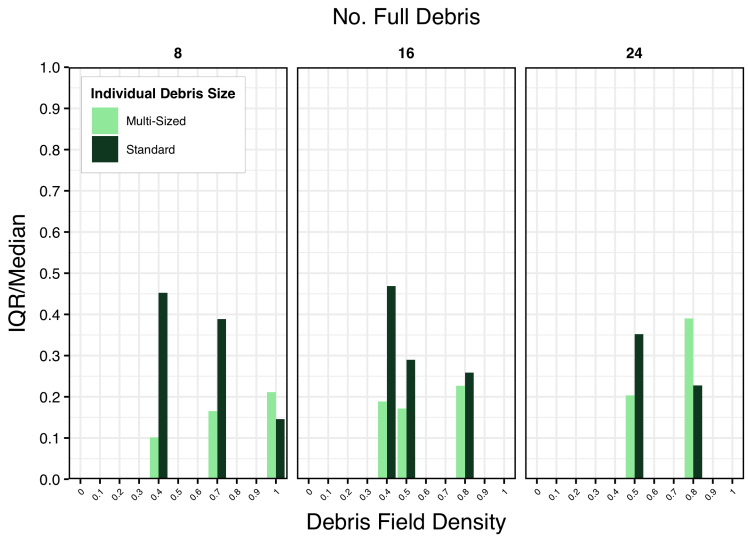


Figure 7.8: Debris field composition versus normalized interquartile range.

debris field and the test structure; the second peak is hypothesized to be due to chaotic collisions after the initial debris field has broken up after the initial impact. Figure 7.9 shows the first peak divided by second peak values to understand the correlation between the two peaks.

The densest configurations for 16 debris oriented longitudinally and 24 debris for regular, random, and multi-sized debris configurations exceed the line indicated as "1.0". This indicates that the hypothesized first impact exceeds the chaotic second impacts from a more randomized debris field. In the densest instances, most of the mass may collide during the first impact nearly simultaneously.

In the majority of tests, however, second peak values exceed first peak values. We see that less dense debris fields tend to have a lower ratio of first peak to second peak. Additionally, regular orientations with transverse orientations of individual debris tend to have a lower ratio of first peak to second peak. Again, this indicates that the dominant forcing in these cases comes from the hypothesized second peak, in which the debris field is broken up and

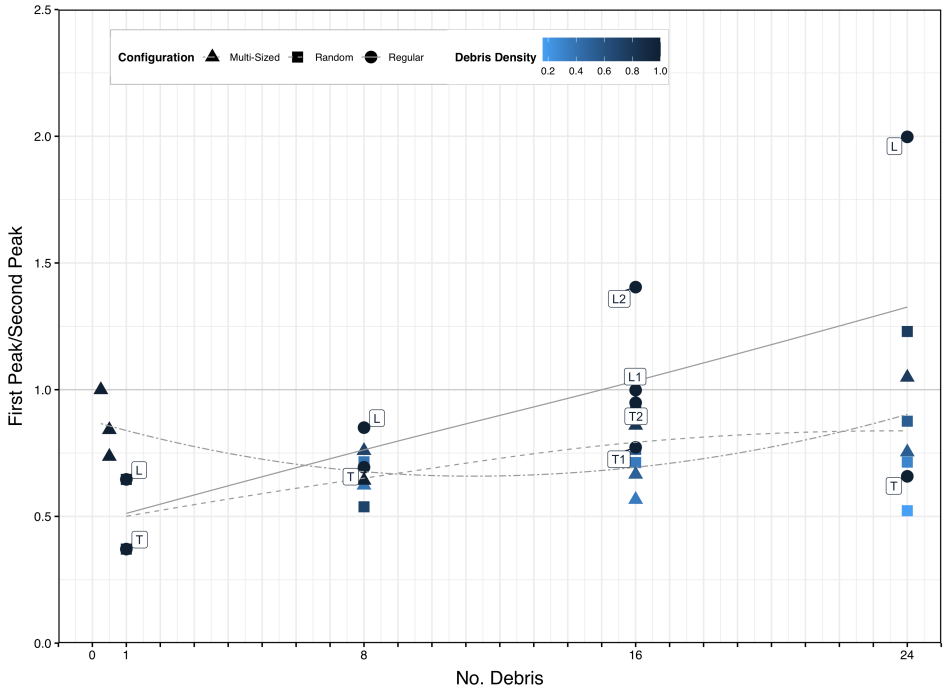


Figure 7.9: First peak divided by second peak.

more randomly oriented after the first impact. This may indicate slowing before impact (as in the case of transverse debris) and/or low-density initial debris fields in which the initial impact is not cohesive among the debris field mass.

## *7.2 Damming Forces*

To calculate the damming forces (as discussed in Chapter 4), a high-pass filter was applied via Fast Fourier Transform methods. The damming force is defined as the low-frequency elevation at a selected time (in all cases, 38.75 seconds) less the wave reaction force value at that point. We normalize the damming force by the median peak reaction force due to the wave only. For this discussion, we use the maximum damming force. Damming is hypothesized to be due to individual debris pieces becoming caught in the test structure legs after the first and second peak impact forces. Since damming is inherently nondeterministic,

the median value is not representative of possibilities that may be equally likely and more conservative for structural design. For example, in six out of 10 trials, all debris may miss, which would give a low median damming force. However, we consider the other four trials (in which damming may occur) to be equally as important to the discussion; thus, we discuss maximum damming forces in this section.

### *7.2.1 Effect of Single Debris Pieces*

This section discusses maximum damming forces due to individual pieces of debris. For single-debris tests, we hypothesize single debris damming forces are dependent on the maximum debris dimensions. Figure 7.10 shows the single debris trials conducted for debris of varying length.

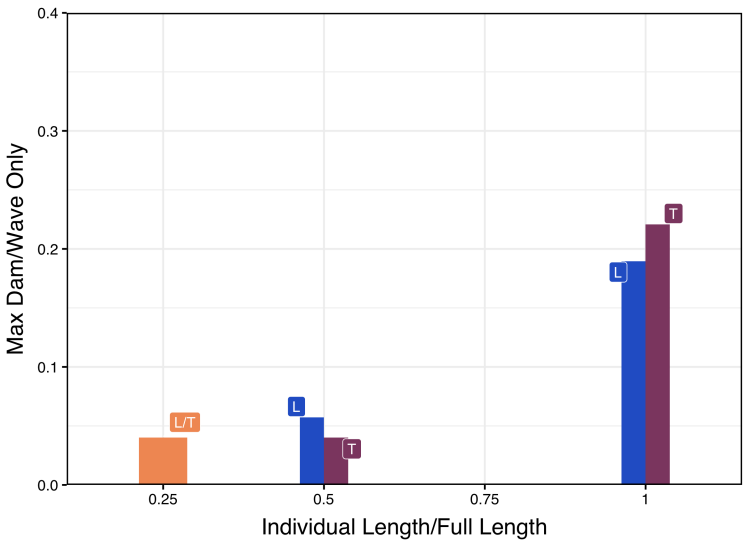


Figure 7.10: Maximum damming forces for single-debris tests.

We observe generally small forces for damming as compared to the median peak wave-only reaction force. The highest damming reaction force is due to a standard-sized debris oriented transversely. This is likely due to the fact that standard-sized debris pieces have

the longest maximum dimension. Among trials, the initial transverse orientation may serve to maintain the transverse orientation after initial impact with the test structure and while flowing underneath the box. Thus, less rotation is required to position this debris to become caught and dam. However, most damming due to single debris is small compared to the wave force and does not appear dependent on individual initial orientation.

Normalized interquartile ranges among trials is also considered in Figure 7.11. Here we can observe higher variations correlated to high forces. While the maximum damming forces may be higher, the variation indicates that there is a possibility of low damming forces, consistent with the hypothesis that damming is nondeterministic and dependent on whether or not individual debris get caught in the test structure legs.

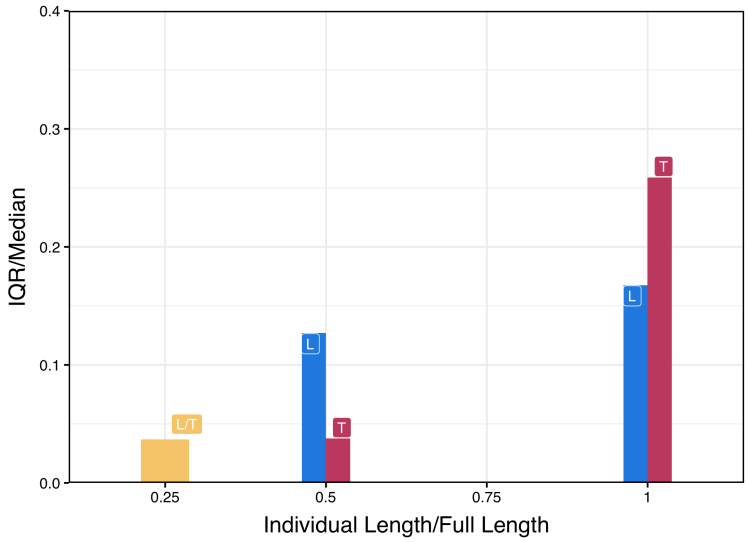


Figure 7.11: Normalized interquartile range for damming forces for single-debris tests.

Given that damming is nondeterministic, we anticipate that 10 trials with small debris fields are likely insufficient to understand all trends in damming forces and variability. For the purposes of this discussion, trends are analyzed through this lens. Further expansion of the understanding of damming phenomena likely requires larger debris fields and increased

trials per configuration to fully represent trends.

### *7.2.2 Effect of Number of Debris*

Damming forces are shown to correlate with number of debris in Figure 7.12. Several dense configurations exceed the maximum wave reaction force during damming. This indicates that damming should be considered significant compared to the forces due to the wave only for higher numbers of debris

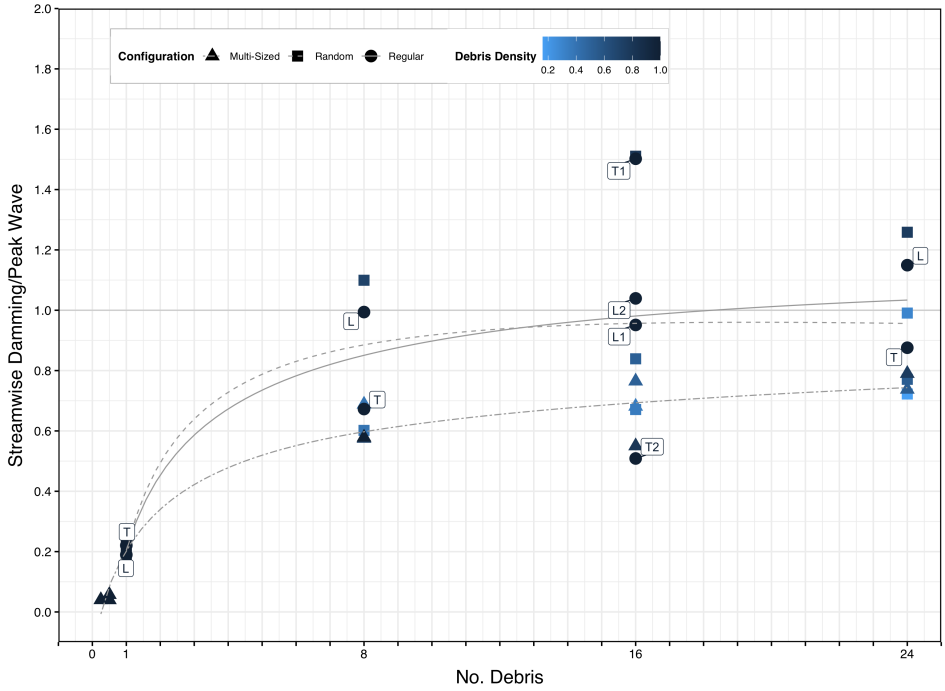


Figure 7.12: Maximum damming forces for all tests.

In all types of debris configurations, logarithmic trend lines are observed. Forces appear approximately constant despite larger numbers of debris as configurations near 24 debris. We observe that the "regular" and "random" debris trend lines are similar, and thus show similar damming regardless of initial debris field orientation. This will be explored in further depth in Section 7.2.3. The "multi-sized" debris configurations have consistently lower maximum

reaction forces for the same number of equivalent, standard-sized debris. This indicates that maximum damming force correlates with debris size; this will be discussed in Section 7.2.4.

To understand the effect of number of debris on the variability of damming, Figure 7.13 shows the normalized interquartile ranges compared to number of debris. The highest normalized interquartile is for the least dense 24 debris test. Since this test is the width of the flume, debris are likely to miss the test structure. The number of debris in contact with the structure per trial is variable and thus has the highest interquartile range. Another high interquartile range is from a 16 debris test with multiple-sized debris, indicating that a high range is likely given a configuration with multiple sizes of debris, even though the trial is dense (i.e., many debris would impact the box instead of miss).

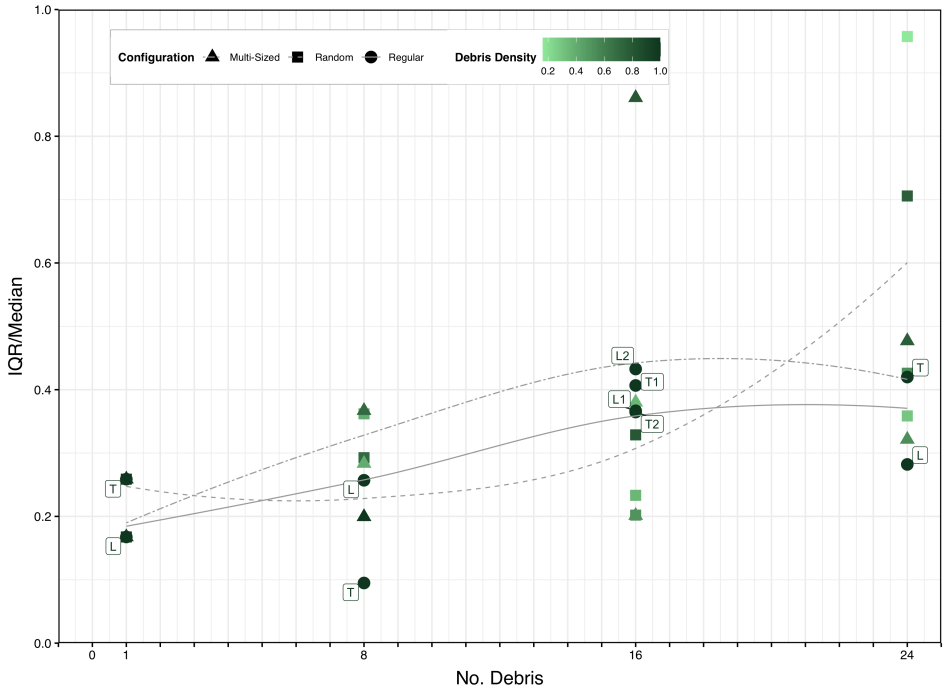


Figure 7.13: Normalized interquartile ranges for damming forces for all tests.

Regular debris configurations have the lowest variation in damming forces, and configurations with multiple-sized debris tends to have higher variability within equivalent numbers

of debris. There is not a clear correlation between density and variability in damming. Both the effects of debris field density and debris field composition will be discussed in Sections 7.2.3 and 7.2.4, respectively. Overall, we can hypothesize that damming is chaotic and relatively nondeterministic compared to peak force variation due to variation in number of debris. Additionally, we acknowledge the need for larger debris fields with more trials tested to fully elucidate damming trends.

### *7.2.3 Effect of Debris Field Density*

The effect of debris field density on maximum damming forces is explored in Figure 7.14. Both regular and random debris configurations are plotted and compared via their respective initial field density.

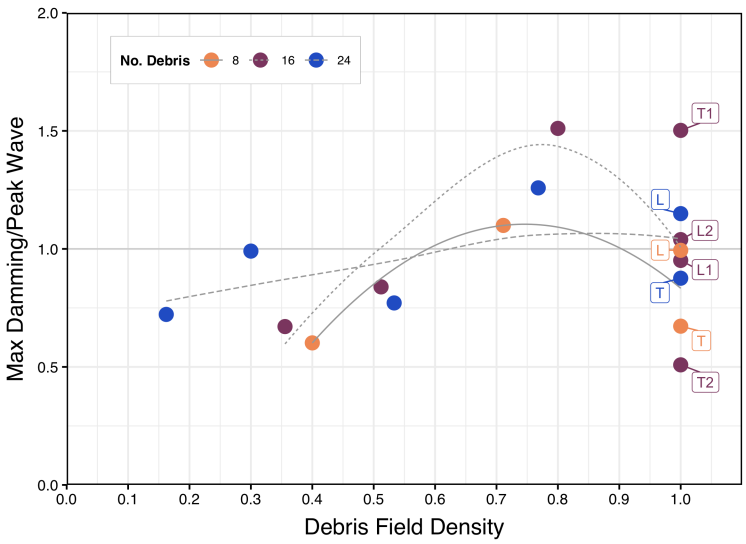


Figure 7.14: Debris field density versus maximum damming forces for regular and random configurations.

For 8 debris, the maximum damming force is observed at approximately 70% debris field surface area density. The lowest damming value is observed with the lowest debris densities.

While one regular configuration has a similar value to the maximum damming force for 8 debris, the other regular configurations have a much lower damming force. For 8 debris, intermediate densities tend to yield the highest damming forces.

A similar trend applies for 16 debris, which has a trend line maximum near approximately 80% debris field density. However, one regular debris configuration has a similar maximum damming force, while other regular debris configurations have the lowest observed maximum damming forces. These extreme values are observable in Figure 7.12.

For 24 debris, there is a more linear increase in damming forces; however, the maximum damming force is still found at a debris field density less than 100% (approximately 75%). We note that the trend line for 16 debris tends to exceed the 24 debris trend line. This is due to extreme values at intermediate debris densities exceeding regular configurations substantially. In the case of 24 debris, the trend of maximums at intermediate densities is not as pronounced.

Again, the observed trends show a maximum in damming reaction forces at intermediate densities. To further understand the trends between damming forces and debris field density, we plot the normalized interquartile ranges for all regular and random tests in Figure 7.15.

The normalized interquartile ranges for 8 and 24 debris configurations decrease with increasing density. However, 16 debris shows increasing variability with debris density. The lowest interquartile range has 8 debris and 100% debris field density, whereas the highest interquartile range is the least dense 24 debris configuration. If we assume that 16 debris interquartile ranges are highly similar, we propose that the interquartile range for damming forces is at least partly correlated with debris field density. However, the nondeterministic aspects of debris damming are evident in the variation in interquartile ranges and lack of trend consistency. We acknowledge the need for more and larger debris fields with more trials to fully elucidate damming trends.

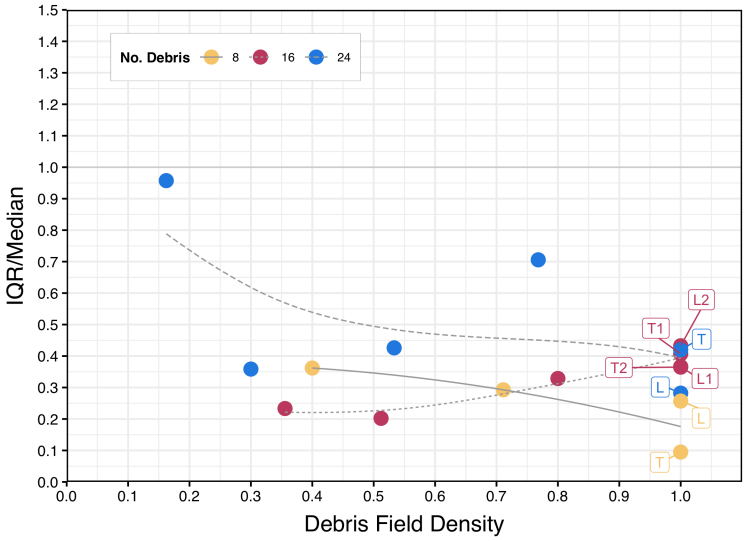


Figure 7.15: Debris field density versus damming normalized interquartile ranges for regular and random configurations.

### *7.2.4 Effect of Debris Field Composition*

In this section, we compare debris field composition (i.e., whether it is entirely comprised of standard-sized debris or small debris are present) and maximum damming forces. Figure 7.16 shows normalized peak reaction forces as compared to debris field composition, number of equivalent debris, and debris field density.

For the same debris field densities, higher maximum damming forces are generally present for configurations with standard-sized debris only. In the case of low-density 8 debris tests, the multi-sized maximum damming force exceeds the configuration with standard-sized debris, which is likely due to the chaotic nature of damming in general. It is possible that standard-sized debris present in the aforementioned multi-sized debris configuration may have caused a high damming force. However, it seems logical that a configuration with only standard-sized debris has a higher chance of debris becoming caught in test structure legs. Figure 7.17 shows variation in the form of normalized interquartile range for the same tests

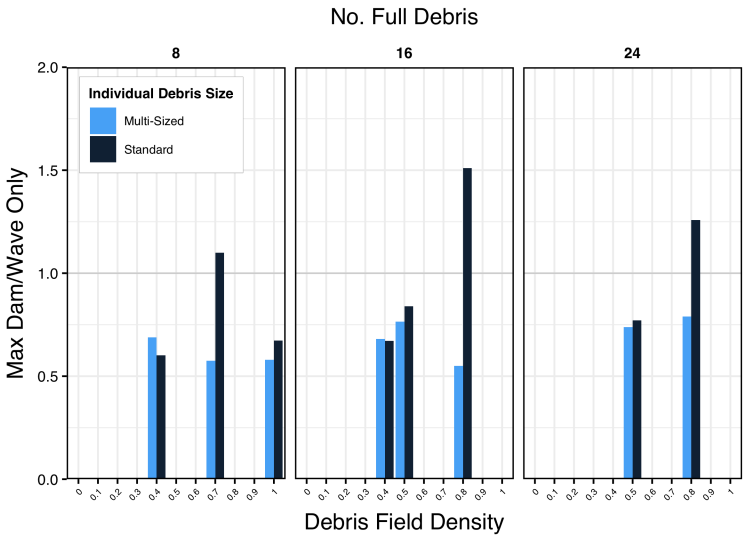


Figure 7.16: Debris field density versus damming normalized interquartile ranges for regular and random configurations.

with equivalent debris and debris field densities.

In the case of variability, there is not a clear correlation between the debris field compositions and range. For 8 and 16 debris, fields with small debris tend to have higher normalized interquartile ranges, while in 24 debris tests both tests have higher variability in standard-sized only tests. It should be noted that in 24 debris trials, the percentage of small debris decreases to 33% versus 50% for 8 and 16 debris trials. Since standard-sized debris are most likely to dam, more standard-sized debris within a configuration can cause more variation due to the change that either many debris or few debris may dam during an event, whereas the multi-sized debris fields have less debris that may dam since they have less standard-sized debris. Largely, the variability seems nondeteriministic in the case of maximum damming, and we acknowledge the need for more and larger debris fields with more trials tested to fully describe damming trends.

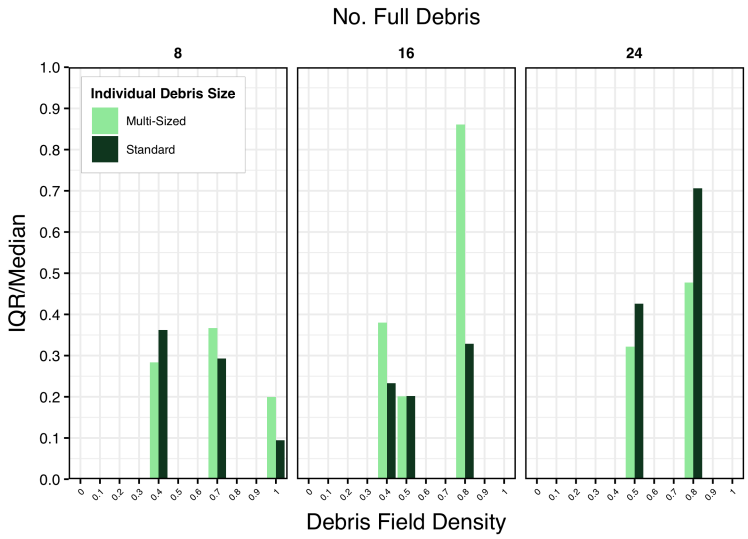


Figure 7.17: Debris field density versus damming normalized interquartile ranges for regular and random configurations.

### *7.2.5 Comparison of Maximum Peak Force & Damming Forces*

To understand the correlation between the peak forces and damming, Figure 7.18 shows the median damming reaction force divided by the absolute maximum peak reaction force. We observe that damming reaction forces are no more than 20% of peak reaction forces for any case. However, damming forces are a lower frequency load; therefore, they are sustained and represent significant structural loading as compared to high-frequency impact forcing. All configuration types show either a leveling of ratios at higher numbers of debris or a decrease toward 24 debris (in the case of regular configurations). The lowest ratios are present for multi-sized debris configurations.

There is also significant spread at higher numbers of debris. This indicates that the ratio of damming to peak forces is not strongly dependent on the number of debris in the trial. Given the nondeterministic nature of debris damming, the ratio of damming to peak reactions also tends toward nondeterminism.

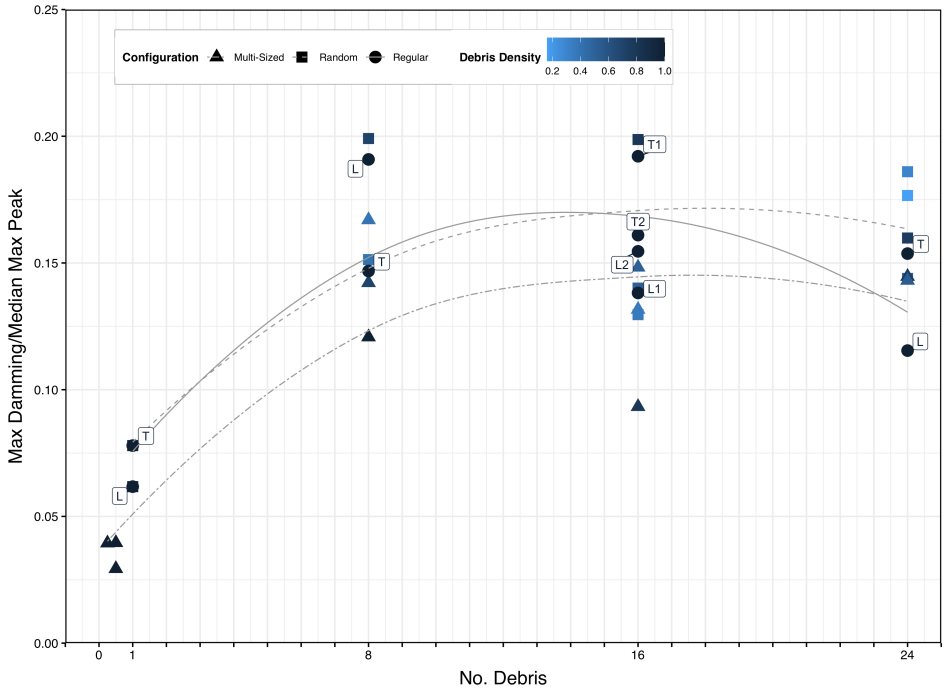


Figure 7.18: Max damming forces divided by max peak forces for all tests.

# Chapter 8
# CONCLUSIONS & FUTURE WORK

This thesis discusses the experimental evaluation of reaction forces sustained by a test-structure due to wave-driven debris fields. The intent of this work is to broaden the scientific understanding of debris fields in inundation-type flows, such as tsunamis and floods, to ultimately enhance coastal resilience in the face of cascading hazards (e.g., earthquake and tsunami).

The test program presented here was conducted at the NHERI Wave Research Lab's Large Wave Flume at Oregon State University over a several-month period. Over 400 trials were conducted to understand flow hydrodynamics, debris-structure interaction, and test structure system properties. This thesis focuses on the streamwise reaction forces during 300 trials with debris that were conducted over 30 tests. All 300 trials were conducted with a wave that remained unbroken throughout the test environment, a stationary debris frame to set an initial condition, and with neutrally-buoyant high-density polyethylene (HDPE) pieces.

Specifically, this thesis discusses the effects of the following variables on streamwise reaction forces:

1. number of debris
2. orientation of individual debris
3. debris field density
4. individual debris size

For all cases, streamwise force time histories indicate the presence of three distinct events.

A high-frequency peak is observed approximately 1-2 seconds before a second set of high-frequency peaks. After both peak events, there is sustained low-frequency loading. These three events are termed: "first peak", "second peak", and "damming".

Qualitative video analysis provides hypotheses for the causes of the first and second peaks. The first peak is likely due to the initial contact of the debris field with the test structure face. After debris collide, the debris field loses contact with the test structure and breaks up such that debris have independent, chaotic paths and may interact with other debris. The second peak occurs as individual debris are forced into various portions of the test structure (i.e., the test structure face and legs, if submerged).

According to Shekhar et al. (2020), damming is hypothesized to be a result of individual debris pieces becoming trapped on the legs of the test structure, increasing the surface area of the structure perpendicular to the direction of flow. Damming is chaotic in nature since it is the result of individual debris orientations and paths after impacts break up the debris field.

Analysis of these three events yields findings that extend and expand previous work (i.e., Shekhar et al. (2020)). Key findings are summarized as follows:

1. Single debris oriented longitudinally to the direction of flow have peak reaction forces that are an order of magnitude lower than that calculated using an idealized, single degree-of-freedom elastic collision in air, likely due to drag and slowing effects of a leading water volume before impact with the test structure. The idealized force is approximately one order of magnitude greater than measured reaction forces. This is a significant finding, as it may inform existing design considerations for individual inundation-driven debris impacts.

2. Single debris oriented longitudinally to the direction of flow have higher peak forces and less peak force variability across trials than single debris oriented transversely. This is likely due to the increase in drag on a transverse debris that may cause slowing and rotation before impact. This effect is also observed in debris fields with larger numbers

of tightly-packed debris moving cohesively.

3. Increasing number of debris yields increasing peak forces at a decreasing rate. The highest median peak force (with 24 debris) among trials for that configuration is only 3.25 times the median peak force for a single debris.

4. Increasing debris field density yields higher peak forces for debris fields up to 100% debris field density. At the highest densities (debris field density = 100%) when the debris field is tightly-packed, effects of the orientation of the field acting cohesively (e.g., drag in transverse orientations seen in single debris trials) may cause lower forcing than less dense fields.

5. The presence of small debris in a field with equivalent surface area of debris tends to correlate with reduced peak forces overall.

6. For most tests, second peak reaction forces tend to be higher than first peak forces. This indicates that the random interaction of debris with the structure after the initial impact of the debris field with the structure face actually yields higher loads than the initial impact itself. Exceptions to this phenomenon occur with highly cohesive debris fields with high mass, where nearly all of the initial mass collides with the test structure at once.

7. The reaction forces due to damming phenomena are variable and chaotic in nature, but tend to increase with number of debris and debris density (if less than 100%) and decrease with more small debris within a field. While damming is only, at most, 20% of the peak loading for a given configuration, it represents a lower frequency, sustained loading that is structurally significant. Higher testing volume (i.e., more debris and more trials) would yield an increased understanding of damming.

The findings from this thesis can be extended into future work. In particular, this thesis represents a portion of data collected during experimentation at the Large Wave Flume. Likely avenues include the interaction of first peak, second peak, and damming loading.

Future analysis of existing streamwise reaction force data includes: a) using a randomizing (i.e., electromagnetic/"drop" frame) instead of stationary frame, b) using breaking wave conditions, and c) further understanding of the test structure system dynamics. For all conditions, the analysis of transverse and vertical loading is also important future work.

Additionally, data was collected via onboard, debris-mounted accelerometers (called Xsens DOTS). Video data were collected using high-speed cameras and GoPros. The combination of this data may yield understanding of debris position and path, velocity, and rotational motion during individual tests.

This experimental data is intended to be model validation for finite element (FEM), computational fluid dynamics (CFD), and multi-point-method (MPM) numerical models that can be used to predict a wide variety of structural, flow, and debris conditions far beyond the scope of experimentation.

Ultimately, this work seeks to be part of a growing number of projects contributing to coastal resilience for communities worldwide. A better understanding of chaotic events that incorporates our increasing knowledge of a changing world, including sea-level rise and the potential cascading coastal hazards, may lead to more lives saved during the next catastrophic tsunami, flood, or storm surge. The author hopes that this work, in some small part, makes the world a little safer.

# REFERENCES

Aghl, P. P., Naito, C. J., and Riggs, H. R. (2017). "A simplified model for estimating axial impact forces resulting from debris with non-uniform nonstructural mass." *Advances in Structural Engineering*, 20(6), 963–975.

Akiyama, M., Frangopol, D. M., Arai, M., and Koshimura, S. (2013). "Reliability of bridges under tsunami hazards: Emphasis on the 2011 Tohoku-Oki earthquake." *Earthquake Spectra*, 29(1_suppl), 295–314.

Alam, M. S., Winter, A. O., Galant, G., Shekhar, K., Barbosa, A. R., Motley, M. R., Eberhard, M. O., Cox, D. T., Arduino, P., and Lomonaco, P. (2020). "Tsunami-like wave-induced lateral and uplift pressures and forces on an elevated coastal structure." *Journal of Waterway, Port, Coastal, and Ocean Engineering*, 146(4), 04020008.

ASCE (2016). *Minimum Design Loads for Buildings and Other Structures. ASCE 7-16.* American Society of Civil Engineering.

Chock, G. (2013). "ASCE/JSCE Tohoku tsunami investigation of structural damage and development of the ASCE 7 tsunami design code for buildings and other structures ".

Chopra, A. K. (2017). *Dynamics of Structures: Theory and applications to earthquake engineering.* Pearson, fifth edition.

Dean, R. G. and Dalrymple, R. A. (1991). *Water Wave Mechanics for Engineers and Scientists.* World Scientific.

Derschum, C., Nistor, I., Stolle, J., and Goseberg, N. (2018). "Debris impact under extreme hydrodynamic conditions Part 1: Hydrodynamics and impact geometry." *Coastal Engineering*, 141, 24–35.

Ghasemi, A. and Zahediasl, S. (2012). "Normality tests for statistical analysis: A guide for non-statisticians." *International Journal of Endocrinology and Metabolism*, 10(2), 486–489.

Ghobarah, A., Saatcioglu, M., and Nistor, I. (2006). "The impact of the 26 December 2004 earthquake and tsunami on structures and infrastructure." *Engineering Structures*, 28(2), 312–326.

Gschnitzer, T., Gems, B., Mazzorana, B., and Aufleger, M. (2017). "Towards a robust assessment of bridge clogging processes in flood risk management." *Geomorphology*, 279, 128–140.

Haehnel, R. B. and Daly, S. F. (2004). "Maximum impact force of woody debris on floodplain structures." *Journal of Hydraulic Engineering*, 130(2), 112–120.

Hasanpour, A., Istrati, D., and Buckle, I. (2021). "Coupled SPH–FEM modeling of tsunami-borne large debris flow and impact on coastal structures." *Journal of Marine Science and Engineering*, 9(10), 1068.

Heaton, T. H. and Hartzell, S. H. (1987). "Earthquake hazards on the Cascadia Subduction Zone." *Science*, 236(4798), 162–168.

Ko, H. T.-S., Cox, D. T., Riggs, H. R., and Naito, C. J. (2015). "Hydraulic experiments on impact forces from tsunami-driven debris." *Journal of Waterway, Port, Coastal, and Ocean Engineering*, 141(3), 04014043.

Kobayashi, M. H., Genest, R., Riggs, H. R., and Paczkowski, K. (2012). "Simple hydroelastic impact models for water-borne debris." *Proceedings of the Institution of Mechanical Engineers, Part M: Journal of Engineering for the Maritime Environment*, 226(2), 170–179.

Lebreton, L. C.-M. and Borrero, J. C. (2013). "Modeling the transport and accumulation floating debris generated by the 11 march 2011 tohoku tsunami." *Marine Pollution Bulletin*, 66(1-2), 53–58.

Leonard, G. S., Evans, N., Prasetya, G., Saunders, W., Pearse, L., Monastra, D., and Fraser, S. (2011). "Scoping study for evaluating the tsunami vulnerability of New Zealand buildings for use as evacuation structures." *GNS Science*, 2011/36 . Technical report.

Madurapperuma, M. A. K. M. and Wijeyewickrema, A. C. (2012). "Inelastic dynamic analysis of an RC building impacted by a tsunami water-borne shipping container." *Journal of Earthquake and Tsunami*, 06(01), 1250001.

McCullough, M. C., , Kareem, A., Donahue, A. S., and Westerink, J. J. (2013). "Structural damage under multiple hazards in coastal environments." *Journal of Disaster Research*, 8(6), 1042–1051.

Naito, C., Cercone, C., Riggs, H. R., and Cox, D. (2014). "Procedure for site assessment of the potential for tsunami debris impact." *Journal of Waterway, Port, Coastal, and Ocean Engineering*, 140(2), 223–232.

Naito, C., Riggs, H. R., Wei, Y., and Cercone, C. (2016). "Shipping-container impact assessment for tsunamis." *Journal of Waterway, Port, Coastal, and Ocean Engineering*, 142(5), 05016003.

OSU (2021). "Land Acknowledgement." *Institutional Diversity*, <https://diversity.oregonstate.edu/feature-story/land-acknowledgement> (Oct).

Paczkowski, K., Riggs, H., Naito, C., and Lehmann, A. (2012). "A one-dimensional model for impact forces resulting from high mass, low velocity debris." *Structural Engineering and Mechanics*, 42(6), 831–847.

Palermo, D., Nistor, I., Saatcioglu, M., and Ghobarah, A. (2013). "Impact and damage to structures during the 27 February 2010 Chile tsunami." *Canadian Journal of Civil Engineering*, 40(8), 750–758.

Paulik, R., Gusman, A., Williams, J. H., Pratama, G. M., lin Lin, S., Prawirabhakti, A., Sulendra, K., Zachari, M. Y., Fortuna, Z. E. D., Layuk, N. B. P., and Suwarni, N. W. I.

(2019). "Tsunami hazard and built environment damage observations from Palu City after the September 28 2018 Sulawesi earthquake and tsunami." *Pure and Applied Geophysics*, 176(8), 3305–3321.

Petersen, M. D., Moschetti, M. P., Powers, P. M., Mueller, C. S., Haller, K. M., Frankel, A. D., Zeng, Y., Rezaeian, S., Harmsen, S. C., Boyd, O. S., Field, E. H., Chen, R., Rukstales, K. S., Luco, N., Wheeler, R. L., Williams, R. A., and Olsen, A. H. (2014). "Documentation for the 2014 update of the United States national seismic hazard maps, <https://doi.org/10.3133/ofr20141091>.

Reuters (2015). "When the Japan tsunami struck." *Reuters/Mainichi Shimbun* . 10 Mar 2015.

Schmocker, L. and Hager, W. H. (2011). "Probability of drift blockage at bridge decks." *Journal of Hydraulic Engineering*, 137(4), 470–479.

Shafiei, S., Melville, B. W., Shamseldin, A. Y., Beskhyroun, S., and Adams, K. N. (2016). "Measurements of tsunami-borne debris impact on structures using an embedded accelerometer." *Journal of Hydraulic Research*, 54(4), 435–449.

Shekhar, K., Winter, A. O., Alam, M. S., Arduino, P., Miller, G. R., Motley, M. R., Eberhard, M. O., Barbosa, A. R., Lomonaco, P., and Cox, D. T. (2020). "Conceptual evaluation of tsunami debris field damming and impact forces." *Journal of Waterway, Port, Coastal, and Ocean Engineering*, 146(6), 04020039.

Stolle, J., Goseberg, N., Nistor, I., and Petriu, E. (2019). "Debris impact forces on flexible structures in extreme hydrodynamic conditions." *Journal of Fluids and Structures*, 84, 391–407.

Suppasri, A., Mas, E., Charvet, I., Gunasekera, R., Imai, K., Fukutani, Y., Abe, Y., and Imamura, F. (2013). "Building damage characteristics based on surveyed data and fragility curves of the 2011 Great East Japan Tsunami." *Natural Hazards*, 66(2), 319–341.

Tomita, T. and Honda, K. (2011). "Practical model to estimate drift motion of vessels by tsunami." *Coastal Engineering Proceedings*, 1(32), 27.

UW (2022). "Native Life & Tribal Relations." *Diversity at the UW*, <https://www.washington.edu/diversity/tribal-relations/>.

Winter, A. O. (2019). "Effects of flow shielding and channeling on tsunami-induced loading of coastal structures." Ph.D. thesis, University of Washington, Seattle, WA.

Winter, A. O., Alam, M. S., Shekhar, K., Motley, M. R., Eberhard, M. O., Barbosa, A. R., Lomonaco, P., Arduino, P., and Cox, D. T. (2020). "Tsunami-like wave forces on an elevated coastal structure: Effects of flow shielding and channeling." *Journal of Waterway, Port, Coastal, and Ocean Engineering*, 146(4), 04020021.

Yamaguchi, D. K., Atwater, B. F., Bunker, D. E., Benson, B. E., and Reid, M. S. (1997). "Tree-ring dating the 1700 Cascadia earthquake." *Nature*, 389(6654), 922–923.

Yeh, H., Barbosa, A. R., Ko, H., and Cawley, J. G. (2014). "Tsunami loadings on structures: Review and analysis." *Coastal Engineering Proceedings*, 1(34), 4.

# Appendix A

# REDUCTION IN PEAK REACTION FORCES DUE TO FILTERING TECHNIQUES

Peak values discussed are taken from raw streamwise impact force time histories. Filtering is shown to be non-conservative within this appendix. Frequencies are removed in the frequency domain after a Fast Fourier Transform. While low-pass (i.e., removing signals with frequencies above a certain threshold) filtering is intrinsic to the discussion of damming forces, peak forces are not filtered.

A high-pass filter applied to a selected trial for a single debris oriented longitudinally, centered at 4 Hz (similar to Shekhar et al. (2020)) with a cumulative density function shape and a standard deviation of 1 Hz is shown in Figure A.1. By inspection, there is a clear reduction in peak values, as low frequency signals (e.g., the wave itself) are removed.

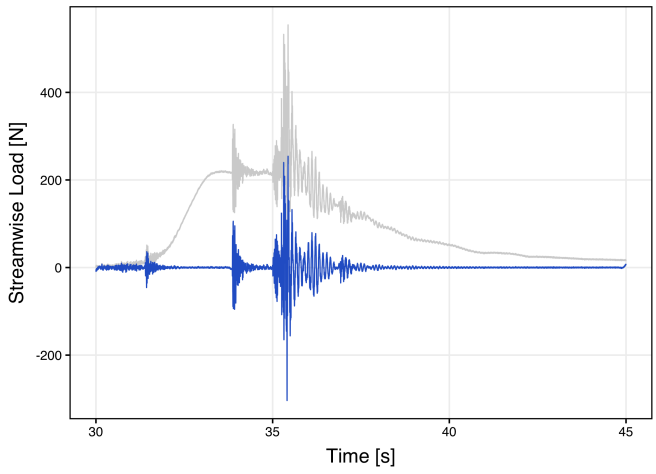


Figure A.1: High pass filter centered at 4 Hz applied to select trial for a single debris oriented longitudinally; GRAY indicates raw data, BLUE indicates filtered data.

Applying a low pass filter using a similar cumulative density function centered at 4 Hz, 40 Hz, 100 Hz, and 200 Hz is shown in Figure A.2. The values are chosen to give a representative range of filters. By inspection, we see either a reduction in peak forces or minimal change to the signal.

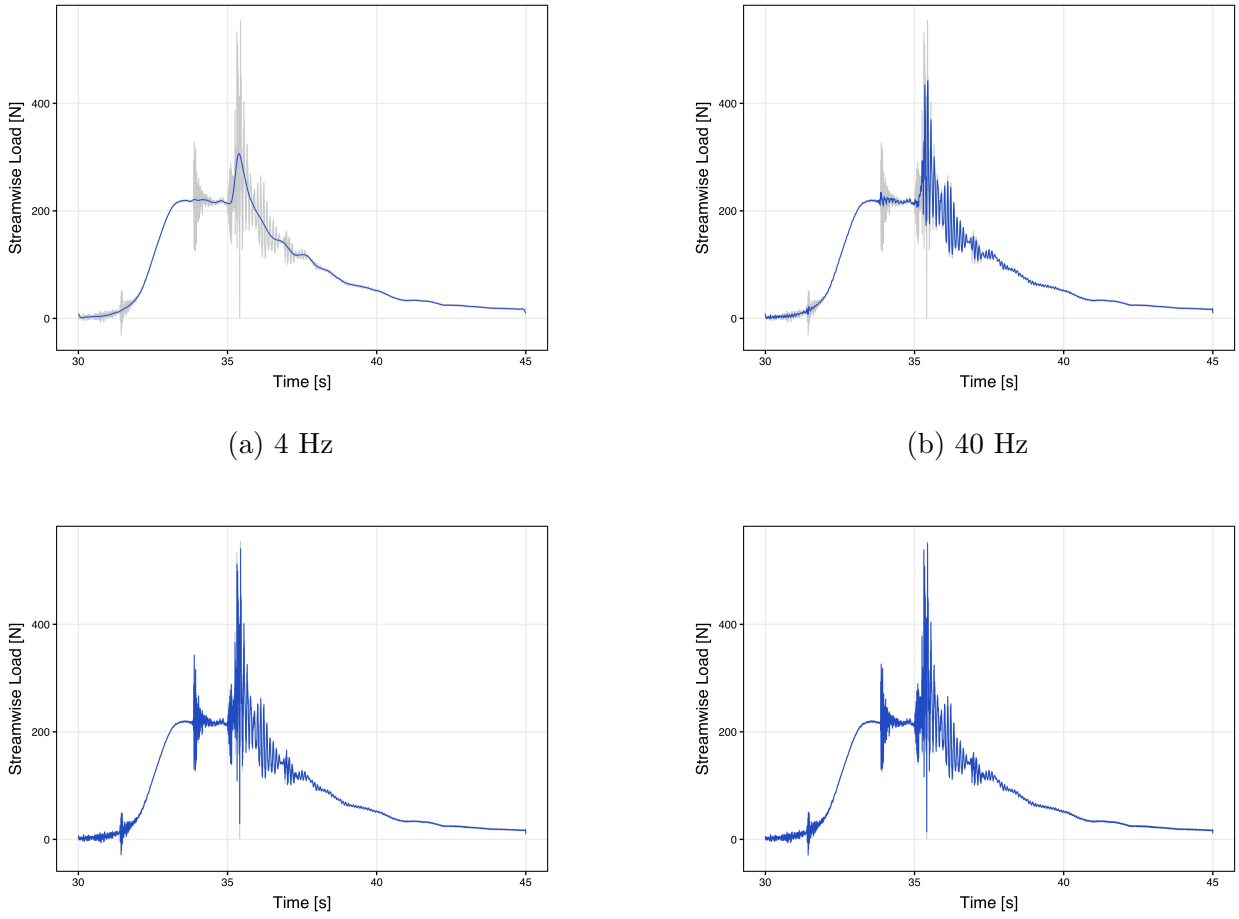


(a) 4 Hz

(b) 40 Hz

(c) 100 Hz

(d) 200 Hz

Figure A.2: Low pass filters applied at varying mean values for a selected trial for a single debris oriented longitudinally; GRAY indicates raw data, BLUE indicates filtered data.

# Appendix B

# IDEALIZED DEBRIS SINGLE DEGREE-OF-FREEDOM COLLISION CALCULATIONS

## *B.1 Collision Time*

To understand idealized system dynamics, a single degree-of-freedom (SDOF) axial rod approximation is used for a single debris piece oriented longitudinally. We assume that the debris has a stiffness, $k$, and collides with a rigid boundary in an elastic collision. Figure B.1 shows a diagram of the idealized system. Note: these calculations are largely based on Chopra (2017).

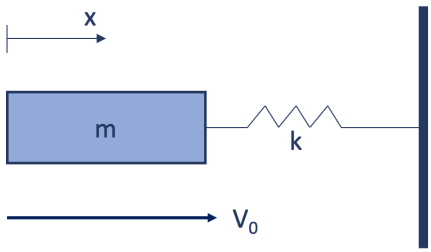


Figure B.1: Idealized SDOF system diagram.

First, we assume the debris has a velocity prior to collision equal to $V_0$. It is assumed that the system debris has a natural angular frequency:

$$\omega_n = \sqrt{\frac{k}{m}}$$

where $m$ is the known mass of the debris, 2.52 kg. We can write the natural frequency:

$$f_n = \frac{\omega_n}{2\pi} = \frac{1}{2\pi}\sqrt{\frac{k}{m}}$$

We can convert to natural period:

$$T_n = \frac{1}{f_n} = 2\pi\sqrt{\frac{m}{k}}$$

The equation of motion for a system undergoing undamped free vibration without any external excitation is shown in Chopra (2017) to be:

$$m\ddot{u}(t) + ku(t) = 0$$

where $u$ is position and $\ddot{u}$ is acceleration. Given initial conditions, $u_0$ and $\dot{u_0}$ (where $\dot{u}$ is velocity), the solution is assumed to be in the form:

$$u(t) = A\sin(\omega_n t) + B\cos(\omega_n t)$$

Solving, we obtain:

$$u(t) = \frac{\dot{u_0}}{\omega_n}\sin(\omega_n t) + u_0\cos(\omega_n t)$$

In this case, $u_0 = 0$ since we assume the collision begins at a zero-position. $\dot{u_0} = V_0$, which is the velocity of the debris at collision. We can substitute:

$$u(t) = \frac{V_0}{\omega_n}\sin(\omega_n t)$$

The maximum displacement $u$ occurs is at $t = \frac{\pi}{2\omega_n}$ and gives:

$$u_{max} = \frac{V_0}{\omega_n} = V_0\sqrt{\frac{m}{k}}$$

We assume that the total collision time is where the displacement returns to 0, which occurs at $\omega_n t = \pi$. Thus,

$$t_{collision} = \frac{\pi}{\omega_n} = \frac{T_n}{2} = \pi\sqrt{\frac{m}{k}}$$

For the debris dimensions presented in Chapter 2, the collision time is a function of the properties of the debris, where $m$ is 2.52 kg and we can define the stiffness:

$$k = \frac{EA}{L}$$

where $E$ is the modulus of elasticity (0.8 GPa), $A$ is the cross-sectional area (0.0052 $m^2$), and $L$ is the length of the debris (0.500 m). Thus, the collision idealized collision time is:

$$t_{collision} = 0.00175s$$

### *B.2 Impact Force*

The idealized impact force can be approximated using this idealization. We can find the acceleration in an undamped system undergoing free vibration. Taking the integral of position, we obtain:

$$\ddot{u}(t) = -V_0\omega_n \sin(\omega_n t)$$

Thus, the force can be written as:

$$F = m\ddot{u} = -V_0\sqrt{mk}\sin(\omega_n t)$$

The maximum force magnitude is:

$$F_{max} = V_0\sqrt{mk}$$

Given the assumed velocity provided in Shekhar et al. (2020) and discussed in Chapter 4, the idealized initial velocity is $V_0 = 1.3m/s$. Thus:

$$F_{max} = 5950N$$

# Appendix C

# QQ-PLOTS FOR ALL CONFIGURATIONS

To establish approximate normality in streamwise reaction force peak value distributions, Shapiro-Wilk tests are conducted (see main text) and QQ-plots are used for visual inspection. As described in Chapter 4, an approximately linear distribution shown in QQ-plots correlates with approximate normality.

The following figures show all QQ-plots for the absolute maximum, FIRST peak, and SECOND peak for all configurations. See Chapter 4 for further discussion.

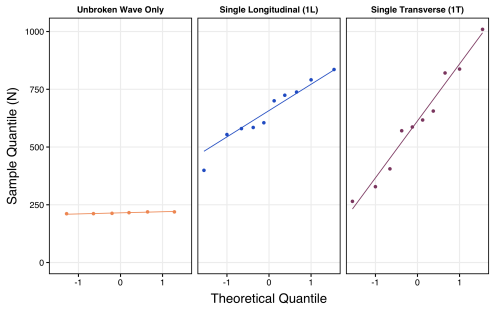


(a) Absolute maximum peak.

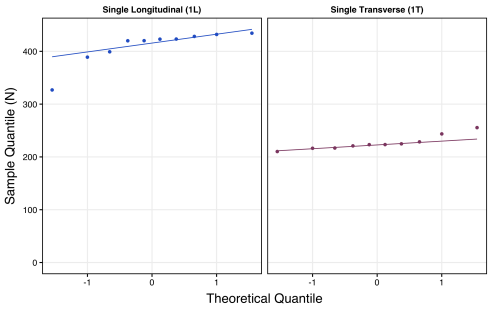


(b) First peak.

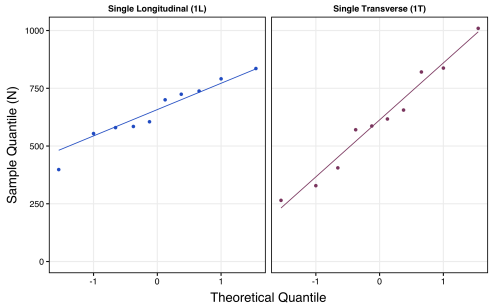


(c) Second peak.

Figure C.1: QQ-plots for absolute maximum, FIRST peak, and SECOND peak values for all standard-sized, single debris trials and wave-only trials.

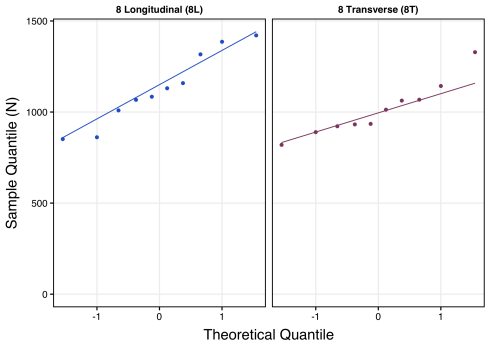


(a) Absolute maximum peak.

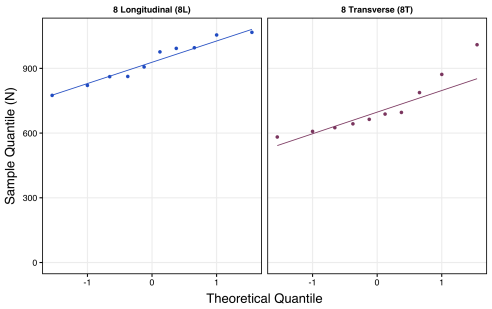


(b) First peak.

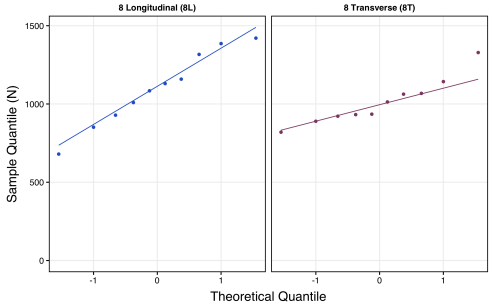


(c) Second peak.

Figure C.2: QQ-plots for absolute maximum, FIRST peak, and SECOND peak values for all regular, standard-sized, 8 debris trials.

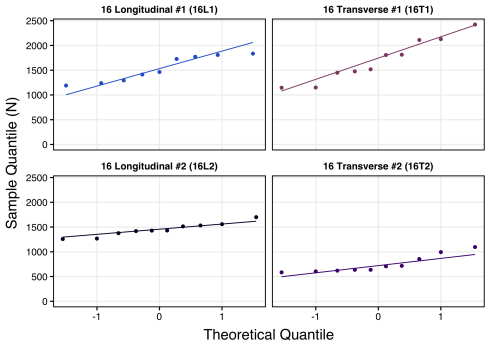


(a) Absolute maximum peak.

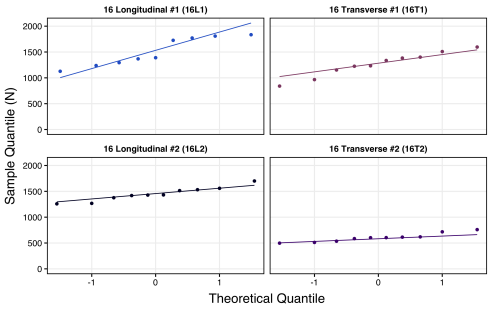


(b) First peak.

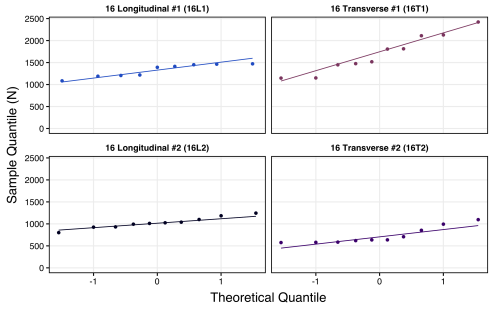


(c) Second peak.

Figure C.3: QQ-plots for absolute maximum, FIRST peak, and SECOND peak values for all regular, standard-sized, 16 debris trials.

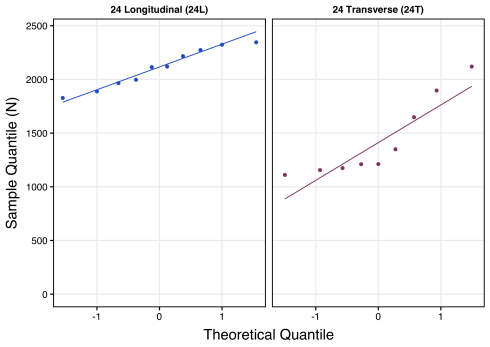


(a) Absolute maximum peak.

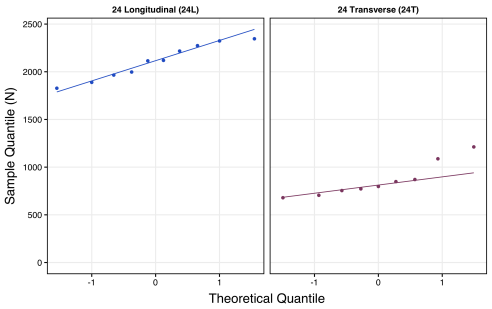


(b) First peak.

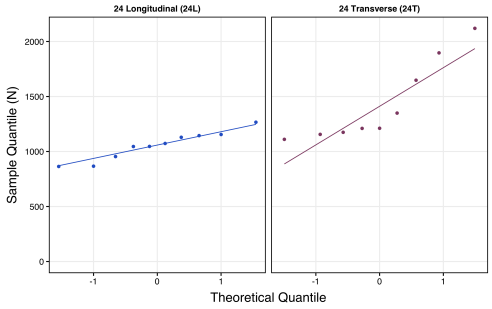


(c) Second peak.

Figure C.4: QQ-plots for absolute maximum, FIRST peak, and SECOND peak values for all regular, standard-sized, 24 debris trials.

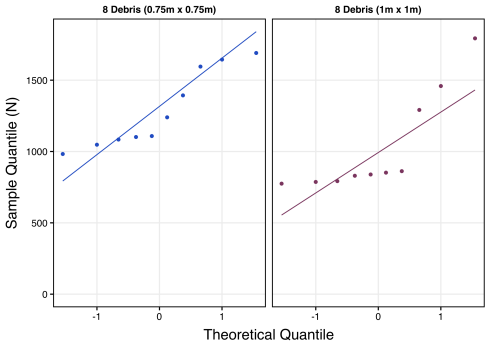


(a) Absolute maximum peak.

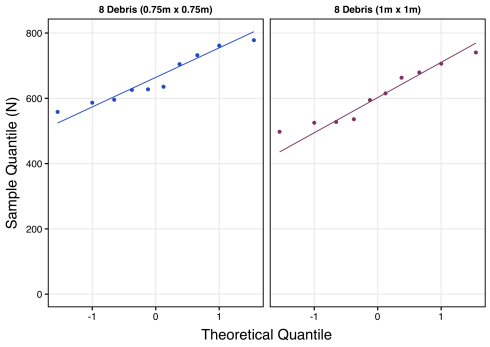


(b) First peak.

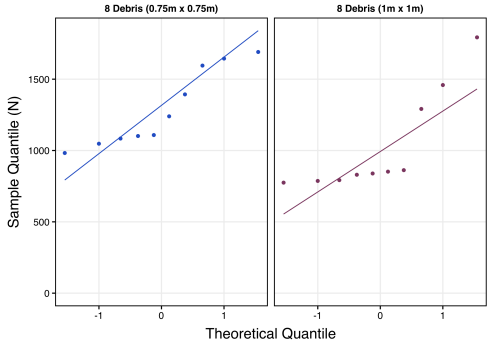


(c) Second peak.

Figure C.5: QQ-plots for absolute maximum, FIRST peak, and SECOND peak values for all random, standard-sized, 8 debris trials.

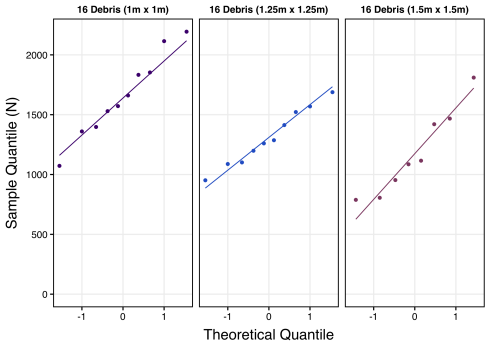


(a) Absolute maximum peak.

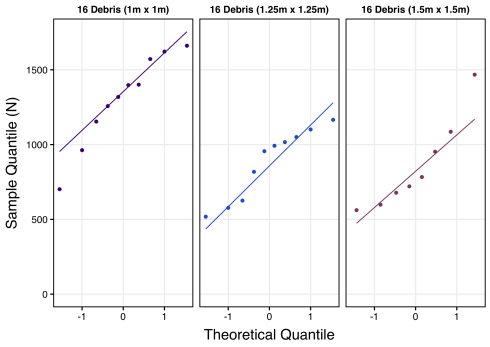


(b) First peak.

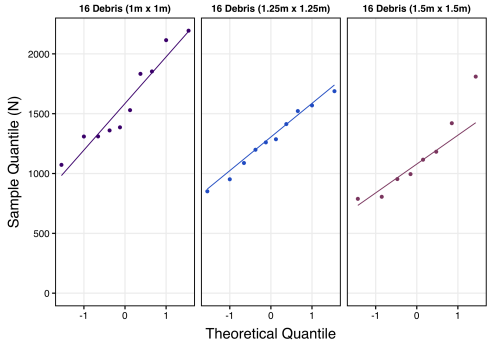


(c) Second peak.

Figure C.6: QQ-plots for absolute maximum, FIRST peak, and SECOND peak values for all random, standard-sized, 16 debris trials.

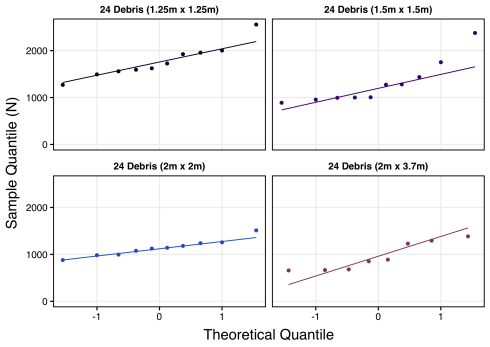


(a) Absolute maximum peak.

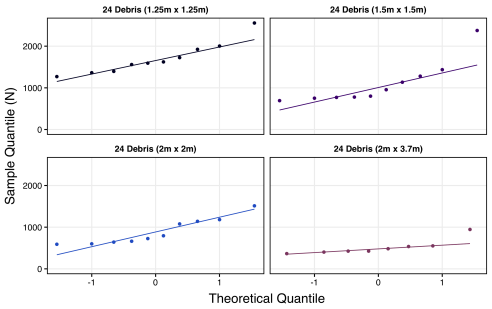


(b) First peak.

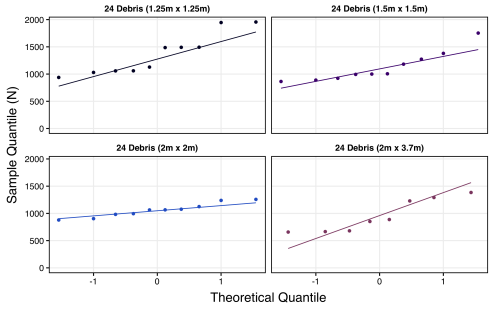


(c) Second peak.

Figure C.7: QQ-plots for absolute maximum, FIRST peak, and SECOND peak values for all random, standard-sized, 24 debris trials.

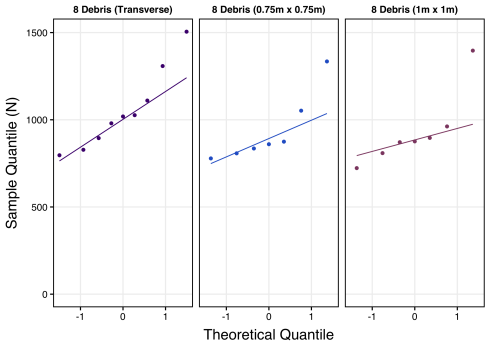


(a) Absolute maximum peak.

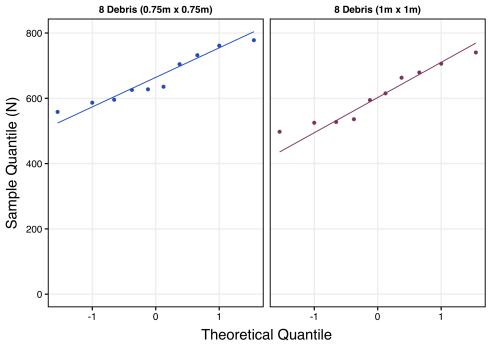


(b) First peak.

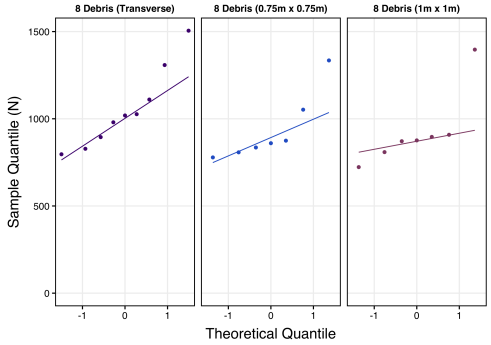


(c) Second peak.

Figure C.8: QQ-plots for absolute maximum, FIRST peak, and SECOND peak values for all multi-sized, 8 debris trials.

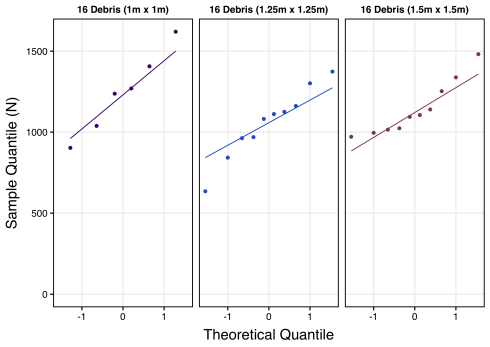


(a) Absolute maximum peak.

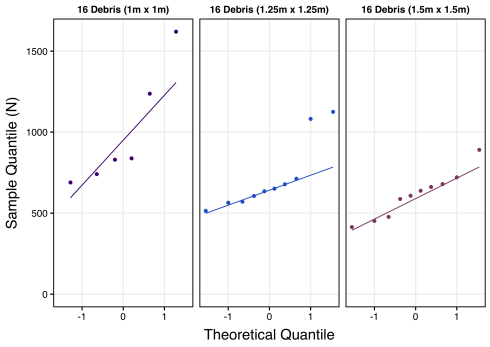


(b) First peak.

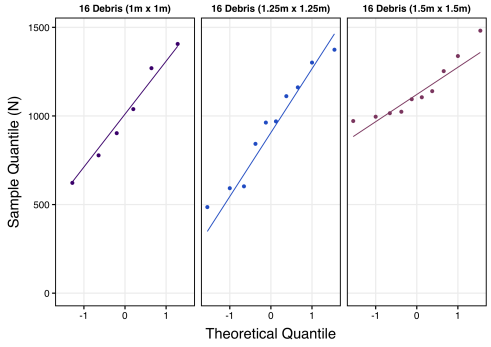


(c) Second peak.

Figure C.9: QQ-plots for absolute maximum, FIRST peak, and SECOND peak values for all multi-sized, 16 debris trials.

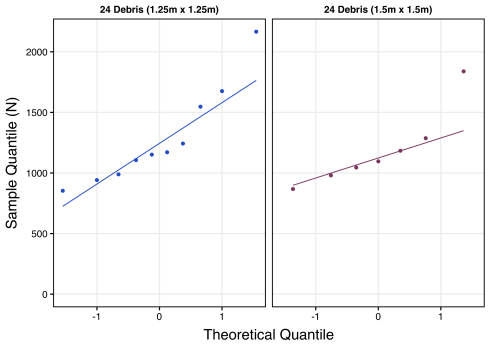


(a) Absolute maximum peak.

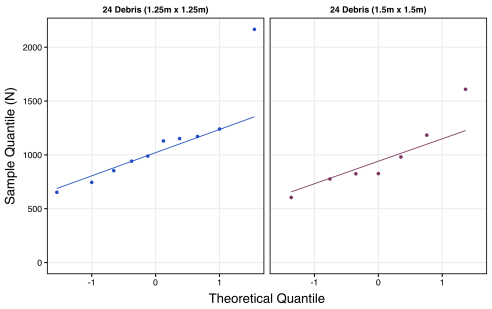


(b) First peak.

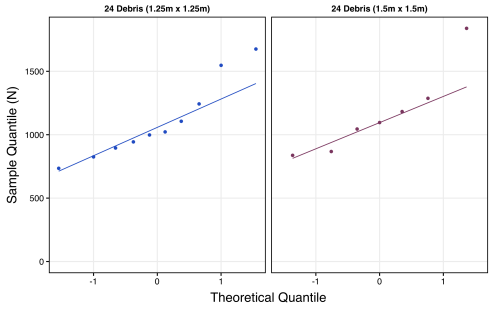


(c) Second peak.

Figure C.10: QQ-plots for absolute maximum, FIRST peak, and SECOND peak values for all multi-sized, 24 debris trials.